1991

Unsteady flow in an actively-controlled centrifugal pump

Ozgur Akin
Lehigh University

UNSTEADY FLOW

IN AN ACTIVELY-CONTROLLED

CENTRIFUGAL PUMP

by

ÖZGÜR AKIN

A Thesis

Presented to the Graduate Committee

of Lehigh University

in Candidacy for the Degree of

Master of Science

in

Mechanical Engineering

Bethlehem, PA

1991

This thesis is accepted and approved in partial fulfillment of the requirements for the degree of Master of Science.

09/19/91
(date)

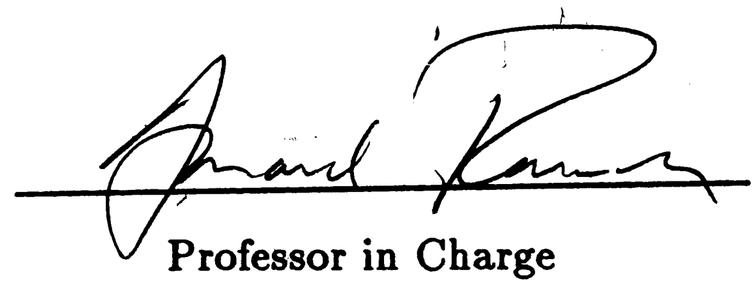

Professor in Charge

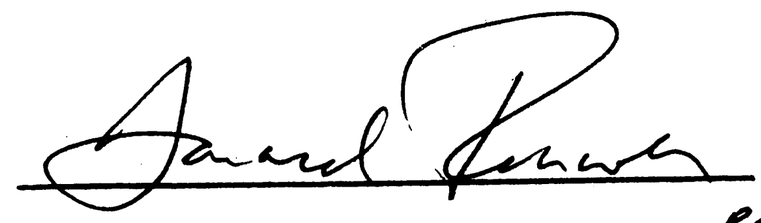

Chairman of Department RM R.P. WEI

TO MY MOTHER

GRANDMOTHER AND GRANDFATHER

ACKNOWLEDGĒMENTS

I would like to thank my family for their never ending love and encouragement through my whole life. I could not come to this point without their support. I gratefully acknowledge my advisor Dr. Donald Rockwell for his continuous support and guidence throughout my research. He has been more than an advisor to me during my stay at Lehigh.

I wish to express my gratitude to Turkish Oil Foundation for their financial support in my first semester at Lehigh University.

I would also like to thank Messrs. Emerson W. Wagner, Frank C. Klucsik, Richard Towne and the staff at the M.E. machine shop for their help and valuable suggestions. Nothing was impossible with them.

In addition, a special word of gratitude goes to Semi Konak for his essential friendship and help during my life at Lehigh. I also acknowledge John P. Fitzgerald as a new but valuable friend. I would also like to thank Charles Magness for answering my endless questions patiently.

Finally, I am indebted to all of my friends and my girlfriends, in U.S.A. and in Turkey, for their company and understanding: their friendship was essential.

TABLE OF CONTENTS

NOMENCLATURE

A	Area
b	Breadth
c	Absolute velocity
c_m	Meridional component of the absolute velocity
c_u	Peripheral component of the absolute velocity
D	Diameter
e	Measurement location from the discharge of the impeller
f	Frequency
f_{BP}	Blade passing frequency
f_F	Forcing frequency of the inlet flow and impeller perturbations
f_{Fi}	Forcing frequency of the impeller perturbation
f_{Fp}	Forcing frequency of the inlet flow perturbation
g	Gravity constant
h	Height of the collector
H_t	Total head
H_{th}	Theoretical head
n	Rotational speed of the impeller [rev/s]
N	Rotational speed of the impeller [RPM]
N_s	Specific speed of the pump $\left(N_s = \frac{N\sqrt{Q}}{H_t^{3/2}}\right)$
P^*	Amplitude of pressure fluctuations
Q	Flow rate of the pump
r	Radius

t	The gap between the collector and the diffuser
t_4	Pitch of the vaned diffuser inlet
U	Peripheral velocity of the impeller
V	Flow speed at the outlet of the contraction
V^*	Amplitude of velocity fluctuations
V_p	Piston velocity
w	Relative velocity
w_u	Peripheral component of the relative velocity
x	Width of the collector
z	Number of impeller blades
z_d	Number of diffuser blades
α	Flow angle (angle between c and U)
β	Blade angle (angle between w and U)
ϕ	Flow coefficient $\left(\phi=\frac{Q}{U_2 A_2}\right)$
μ	Slip coefficient
η	Overall efficiency of the pump
η_H	Hydraulic efficiency of the pump
η_V	Volumetric efficiency of the pump
η_m	Mechanical efficiency of the pump
ψ	Pressure coefficient $\left(\text{Head coefficient; } \psi=\frac{g H_t}{U_2^2}\right)$
ψ_{ip}	Phase shift between the inlet flow and impeller perturbations
Δh_p	Total losses in the impeller
$\frac{\tilde{V}_i}{\bar{V}_i}$	Amplitude of impeller perturbations

$\frac{\tilde{V}_p}{\bar{V}_p}$	Amplitude of inlet flow perturbations
$\frac{e}{r_i}$	Dimensionless measurement location

SUBSCRIPTS

1	Inlet of the impeller
1m	Mean inlet of the impeller
2	Outlet of the impeller
3	Inlet of the diffuser discs
4	Leading edge of the diffuser blade
5	Outlet of the diffuser discs
i	Impeller
p	Inlet flow
thr	Collector throat
v°	Dimensions of the throat at different angles

ABSTRACT

This investigation aims to bring an understanding to some of the sources of noise generation in rotating flows. A radial flow, rotating machine is constructed of Plexiglas. Detailed insight into the steady and unsteady flow structure, and corresponding pressure and velocity fields are addressed by experimental investigation of this simulated centrifugal pump. The transparent rotating machine consists of four main components: a centrifugal impeller; a vaneless diffuser; a vaned diffuser, with an adjustable blade; and a collector.

The control of the throughflow and rotation of the impeller are maintained by two independent, computer-driven motors. Control of the flow structure and the unsteady pressure fields are maintained by both self-generated and externally-imposed perturbations to the rotating machine at design and off-design operating conditions.

The pressure field on a simulated volute is explored at various locations downstream from the discharge of a three-blade impeller. The corresponding velocity fields are obtained using LDV technique.

The velocity fields are obtained for the following cases; discharge from a free, six-blade impeller; and in the presence of vaneless and vaned diffusers. The velocity fluctuations are examined in terms of the blade passing frequency, the forcing frequencies of the inlet flow and the impeller perturbations, and the sum and difference frequencies, which are due to nonlinear interactions.

1. INTRODUCTION

This investigation aims to bring an understanding to some of the sources of noise generation in rotating flows. Detailed insight into the steady and unsteady flow structure, and the corresponding pressure and velocity fields, are addressed by experimental investigation of a simulated centrifugal pump.

Unsteady flow phenomena in centrifugal impeller passages have been investigated by Lennemann and Howard (1968). The mechanism of stall was visualized for different types of impellers. They detected a change from steady to unsteady flow, in terms of stall development in the impeller passages, as the flow coefficient was decreased below a value of ϕ=0.04. The propagation of passage stall was correlated to an inducer backflow region whose primary effect was deflection of streamlines. The boundary layer on the suction side separated and backflow occurred along the suction side, blocking off the discharge side and reversing the flow direction in the passage. The direction of the backflow was reinforced by the relative motion of an eddy in the rotating system. This observation is important in the case of a diffuser located at the discharge of the impeller.

The flow in a vaneless diffuser is characterized by the presence of blade wakes, which are influenced by eventual flow separation on the suction side of the blades (Paone, 1989). This type of flow can be considered as unsteady with a period defined by the blade passing frequency. The amplitude and magnitude

of the velocity are a function of the diffuser width and circumferential position.

The effect of vaneless diffuser geometry on rotating stall was investigated by Otugen (1988). Mass flow rate and the rotation rate of the impeller were varied for different wall shapes and dimensions. This investigation showed that the critical mass flow rate for the onset of rotating stall decreased with increasing diffuser width. Moreover, increasing the ratio of the diffuser radius to the radius of the impeller delayed the onset of rotating stall. The effects of the slopes of the diffuser walls were investigated by Sherstyuk. He found that an increase in the diffuser outlet width could produce the highest radial static pressure gradients without flow separation. This result is supported by Yinkang (1987).

Vaned diffusers are widely used in pumping systems. The interactions between impeller blades and diffuser vanes were investigated on a diffuser pump by Arndt (1983). He found that the pressure fluctuations were larger on the suction side of the blade. Moreover, the pressure fluctuations were smaller near the shroud wall compared to the ones near the hub wall. This concept was also addressed in detail by Johnson (1979). Arndt describes the impeller-diffuser interactions in terms of two different mechanisms; potential flow interactions and wake interactions. He also found that the pressure fluctuations at the discharge of the impeller are periodic with impeller blade passing frequency and its higher harmonics. In other words, the generated noise is often dominated by tones at blade passing frequency and its higher harmonics.

Herein, the steady and unsteady flow structure and the corresponding

pressure fields are investigated experimentally using a centrifugal pump simulation system. Control of the flow structure and the unsteady pressure field are maintained by both self-generated and externally-imposed perturbations to the rotating machine. The transparent rotating machine consists of four main components: a centrifugal impeller; a vaneless diffuser; a vaned diffuser with an adjustable blade; and a collector.

The control of the throughflow and rotation of the impeller are maintained by two independent Compumotors. The Compumotors allow investigation of the flow structure for different operating conditions such as steady or unsteady flow at full or partial capacity.

In the first part of the investigation, the pressure field on a simulated volute is explored at various locations downstream from the discharge of the three-blade impeller. The corresponding velocity fields are obtained using a Laser Doppler Velocimetry (LDV) technique.

In the second part of the investigation, the velocity fields are obtained for three cases: discharge from a free, six-bladed impeller; in the presence of vaneless diffuser; and in the presence of vaned diffuser. The LDV measurements are performed at various locations. Externally-imposed perturbations are exerted in the form of synchronized or phase-shifted inlet flow and impeller perturbations at various frequencies and amplitudes. The velocity fluctuations are examined in terms of the blade passing frequency, the forcing frequency of the inlet flow and the impeller perturbations, and the sum and difference frequencies, which are due to nonlinear interactions.

2. EXPERIMENTAL SYSTEM

Having defined the objectives of this investigation, the first step taken was the design and construction of a transparent rotating machine with active control of the inflow and the impeller rotation. This unique radial flow rotating machine system is constructed of plexiglass in order to provide full visual access into the flow structure (Figures 2.1.a,b,c). The active control accomplished by the use of Compumotors; they control the instantaneous flow into the rotating machine and the rotation rate of the impeller. The design of the main components of the rotating machine is explained in Appendices A and B.

The velocity of the inlet flow is controlled by a Compumotor (PARKER-AX83-135) which is connected to a ball bearing screw by an elastic coupling (Figure 2.2). The screw, 1.0 inch diameter and 0.25 inch lead, is mounted on a table which holds the piston rod. A 3.0 feet long, 9.0 inch ID and 10.0 inch OD plexiglass cylinder is used to provide continuous flow into the contraction. The connection between the cylinder and the contraction is sealed with silicon. Providing the in flow by a Compumotor-driven piston-cylinder system was one of the advantages of this experimental system. The character and magnitude of the inlet flow can be changed easily. We were able to change the velocity over a reasonably wide range and create perturbation at various amplitudes. Another advantage of the piston-cylinder system was obtaining very high accuracy and uniformity of the inlet flow. There were no valves or other obstructions that could disturb the flow. The leakage between the cylinder and the piston is prevented by two Teflon O-rings. The lubricating characteristics of the Teflon

helped to minimize the mechanical noise during the operation. During the back stroke of the piston, water spray is used to lubricate the O-rings and minimize the mechanical vibrations which could damage the system.

The connection between the ball bearing screw and the piston table is specially designed so that the screw and the motor can be changed without interfering with the other parts of the system.

Before designing the rest of the system, the Compumotor and the ball bearing screw system were tested at various speeds. A speed of 120 RPM was the optimum for the motor to operate without stall and significant mechanical noise. The motor started to stall after 180 RPM. In order to be able to work at higher flow speeds, a Compumotor with a higher torque (PARKER-AX-106-205) and a 1.0 inch lead ball bearing screw were purchased. These components allowed us to increase the maximum value of the piston velocity from 0.75 in/s to 2.0 in/s .

The piston is connected to a contraction 10.0 inches long, the contraction has an area ratio of 1/16. The design of the contraction is explained in detail in Appendix A. For the optimum speed of the piston (0.5 in/s) the mean flow velocity at the outlet of the contraction is 8.0 in/s.

The total length of the connection between the contraction and the impeller is 2.5 inches. We tried to minimize the boundary layer effect in the constant diameter tubing by keeping this length as short as possible. A 2.25 inches ID brass tubing is used to guide the flow from the exit of the contraction to the inlet of the impeller. A DELRIN bearing is machined around the brass

tube and connected to the impeller by screws in order to guide the impeller. The clearance of the bearing is chosen carefully so that the impeller does not move in the axial and radial directions. The impeller is also driven by a Compumotor; the torque is transmitted by a gear-chain system. A plastic coated chain is used in order to minimize the mechanical noise. The gear ratio is chosen as 1/2 ; a 6.0 inches gear is mounted on a plexiglass tube which holds the bearing and the impeller. The distance between the axis of the chain and the impeller inlet was chosen as 1.375 inches, so that the impeller discharge flow would not be disturbed by the fluctuations generated by the gear-chain system.

Beginning from the contraction, the system is placed in a Plexiglass tank (33.0 inches x 24.0 inches x 27.0 inches) by drilling a hole on one side of the tank. In order to prevent leakage, an O-ring is pressed between the hole and the contraction. This design allowed us to move the whole system forward and backward so that an extension pipe (50.0inches) between the contraction and the impeller inlet could be mounted during subsequent stages of the investigation.

The whole system, including the tank, was mounted on a steel frame. The system is leveled by six leveling screws. These screws allowed us to vary the height of the system by as much as 16.0 inches.

Two types of impellers were used in the experiments. The first impeller is designed in order to perform the preliminary experiments (Figure 2.3). This impeller served the purpose of understanding the problems of the system, such as mechanical and electrical noise. It also helped us to overcome the problems of using quantitative flow visualization techniques on a rotating machine. The

impeller had three blades which were constructed by the Single Arc Method. The blade thickness is kept constant from the leading edge to the trailing edge in order not to machine the blades. Machining the blade could cause some additional refraction of the laser sheet. In summary, we had full visual access from the inlet up to the discharge.

Detailed dimensions of this impeller are as follows :

$$\frac{D_2}{D_1} = \frac{9.00 \text{ in}}{2.25 \text{ in}} = 4.0 \qquad b_1 = b_2 = 0.45 \text{ in}$$

$$\beta_1 = 18.0^\circ \qquad \beta_2 = 25.0^\circ \qquad z = 3$$

Blade angles were chosen to be representative of the range of values used widely in industry. We were aware of the problems which would be caused because of not guiding the flow at the inlet of the impeller and using just three blades. This was a compromise in order to overcome the difficulties of performing laser sheet techniques on a rotating machine, and solving the mechanical and electrical problems of the system before using a realistic impeller. It should be noted, however, that this type of impeller is generic to family of impellers used by the U. S. Navy in their early pumping systems. [T. Calvert, private communication, 1989]

The second impeller was a more sophisticated radial flow impeller (Figure 2.4). It had six blades that were constructed by the Single Arc Method with

constant thickness from the leading edge to the trailing edge. The impeller was machined from plexiglass using a CNC milling-machine.

Detailed dimensions of this impeller are as follows :

$\frac{D_2}{D_1} = \frac{6.75 \text{ in}}{2.25 \text{ in}} = 3.0$ $\quad b_1 = 1^{9/32}$ in $\quad b_2 = 3/8$ in

$\beta_1 = 20.0^\circ \quad \beta_2 = 27.0^\circ \quad z = 6$

A plexiglass vaneless diffuser is designed in order to diffuse the flow at the exit of the impeller. The vaneless diffuser consists of two separate discs, making up the parallel walls of the diffuser. The breadth of the diffuser could be increased or decreased during the experiments. The breadth of the diffuser is chosen as 10% smaller than the impeller discharge breadth, and this value is kept constant from the inlet to the exit. The ratio of the diffuser exit diameter to the impeller exit diameter is chosen as 1.6. The radial clearance between the impeller blades and the diffuser disks was about 9% of the impeller diameter.

The vaneless diffuser can also be used as a vaned diffuser by mounting a blade between these disks. This type of design allowed us to change the angle of attack of the diffuser blade and the gap between the diffuser inlet and the leading edge of the blade.

In order to complete the pump simulation, a rectangular, constant width collector was designed. The collector is also machined from plexiglass so that the

flow from the inlet of the impeller to the discharge of the collector can be visualized.

The design criteria for the second impeller, vaneless and vaned diffusers and the collector are given in detail in Appendix B.

3. THREE BLADE IMPELLER: VELOCITY AND PRESSURE FLUCTUATIONS

This chapter addresses some of the preliminary experiments which are performed on an idealized impeller (see Figure 3.1). Even though the impeller was a simplified version of commonly employed impellers, it helped us solve design problems and overcome experimental difficulties.

Pressure and LDV measurements were the two experimental techniques performed at this stage of the research. A number of velocity and pressure measurements were performed at various distances from the discharge of the impeller. In order to focus on the most representative results, we will describe experiments performed at a location 0.5 in. downstream of the impeller discharge.

The pressure measurements were performed on the interior of a simulated volute (see Figure 3.2) using a PCB Piezotronic Transducer (PCB 106B50). The sensitivity of the transducer was 596.2 mV/psi (Figure 3.3). The dimensions of the transducer are given in Figure 3.4. The transducer is held in place by a specially-designed mount. The entire transducer, except the diaphragm, is sealed with high vacuum grease in order to prevent leakage from the rear. For most of the cases the best dynamic performance is attained by a flush diaphragm design (see Figure 3.5). Even though tubing and cavity transducer design degrades performance to some extent, the flush diaphragm transducer was not applicable to our case.

The transducer mount is shown in Figure 3.6. The mount was attached to a ring which rested on the tank (see Figure 3.7). The ring had two degrees of freedom, so the distance between the discharge of the impeller and the transducer could be adjusted. During the experiments the biggest problem was the mechanical and electrical noise. This subject is covered in detail in Appendix C.

Corresponding velocity measurements were performed at the impeller outlet using a Laser Doppler Velocimeter. The setup of the LDV system is shown in Figure 3.8. The control volume of the LDA was located a distance of 0.5 in. from the impeller discharge.

In general, the spectra obtained by pressure measurements were more informative than the velocity spectra. In other words, the peaks at certain frequencies, such as blade passing and perturbation frequencies and their harmonics, were more significant than those obtained from velocity measurements.

For both pressure and velocity measurements, an analog filter was used to filter the frequencies above the Nyquist frequency. This approach prevented high frequency noise from folding back to the regions of the spectrum of interest. In order to eliminate low frequency noise during the pressure measurements, the high pass filter setting was chosen as 1 Hz. In summary, the low and high pass filter settings were 50 Hz and 1 Hz and the Nyquist frequency was 50 Hz.

In subsequent chapters, some of the results obtained from these preliminary experiments will be compared with those acquired from experiments

performed on the six-blade impeller.

In the sections of this chapter that follow, the spectra of pressure and velocity will be categorized according to the type of forcing applied, namely perturbation of the inlet flow and the perturbation of the impeller at f_F, and the values of these frequencies in comparison with the blade passing frequency f_{BP}.

3.1. CATEGORY I

In this category, the forcing frequency of the inlet flow and impeller perturbations f_F is less than the blade passing frequency f_{BP}. The values of the forcing frequency f_F of the inlet flow perturbations and the blade passing frequency f_{BP} were 1.0 Hz and 1.5 Hz respectively. In the plots given in Figure P1 through V14, the following terminology holds: Φ is the flow coefficient defined as the ratio of the radial velocity of the flow at the discharge of the impeller to the tangential velocity of the impeller at the discharge. The ratio of the perturbation amplitude of the inlet flow to the mean inlet flow velocity is defined as $\tilde{V}_p/\overline{V}_p$; correspondingly, the ratio of the tangential velocity fluctuations amplitude induced by the impeller perturbation, normalized by the mean value of the tangential velocity of the impeller due to its steady rotation is defined as $\tilde{V}_i/\overline{V}_i$. Finally, the ratio of the forcing frequency f_F of the inlet flow and impeller perturbation, normalized with respect to the blade passing frequency f_{BP} is delineated as f_F/f_{BP} .

In the table given below, the combinations of the parameters investigated

in this phase of the investigation are defined.

PLOT #	ϕ	$\frac{\tilde{V}_p}{\bar{V}_p}$	$\frac{\tilde{V}_i}{\bar{V}_i}$	$\frac{f_F}{f_{BP}}$
P1 & V1	0.177	0	0	0
P2 & V2	0.177	0.3	0	0.667
P3 & V3	0.177	0.3	0.1	0.667
P4 &V4	0.177	0.3	0.3	0.667

First, considering the spectra of the pressure fluctuations given in Figure P1 through P4, it is evident that in the absence of any applied perturbation, i.e. with no control, the amplitudes of the higher harmonics of the blade passing frequency have a value equal to or larger than the fundamental component. When active control is exerted in the form of inlet flow perturbations at frequency f_F, as illustrated in Figure P2, there occur not only the blade passing frequency and inlet perturbation frequency in their higher harmonics, but also sum and difference frequencies between the wave passing frequency f_{BP} and perturbation frequency f_F. These sum and difference frequencies are clearly due to nonlinear interactions. In general, however, their amplitudes remain considerably smaller than those of blade passing frequency and its higher harmonics in the case of simultaneous inlet flow and impeller perturbations at

the same frequency, as given in Figure P3. For this particular set of excitation conditions, the first harmonic of the perturbation is of the same order of magnitude as the blade passing frequency and its higher harmonics, even though the fundamental component of the impeller perturbation is relatively small. In the event that the amplitude of the impeller perturbation is increased, as shown in Figure P4, the amplitudes of the perturbation frequency and its first harmonic increase; moreover, there is a substantial increase in the amplitudes of the sum and difference components as well.

The corresponding spectra of the velocity measurements shown in Figure V1 through V4 show several features in common with the pressure spectra. In the case of no applied control, as indicated in Figure V1, only the blade passing frequency and its higher harmonics are present. The highest harmonic in the velocity spectra is the first harmonic; however, the highest harmonic in the pressure spectra is the second harmonic. With the presence of an inlet flow perturbation at frequency f_F, the amplitude of the fundamental component at the inlet forcing frequency is of the same order as that of the blade passing frequency; this result seems to be contrary to that in the pressure spectra described in the foregoing. Indications of higher harmonics and nonlinear sum and difference frequencies are present. The presence of components above the forcing component f_F, of both the inlet flow and the impeller, is indicated in Figure V3 and V4. The form of the pressure and the velocity spectra is the same as that in absence of the impeller perturbation for the lower value of the impeller perturbation amplitude (Figure V3). However, when the amplitude of the impeller perturbation is increased, the higher harmonics and the nonlinear sum

and difference components are substantially attenuated.

In summary, for the range of excitation conditions given in the above table, the following conclusions can be made.

(a) The amplitude of the blade passing frequency and its harmonics do not change when either the inlet flow or impeller are subject to perturbations.

(b) The amplitude of the component at the perturbation frequency is typically about two-thirds that at the blade passing frequency; it *decreases* when the impeller perturbation has a relatively low amplitude of about 10%. When the impeller perturbation amplitude is increased to 30%, however, the amplitude of the peak actually *increases* slightly.

(c) The background noise level does not seem to change, either for the pressure or the velocity spectra.

(d) The attenuation of the peak at the perturbation frequency, evident in the pressure spectra, cannot be detected in the velocity spectra.

3.2. CATEGORY II

In this category, the forcing frequency of the inlet flow and the impeller perturbations f_F is larger than the blade passing frequency f_{BP}. The values of the forcing frequency f_F of both the inlet flow and impeller perturbations and the blade passing f_{BP} frequency were 2.0 Hz and 1.5 Hz respectively. Therefore the ratio of the forcing frequency of the perturbations to the blade passing frequency

is 1.333 .

In the table given below, the combinations of parameters investigated in this phase of the investigation are defined.

PLOT #	ϕ	$\frac{\tilde{V}_p}{\bar{V}_p}$	$\frac{\tilde{V}_i}{\bar{V}_i}$	$\frac{f_F}{f_{BP}}$
P5 & V5	0.177	0.3	0	1.333
P6 & V6	0.177	0.3	0.1	1.333
P7 & V7	0.177	0.3	0.3	1.333

Considering the spectra of the pressure fluctuations given in Figure P5 through P8, it is evident that in the absence of either inlet flow or impeller perturbations, i.e. with no active control, the higher harmonics of the blade passing frequency have a value equal to or slightly larger than the fundamental component. This observation is similar to that of the previous category. When active control is exerted in the form of inlet flow perturbations at frequency f_F and amplitude 30%, as shown in Figure P5, there occur not only the blade passing frequency in its higher harmonics, but also the sum and difference frequencies between the blade passing frequency f_{BP} and the perturbation frequency f_F. The peak at the forcing frequency of the inlet flow has the highest

amplitude compared to other frequencies. However, the amplitude of its first harmonic is substantially smaller. Active control induces sum and difference frequencies that are clearly due to nonlinear interactions. In general, their amplitudes remain smaller than those of the blade passing frequency and its higher harmonics, even in the case of simultaneous inlet flow and impeller perturbations at frequency f_F, as given in Figure P6. For this particular set of excitation conditions, the fundamental component of the inlet flow perturbation still has the highest amplitude and the higher harmonics of this frequency are present in the spectrum with relatively high amplitudes. In the event that the magnitude of the impeller perturbation is increased to 30%, as shown in Figure P7, the amplitudes of the perturbation frequency and its harmonics increase; moreover, there is a significant increase in the amplitudes of the sum and difference components as well. The amplitude of the peak at the perturbation frequency remains unchanged when there is a simultaneous impeller perturbation. The change in the amplitude of the impeller perturbation does not affect the amplitude of this peak.

The corresponding spectra of the velocity measurements are shown in Figures V5 through V7. They show some features in common with the pressure spectra. With the presence of inlet flow perturbations at frequency f_F, the amplitude of the fundamental component at the inlet forcing frequency is of the same order as the higher harmonics of the blade passing frequency. In contrast with the pressure spectra, higher harmonics of the inlet flow perturbation frequency cannot be detected. Nonlinear sum and difference frequencies are present. When the impeller perturbation at frequency f_F is simultaneously

applied, the amplitude of the peak at the perturbation frequency decreases; this result seems to conflict with the pressure spectra. The number of nonlinear sum and difference frequencies does not change with increasing amplitude of the impeller perturbation. However, when the magnitude of the impeller perturbation is increased from 10% to 30%, the amplitude of the peak at the perturbation frequency increases significantly. The amplitudes of the peaks at the blade passing frequency and its higher harmonics do not change with either the inlet flow or the impeller perturbation.

In summary, for the range of excitation conditions given in the above table, the following conclusions can be made.

(a) The amplitudes of the peaks at the blade passing frequency and its higher harmonics do not change when either the inlet flow or the impeller are subjected to perturbation.

(b) The amplitudes of the peaks at the blade passing frequency do not change when either the inlet flow or impeller are subject to perturbation.

(c) The amplitudes of the nonlinear sum and difference frequencies increase when the impeller has a relatively low amplitude of about 10%. When the impeller perturbation amplitude is increased to 30%, the amplitude of the peaks increases drastically.

(d) The attenuation of the peak at the perturbation frequency, evident in the velocity spectra, cannot be detected in the pressure spectra.

3.3. CATEGORY III

In this category, the forcing frequency f_F of the inlet flow and impeller perturbations is equal to the blade passing frequency f_{BP}. The value of the forcing frequency and the blade passing frequency f_{BP} was 1.5 Hz. Therefore the ratio of the forcing frequency of perturbations f_F to the blade passing frequency f_{BP} is unity.

In the table given below, the combinations of parameters investigated in this category are defined.

PLOT #	ϕ	$\frac{\tilde{V}_p}{\bar{V}_p}$	$\frac{\tilde{V}_i}{\bar{V}_i}$	$\frac{f_F}{f_{BP}}$
P8 & V8	0.177	0.3	0	1
P9 &V9	0.177	0.3	0.3	1

Since the forcing frequency f_F of the inlet flow and the impeller perturbations is equal to the blade passing frequency f_{BP}, the terminology " *frequency of interest*, f " will be used in order to represent these frequencies. Considering the pressure spectra given in Figures P8 and P9, it is evident that, in the presence of impeller perturbation, the number of higher harmonics of the frequency of interest increases. When active control is exerted in the form of

impeller perturbation with a relatively high amplitude, even the sixth harmonic of the frequency of interest is detected (Figure P9). For both cases, the amplitude of the fundamental component at the frequency of interest is higher than the amplitude of its harmonics.

The corresponding spectra of the velocity is shown in Figures V8 and V9. These spectra show identical features to the pressure spectra. Increasing the amplitude of synchronized impeller perturbation increases the number of detectable higher harmonics of the frequency of interest. However, the highest harmonic of this frequency, which appears in the spectrum (Figure V9), is the third harmonic. The amplitude of the fundamental component at the frequency of interest is the highest; the amplitude of each higher harmonic successively decreases.

In summary, the following conclusions can be made for the case of forcing the inlet flow and the impeller at the same frequency as the blade passing frequency.

(a) The amplitude of the fundamental component at the frequency of interest is higher than its harmonics and the amplitude of its higher harmonics *decreases* gradually relative to the fundamental component.

(b) The number of detectable higher harmonics is larger than any other case presented in the previous categories.

(c) The background noise level remains unchanged, both in the pressure or the velocity spectra.

3.4. CATEGORY IV

This category consists of two different cases. In the first case, the blade passing frequency f_{BP} is larger than the forcing frequency of the inlet perturbations f_{Fp} but smaller than the forcing frequency of the impeller perturbations f_{Fi}. In the second case, the blade passing frequency f_{BP} is larger than the forcing frequency of the impeller perturbation f_{Fi} but smaller than the forcing frequency of the inlet flow perturbations f_{Fp}. The value of the blade passing frequency for both cases was 1.5 Hz. For the first case, the forcing frequency of the inlet flow and the impeller perturbations were 1.0 Hz and 2.0 Hz respectively. For the second case, these values were 2.0 Hz and 1.0 Hz.

In the table given below, the combinations of parameters used in these two cases are defined.

PLOT #	ϕ	$\frac{\tilde{V}_p}{\bar{V}_p}$	$\frac{\tilde{V}_i}{\bar{V}_i}$	$\frac{f_{Fp}}{f_{BP}}$	$\frac{f_{Fi}}{f_{BP}}$
P10 & V10	0.177	0.3	0.3	0.667	1.333
P11 & V11	0.177	0.3	0.3	1.333	0.667

First, considering the spectra of the pressure fluctuations given in Figures P10 and P11, the amplitudes at the higher harmonics of the blade passing

frequency have a value equal to or larger than the fundamental component. The sum and difference frequencies, which are due to nonlinear interactions, do not change in both sets of spectra. Therefore one can say that the presence of these sum and difference frequencies is independent of the value of the forcing frequency of either inlet flow or impeller perturbations. Supporting the result in Category II, when the forcing frequency of the inlet flow is larger than the blade passing frequency, the amplitude of the peak at the forcing frequency of the inlet flow is larger than that of the blade passing frequency, its higher harmonics and the forcing frequency of the impeller perturbation (Figure P11). However, the higher harmonics of neither the inlet flow nor the impeller perturbation frequencies are present.

Unfortunately, the corresponding velocity spectra, shown in Figures V10 and V11, do not show any features in common with the pressure spectra. For both cases, the higher harmonics of the blade passing frequency have an amplitude smaller than the fundamental component, and the amplitude decreases with each higher harmonic. One difference frequency is present due to nonlinear interactions. The amplitude of this peak is relatively high but does not change with the value of the forcing frequency of the inlet flow and impeller perturbations. The peak at the forcing frequency of the impeller perturbation is not present when it is larger than the blade passing frequency. But the amplitude of this peak increases substantially in the case where the forcing frequency of the impeller perturbation is smaller than the blade passing frequency. A peak at the forcing frequency of the inlet flow is detected in both cases and its amplitude remains unchanged.

For the cases explained above, due to conflicting results obtained from the pressure and velocity spectra, no conclusions can be made.

3.5. CATEGORY V

In this category, the forcing frequency of the inlet flow and impeller perturbation f_F is less than the blade passing frequency f_{BP}. The values of the forcing frequency and the blade passing frequency were 1.0 Hz and 1.5 Hz. The ratio of the forcing frequency of the inlet flow and impeller perturbations to the blade passing frequency was 0.667. Instead of synchronized impeller perturbations, active control is exerted in the form of impeller perturbations with a defined phase shift ψ_{ip} with respect to the inlet flow perturbations. The impeller perturbations are shifted of $\psi_{ip}=\pi/2$, π and $3\pi/2$ radian as shown in Figures V12, V13 and V14 respectively.

In the table given below, the parameters investigated in this phase of the investigation are defined.

PLOT #	ϕ	$\frac{\tilde{V}_p}{\bar{V}_p}$	$\frac{\tilde{V}_i}{\bar{V}_i}$	$\frac{f_F}{f_{BP}}$	ψ_{ip}
V12	0.177	0.3	0.3	0.667	$\pi/2$
V13	0.177	0.3	0.3	0.667	π
V14	0.177	0.3	0.3	0.667	$3\pi/2$

Considering the spectra of the velocity fluctuations, given in Figures V12 through V14, the amplitude of the blade passing frequency does not change. Even though the number of sum and difference frequencies increases at $\psi_{ip}=\pi$ radian phase shift, the amplitude of the peak at the difference frequency decreases with increasing phase shift angle. The peak at the forcing frequency reaches a maximum of π phase shift. Moreover, the first harmonics of the forcing frequency and the blade passing frequency can be detected only when the forcing frequency of the impeller is shifted π radians. The background noise level does not seem to change with the magnitude of the phase shift angle.

4. SIX BLADE IMPELLER: VELOCITY FLUCTUATIONS

This chapter addresses some of the experiments which were performed on the primary impeller, designed according to the criteria given in Appendix B. The impeller performance was studied using a free impeller, and in the presence of vaneless and vaned diffusers (Figures 4.1, 4.2 and 4.3). The design of these components are also explained in Appendix B.

Laser Doppler Velocimetry (LDV) measurements were performed at various locations. In this section, we will introduce some of the experiments which were performed at the discharge of the impeller, in the vaneless and vaned diffuser.

The design flow coefficient Φ was chosen as 0.111 due to Compumotor speed limitations. The design mean inlet flow velocity V and the rotational speed of the impeller n were 8.0 in/s and 0.85 rev/s respectively. In this case the blade passing frequency f_{BP} was 10.2 Hz. One of the aims of this study was to investigate the effect of various inlet and impeller perturbations on the discharge flow. But the Compumotors started to generate noise at high perturbation frequencies. Therefore by halving the mean inlet flow velocity and the rotational speed, the blade passing frequency was reduced to 5.1 Hz. Since the velocity ratio remained unchanged, the design flow coefficient was retained. Reducing the blade passing frequency allowed us to perform experiments over a wide range of perturbation frequencies.

The amplitude of perturbation of the inlet flow $\tilde{V}_p/\overline{V}_p$ and the impeller

$\tilde{V}_i/\overline{V}_i$ was varied between 5% and 30%. The impeller was perturbed synchronized, or with various phase shift angles, relative to the inlet flow perturbation at the same frequency.

4.1 Free Impeller

The following results are obtained from the LDV measurements at the discharge of the second impeller. The LDV setup is shown in Figure 3.8. Since the impeller was in a relatively large tank, the discharge velocity was diminished very quickly. LDV measurements were performed at various locations, but we could not detect any considerable flow after a distance of 0.5 inches downstream from the impeller discharge, where the ratio of the distance form the impeller discharge to the measurement location to the impeller radius $e/r_i = 0.148$. Even at 0.5 inches, only the large amplitude signals could be detected. Since we are interested in nonlinear interactions, which have relatively low amplitudes, the measurement location was moved to 1/8 inches downstream of the impeller discharge, $e/r_i = 0.037$.

The velocity spectra which are shown in Figure 4.1.1 are obtained when the impeller was operating at the design condition. The design flow coefficient Φ was 0.111 which corresponds to 8.0 in/s inlet velocity and 1.7 rev/s rotational speed. The magnitude of the inlet flow perturbation was ± 30% of the mean velocity. The experiment is performed at different forcing frequencies of the inlet flow perturbations f_F, $f_F = 2.0$ Hz, 4.0 Hz, 8.0 Hz and 9.0 Hz, corresponding to $f_F/f_{BP} = 0.196$, 0.39, 0.78 and 0.88 which are shown in Figure 4.1.1.a, b, c and d

respectively. The blade passing frequency f_{BP} for these cases was 10.2 Hz.

As shown in Figure 4.1.1, the number of sum and difference frequencies, which are due to nonlinear interactions, increased gradually with increasing perturbation frequency. The value of the forcing frequency of the inlet flow and impeller perturbations, and the amplitude of perturbation have a significant effect on the frequency range where the nonlinear interactions appear. As the perturbation frequency increases, the peaks at the perturbation frequency and its first harmonic are attenuated. According to the experimental results, which are shown in Figure 4.1.1.c and Figure 4.1.1.d, the peak at the perturbation frequency diminishes when the perturbation frequency reaches about 80% of the blade passing frequency. Considering the increase in the number of nonlinear interactions, one may say that its energy is transferred into nonlinear interactions. The unchanged background noise level supports this conclusion.

One of the most interesting results is the attenuation of the peak at the forcing frequency of the inlet flow and impeller perturbations when a synchronized impeller perturbation is introduced at the same frequency with the inlet flow perturbations. Some excerpts from this experiment are shown in Figure 4.1.2. Since the peak at the perturbation frequency diminishes when the perturbation frequency reaches about 80% of the blade passing frequency, the value of the forcing frequency of the inlet flow and impeller perturbations f_F, and the blade passing frequency f_{BP} were chosen as 2.0 Hz and 5.1 Hz respectively for this experiment. For all cases, the amplitude of the inlet flow perturbation was chosen as 30%, i.e. $\tilde{V}_p/\overline{V}_p=0.30$. The amplitude of the peak at the perturbation frequency decreased drastically with 5% synchronized impeller

perturbation, i.e. $\tilde{V}_i/\overline{V}_i=0.05$. In the case of 10% impeller perturbation this value reaches its minimum value, which is very close to the background noise level (Figure 4.1.2.b). As the amplitude of the impeller perturbations increases, the amplitude of the peak decreases and reaches its maximum value at 30% impeller perturbation, i.e. $\tilde{V}_i/\overline{V}_i=0.30$, as shown in Figure 4.1.2.c. By interpolating the experimental data, one can say that the peak at the perturbation frequency, due to 30% inlet flow perturbation, diminishes completely with about 8% synchronized impeller perturbation, i.e. $\tilde{V}_p/\overline{V}_p=0.30$ and $\tilde{V}_i/\overline{V}_i=0.08$ (Figure 4.1.3). The concept of compensating the relatively high amplitude inlet flow perturbation by a synchronized, low amplitude impeller perturbation can be explained in terms of the value of the operational flow coefficient. The flow coefficient is basically the ratio of radial discharge velocity to the tangential impeller velocity. Since, in this case, the design and operational flow coefficient is 0.111, the tangential velocity is 9 times higher than the radial discharge flow velocity. Therefore the impeller requires a lower amplitude perturbation in order to compensate the inlet flow perturbation which affects the discharge flow. In other words, if the unsteadiness of the inlet flow can be defined in terms of certain frequencies, this unsteadiness may be eliminated in order to create a more uniform flow at the discharge of the impeller. This may increase the diffuser efficiency.

The amplitude of the synchronized impeller perturbation $\tilde{V}_i/\overline{V}_i$ does not have a large effect on the nonlinear interaction peaks, which appear at the sum and difference frequencies between the blade passing and perturbation frequencies. This result led us to investigate the effects of a phase shift between

the inlet and impeller perturbation. Therefore four experiments were performed with phase shifts $\psi_{ip}=\pi/4$, $\pi/2$, $3\pi/4$ and π radians, as shown in Figures 4.1.4.c, d, e and f. The forcing frequency of the inlet flow and impeller perturbations was chosen as 2.0 Hz with 10% impeller and 30% inlet flow perturbations, i.e. $\tilde{V}_i/\overline{V}_i=0.10$ and $\tilde{V}_p/\overline{V}_p=0.30$. The number of nonlinear interaction peaks increased drastically when $\pi/4$ radian phase shift was introduced. The amplitude of these peaks increased slightly with increasing phase shift angles. Finally, they reached a maximum when the impeller perturbation was shifted π radian relative to the inlet flow perturbation.

4.2 Impeller in Presence of Vaneless Diffuser

The following LDV measurements were performed at 1/8, 3/8, 5/8 and 3/2 inches downstream of the leading edge, where $e/r_i=$ 0.37, 0.111, 0.185 and 0.444, of the vaneless diffuser discs, which are shown in Figures 4.2.a, b, c and d respectively. Active control was exerted in the form of inlet flow perturbations and the value of the forcing frequency of the inlet flow perturbations f_F was chosen as 2.0 Hz. The amplitude of the inlet flow perturbations was 30%, i.e. $\tilde{V}_p/\overline{V}_p=0.30$. The operational flow coefficient Φ and the blade passing frequency f_{BP} were 0.111 and 5.1 Hz respectively.

The experiments which are performed with the vaneless diffuser basically emphasize the following results. Most of the nonlinear interactions especially the ones at relatively higher frequencies (higher than $2f_{BP}$) are attenuated. Due to the design of the vaneless diffuser jet flow was created at the inlet of the diffuser.

This jet flow may be the reason for the attenuation of the peaks at high frequencies. When measurement location is moved downstream from the impeller discharge, due to the lower velocities, nothing but two or so peaks at low frequencies were present. At 3/2 inches, e/r_i=0.444, only the background noise could be detected.

Another interesting result was the decrease in the background noise level. Even at e/r_i=0.037, the background noise level was slightly lower than the free impeller cases, which are explained in the previous section. Finally at e/r_i=0.185 and 0.444, the background noise level decreased drastically (Figures 4.2.c and d). This may also be due to the lower velocities along the vaneless diffuser.

4.3 Impeller in Presence of Vaned Diffuser

The following experiments are performed at the design condition where the flow coefficient Φ was 0.111, with 4.0 in/s inlet velocity V and 0.85 rev/s rotational speed n. The corresponding blade passing frequency f_{BP} for these cases was 5.1 Hz.

The dimensions and the type of vaned diffuser is explained in Appendix B in detail. LDV measurements were performed at various locations, such as the leading edge, trailing edge, pressure and suction side of the diffuser blade. Due to the very low velocity right at the leading edge, the laser control volume was located at 3/16 inches upstream of the leading edge of this diffuser blade.

In order to obtain a reference case the first experiment is performed

without any perturbation. The only peaks which could be detected in the spectrum were at the blade passing frequency and its higher harmonics which; thet are shown in Figure 4.3.1.a. When a 10% perturbation was introduced into the inlet flow, besides a peak at the perturbation frequency, some nonlinear interaction related peaks were detected (Figure 4.3.1.b). The sum and difference frequencies, due to nonlinear interactions, were in the form of $nf_{BP}-f_F$. If, instead of a synchronized impeller perturbation, the impeller is perturbed 10% with a phase shift of $\psi_{ip}=\pi$ radian, the number of nonlinear interactions increases drastically, and they take the form $nf_{BP}\pm f_F$, as shown in Figure 4.3.1.c. The same results were obtained during the measurements at the free discharge of the impeller, as explained in section 4.1. As the amplitude of the peaks at the perturbation frequency and its higher harmonics increased, the amplitude of the peaks of the blade passing frequency and its higher harmonics decreased. Since the inlet flow perturbation was 10%, one can expect that the peak at the perturbation frequency can be attenuated by a relatively small amplitude of impeller perturbation. But when the impeller is perturbed at the same amplitude as the inlet perturbation, the amplitude of this peak increased, as shown in Figure 4.3.2.a. The same experiment is repeated with a 30% inlet perturbation; the number of nonlinear interactions increased and the peaks at the perturbation frequency and its higher harmonics are shown in Figure 4.2.2.b. The nonlinear interactions were again in the form of $nf_{BP}\pm f_F$. This result shows that the type of nonlinear interaction is related to the amplitude of the inlet perturbation rather than the presence of a phase shift between the inlet flow and the impeller perturbations. When 10% amplitude and $\psi_{ip}=\pi$ radian shifted

impeller perturbation is introduced, the amplitude of the peaks at the blade passing frequency and its higher harmonics are attenuated (Figure 4.3.2.c). Another decrease in amplitude is detected at the perturbation frequency. Basically, the foregoing results demonstrate that the peak at the perturbation frequency can be attenuated by low amplitude synchronized or phase-shifted impeller perturbation. As the amplitude of the perturbation peak decreases, the amplitudes of the higher harmonics of the perturbation frequency and the nonlinear interactions increase.

Since it becomes more difficult to detect the peak at the perturbation frequency as its value gets closer to the blade passing frequency, most of the experiments were performed with 2.0 Hz perturbation frequency. For the case shown in Figure 4.3.3, the perturbation frequency was 0.5 Hz and the blade passing frequency was 5.1 Hz. The aim was to understand the effect of low perturbation frequency on the spectrum. Even though the inlet flow is perturbed with an amplitude of 10%, all of the nonlinear interactions are detected (Figure 4.3.3.b). When a synchronized impeller perturbation at an amplitude of 10% is introduced, the amplitude of the peaks at the perturbation frequency and the nonlinear interactions increase, but the amplitude of the peaks at the blade passing frequency and its higher harmonics decreased drastically (Figure 4.3.3.c). This can be interpreted as a transfer of energy since the background noise level remained unchanged. The shifted perturbation of the impeller did not affect the spectrum except for a small decrease in the amplitude of the peak at the blade passing frequency , as shown in Figure 4.3.3.d .

Up to now, all the experiments are performed at the design condition.

The following results are obtained by operating the system in off-design conditions. The inlet flow velocity is kept constant at 4.0 in/s. In order to create off-design flow coefficients, the rotational speed of the impeller is changed. LDV measurements were performed at 3/16 inches upstream of the diffuser blade leading edge in two off-design operating conditions.

The first off-design flow coefficient is chosen as 0.188 with 0.5 rev/s rotational speed. The blade passing frequency which corresponds to this speed is 3.0 Hz; this case is represented in Figure 4.3.4.a. The biggest difference between the spectra obtained in the design and off-design conditions was the background level at low frequencies. The background noise level increased significantly between zero and the blade passing frequency as shown in Figure 4.3.4.a. This result may be due to rotating stall which is expected at low frequencies. The idea of detecting the rotating stall directed us to perform more velocity measurements which are focused on the low frequency range. But due to hardware limitations, we could not filter out the background noise and detect the low amplitude peaks at low frequencies. Even though some results are obtained, their reliability is questionable. Therefore these experimental results are not included here. In Figure 4.3.4.b, the perturbation frequency is chosen as 2.0 Hz. At 30% flow perturbation, the background noise level between zero and the blade passing frequency decreases slightly, but a peak at the perturbation frequency and some nonlinear interactions are detected. As shown in Figure 4.3.4.c, the π radian shifted, 10% impeller perturbation increases the number of nonlinear interactions, and the background noise level returns to its original level. The amplitude of the peak at the perturbation frequency decreases slightly, but its

first harmonic appears on the spectrum. In the meantime, the amplitude of the peaks at the blade passing frequency and its harmonics decrease drastically.

The second off-design flow coefficient corresponds to Φ=0.071 with 1.328 rev/s rotational speed. The blade passing frequency which corresponds to this speed is about 8.0 Hz. As shown in Figure 4.3.5.a, the background noise level between zero and the blade passing frequency was higher in comparison to the design condition. Figures 4.3.5.a and b reveals that it increases slightly with 30% inlet flow perturbation but remains unchanged with 10%, $\psi_{ip}=\pi$ radian phase-shifted impeller perturbation (Figure 4.3.5.c). A peak at the perturbation frequency and another peak at its first harmonic appear on the spectrum. Nonlinear interactions induced sum and difference frequencies are detected. Due to the impeller perturbation, the amplitude of the peak at the perturbation frequency increases, but the amplitude of its first harmonic decreases. While the amplitude of nonlinear interactions were increasing slightly, the amplitude of the peak at the blade passing frequency decreases and its first harmonic diminishes completely.

The last experiment which will be explained in this section is performed at the design condition. Due to the low velocity at the diffuser discharge, even the peak at the blade passing frequency is not detected. With 30% impeller perturbation, a low amplitude peak at the perturbation frequency appeared on the spectrum, as shown in Figure 4.3.6.a. Some nonlinear interactions are detected due to 10%, $\psi_{ip}=\pi$ radian phase-shifted impeller perturbation (Figure 4.3.6.b). It is very difficult to come to a conclusion from these spectra, since the resolution is lower than the previous cases. The only significant difference

between these measurements and the previous ones is a very high amplitude peak at about 0.5 Hz. This may be due to rotating stall but it was too weak to be detected clearly.

5. CONCLUSIONS

The most revealing results of this study are as follows:

• The amplitude of the blade passing frequency and its higher harmonics do not change when either the inlet flow or impeller are subjected to perturbations.

• The background noise level does not change, when either the inlet flow or the impeller perturbations are introduced, while the system operates at the design flow coefficient.

• The number of sum and difference frequencies, which are due to nonlinear interactions, increases gradually with increasing forcing frequency of the inlet flow and the impeller perturbations. The amplitude of these perturbations has a significant effect on the frequency range over which the nonlinear interactions appear. As the amplitude increases, the nonlinear interactions appear at higher frequencies.

• The peak at the perturbation frequency diminishes when the perturbation frequency reaches about 80% of the blade passing frequency.

• Relatively high amplitude inlet flow perturbations, in other words the unsteadiness of the inlet flow at certain frequencies, can be compensated by low amplitude, and either synchronized or phase-shifted impeller perturbations. As the amplitude of the peak at the forcing frequency of the inlet flow and the impeller perturbations decreases, the amplitudes of the higher harmonics of the perturbation frequency and nonlinear interactions increase.

• The number of nonlinear interaction peaks increase drastically due to a phase angle of π between the forcing frequency of the inlet flow and the impeller perturbations.

• Most of the nonlinear interactions, especially the ones at frequencies higher than two times the blade passing frequency, are attenuated through the vaneless diffuser.

• At off-design operation conditions, the background noise level increases at low frequencies, between zero and the blade passing frequency. This increase may be due to rotating stall.

6. APPENDIX A : DESIGN OF CONTRACTION

The design of the contraction, which is located between the inlet duct and the impeller (see page 75) is according to the following criteria established by Morel (1977) .

The major design criteria are: maintenance of flow uniformity at the exit; avoiding flow separation; and minimizing the exit boundary layer thickness. To achieve these criteria, the following design parameters are available: Length of the contraction; the shape of the wall; and Reynolds number.

There are various wall shapes recommended by Morel (1977), Bell and Mehta (1988) for design of the contraction. These wall shapes can be obtained by using a third order polynomial, a fifth order polynomial, or two matched cubic splines.

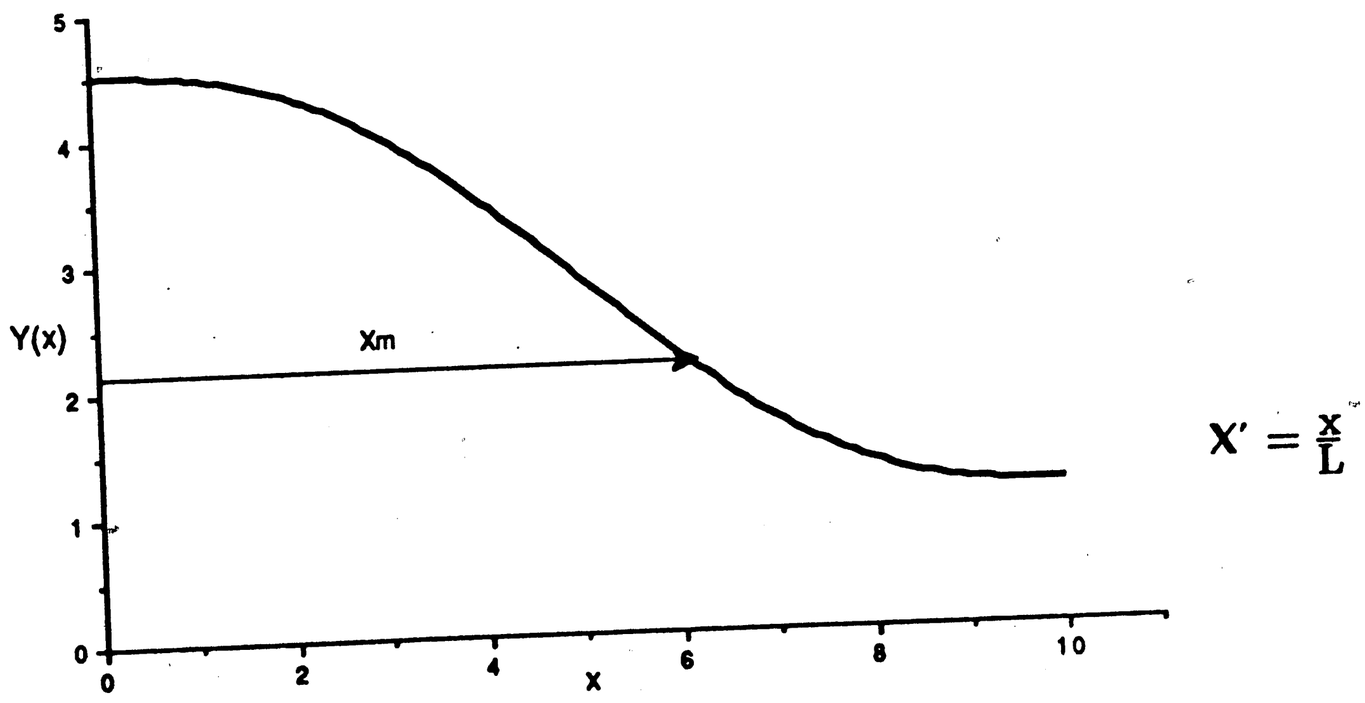

Figure A1: Wall contours constructed of two matched cubic arcs. [Reproduced from Morel, 1976]

For the polynomials, the corresponding equations are :

(1) *Third Order Polynomial* :

$$Y(x) = R_i - (R_i - R_e) * \left(-2(X')^3 + 3(X')^2 \right)$$

(2) *Fifth Order Polynomial* :

$$Y(x) = R_i - (R_i - R_e) * \left(6(X')^5 - 15(X')^4 + 10(X')^3 \right)$$

(3) *Seventh Order Polynomial* :

$$Y(x) = R_i - (R_i - R_e) * \left(-20(X')^7 + 70(X')^6 - 84(X')^5 + 35(X')^4 \right)$$

For the case of two matched cubic splines, Morel (1977) introduces a design method using two cubic splines under the following restrictions.

$X' = \frac{x_m}{L}$, where x_m is the matching point of the two cubic splines.

Subscripts "1" and "2" refer to the inlet and exit conditions, and subscripts "e" and "i" to the maximum and minimum values of wall velocity .

The symbol "CR" represents the area ratio (A_1/A_2); values of CR lie in the range of $2.0 \leq CR \leq 25.0$.

The wall pressure coefficients are defined according to:

$c_{pe} = 1-(U_{2,\infty}/V_e)$ which controls exit velocity uniformity should be in the range of $c_{pi} \leq 0.5$.

$c_{pi} = 1-(V_i/U_{2,\infty})$ which controls the separation near the inlet should lie in the range of $c_{pe} \leq 0.06$.

" L/D_1 " ratio and " X' " should be in the range of $0.75 \leq L/D_1 \leq 1.25$ and $0.20 \leq X' \leq 0.80$ respectively.

The design procedure is as follows :

(a) Choose CR, c_{pi}, c_{pe}

The recommended values of c_{pi} and c_{pe} : $c_{pi} < 0.5$ and $c_{pe} \leq 0.06$

(b) Read F_e from Figure 6.3 for c_{pe} and G_i from Figure 6.4 for c_{pi}

(c) Solve the following equation for X'

$$X'^{1/2}(1-X')^{-2/3} = F_e^{1/3}\, G_i^{-1/2}\, m^{1/2}(m-1)^{1/6}$$

where $m=D_1/D_2$ and $\xi = F_e^{1/3}\, G_i^{-1/2}$

$$X'^{1/2}(1-X')^{-2/3} = \xi\, m^{1/2}(m-1)^{1/6} \quad -$$

(d) $L=\left(G_i\, m\, X'/(m-1)\right)^{-1/2} D_1$

(e) Make sure the restrictions given at the beginning under (a) are satisfied.

(f) Plot the matched cubics using the following equations.

$$\frac{R-R_2}{R_1-R_2} = 1-\frac{1}{X'^2}\left(\frac{x}{L}\right)^3 \qquad x \le x_m$$

$$\frac{R-R_2}{R_1-R_2} = \frac{1}{(1-X')^2}\left(1-\frac{x}{L}\right)^3 \qquad x > x_m$$

The data obtained from each equation is plotted and the fifth order polynomial is chosen for the wall shape of the contraction. The fifth order polynomial is also recommended by Bell and Mehta (1988) for low speeds in terms of minimum separation.

In our case the dimensions of the contraction is as follows:

$D_1 = 9.0$ in $\qquad D_2 = 2.25$ in

CR= 16.0 $\qquad L = 10$ in

$V_1 = 0.5$ in/s $\qquad V_2 = 8.0$ in/s

(1) $Y(x)= 4.5-(4.5\text{-}1.125)*\left(-2(x/10)^3+ 3(x/10)^2\right)$

(2) $Y(x)= 4.5-(4.5-1.125)*\left(6(x/10)^5- 15(x/10)^4+ 10(x/10)^3\right)$

(3) $Y(x)= 4.5-(4.5-1.125)*\left(-20(x/10)^7+ 70(x/10)^6- 84(x/10)^5+ 35(x/10)^4\right)$

(4) CR= 16.0 c_{pi}= 0.4 c_{pe}= 0.05 L= 10 in

X'= 0.4 x_m= 4.0 in L/D_1= 1.11

$$\frac{R-1.125}{4.5-1.125} = 1- \frac{1}{0.4^2}\left(\frac{x}{10}\right)^3 \qquad x \leq x_m$$

$$\frac{R-1.125}{4.5-1.125} = \frac{1}{(1\text{-}0.4)^2}\left(1- \frac{x}{10}\right)^3 \qquad x > x_m$$

7. APPENDIX B : DESIGN OF EXPERIMENTAL SYSTEM

7.1. DESIGN OF IMPELLER

The fluid motion in a centrifugal pump is very complex. Therefore the design procedure is based on some assumptions empirical equations and charts. The overall aim of the designer should be to find the optimal involving dimensions of a pump for a given head and flow rate.

One of the objectives of this research was operating the system at different flow rates. The system did not have to fulfill any head requirements. On the other hand we had the limitations of using Compumotors. The suction rate, in other words the flow rate, was controlled by a Compumotor. The design flow rate is chosen as 8.2614 gpm, this value is based on optimum operation conditions of the Compumotor. The next step was choosing the design flow coefficient. Considering the limitations of the Compumotor, which was driving the impeller, the design flow coefficient was computed. Due to the manufacturing problems the blades are constructed by the Single Arc Method. The blade inlet and exit angles were chosen from the range of widely used and recommended values. The total and theoretical head and the specific speed were calculated. The chosen dimensions of the impeller did not contradict the recommended dimensions, which are generally given as a function of specific speed and flow rate.

Since the research required an investigation of the flow structure in both vaneless and vaned diffusers, predicting the impeller discharge flow conditions

was very important. By introducing the *slip* concept, the discharge conditions were calculated with minimum error.

In the following an abbreviated description of the design process is given in outline form. For detailed explanation of the sequential steps, the reader is referred to the references of, Stepanoff (1957), Lazerkiewicz (1965), Dixon (1978) and Krassik (1986).

Inlet Velocity :

Since the piston velocity is chosen as 0.5 in/s, we can calculate impeller inlet velocity by using the continuity equation.

$D_p = 9.0$ in $\qquad V_p = 0.5$ in/s $\qquad D_1 = 2.25$ in

$$V_p \frac{\pi D_p^2}{4} = V_1 \frac{\pi D_1^2}{4} \qquad \rightarrow V_1 = 8.0 \text{ in/s}$$

Flow Rate :

$$Q = V_1 A_1 = 8.0 \cdot \frac{\pi \cdot 2.25^2}{4} = 31.81 \text{ in}^3/\text{s} \qquad \rightarrow Q = 0.01841 \text{ ft}^3/\text{s}$$

$$\rightarrow Q = 8.2614 \text{ gpm}$$

Inlet-Outlet Area Ratio :

$D_1 = 2.25$ in

$$A_1 = \frac{\pi D_1^2}{4} = \frac{\pi \cdot 2.25^2}{4} = 3.976 \text{ in}^2 \qquad \rightarrow A_1 = 0.0276 \text{ ft}^2$$

$D_{1m} = 1.8125$ in $\qquad b_{1m} = 1.28125$ in

$$A_{1m} = \pi D_{1m} b_{1m} = \pi \cdot 1.8125 \cdot 1.28125 = 7.301 \text{ in}^2$$

$$\rightarrow A_{1m} = 0.0507 \text{ ft}^2$$

$D_2 = 6.75$ in $\qquad b_2 = 0.375$ in

$$A_2 = \pi D_2 b_2 = \pi \cdot 6.75 \cdot 0.375 = 9.949 \text{ in}^2 \qquad \rightarrow A_2 = 0.0552 \text{ ft}^2$$

$$\frac{A_1}{A_{1m}} = 0.545$$

$$\frac{A_{1m}}{A_2} = 0.920$$

$$\frac{A_1}{A_{1m}} \cdot \frac{A_{1m}}{A_2} = \frac{A_1}{A_2} = 0.501$$

Inlet Velocity Triangle :

This is a radial flow impeller, therefore the flow angle α is 90° and the blade angle β_1 is chosen as 20°

$$c_{m1} = c_1 = \frac{Q}{A_1} = \frac{0.01841}{0.0507} \rightarrow c_{m1} = 0.36312 \text{ ft/s}$$

$$\beta_1 = 20^\circ \qquad \alpha_1 = 90^\circ$$

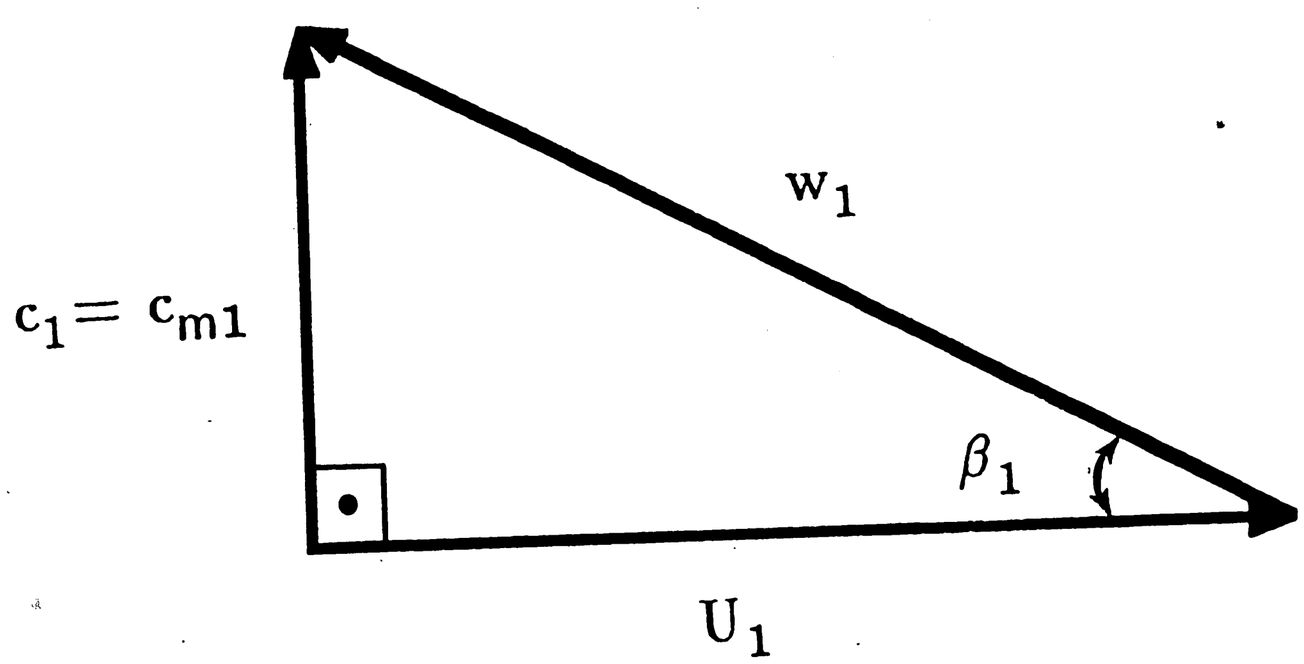

Figure A2: Inlet velocity triangle.

Since we have chosen the inlet blade angle and the flow rate, we can calculate the inlet tangential velocity " U_1", which gives the design RPM of the impeller.

$$tg\beta_1 = \frac{c_{m1}}{U_1}$$

$$U_1 = \frac{c_{m1}}{tg\beta_1} = \frac{0.036312}{tg20^\circ} \rightarrow U_1 = 0.9977 \text{ ft/s}$$

$$U_1 = \pi D_1 n$$

$$n = \frac{U_1}{\pi D_1} = \frac{0.9977}{\pi \cdot (2.25/12)} = 1.694 \text{ rev/s}^- \qquad \rightarrow n = 1.7 \text{ rev/s}$$

$$\rightarrow N = 102 \text{ RPM}$$

$$w_1 = U_1^2 + c_{m1}^2 = 0.9977^2 + 0.36312^2 \qquad \rightarrow w_1 = 1.1276 \text{ ft/s}$$

Outlet velocity triangle :

$D_2 = 6.75$ in $\qquad b_2 = 0.375$ in

$$c_{m2} = \frac{Q}{A_2} = \frac{0.01841}{0.0552} \qquad \rightarrow c_{m2} = 0.3335 \text{ ft/s}$$

$$U_2 = \pi D_2 n = \pi \cdot 6.75 \cdot 1.7 \qquad \rightarrow U_2 = 3.004 \text{ ft/s}$$

$$\beta_2 = 27^\circ$$

$$w_{u2} = \frac{c_{m2}}{tg\beta_2} = \frac{0.3335}{tg27^\circ} \qquad \rightarrow w_{u2} = 0.6545 \text{ ft/s}$$

$$c_{u2} = U_2 - w_{u2} = 3.004 - 0.6545 \qquad \rightarrow c_{u2} = 2.3495 \text{ ft/s}$$

$$tg\alpha_2 = \frac{c_{m2}}{c_{u2}} = \frac{0.3335}{2.3495} \qquad \rightarrow \alpha_2 = 8.08^\circ$$

$$c_2 = c_{u2}^2 + c_{m2}^2 = 2.3495^2 + 0.3335^2 \qquad \rightarrow c_2 = 2.3731 \text{ ft/s}$$

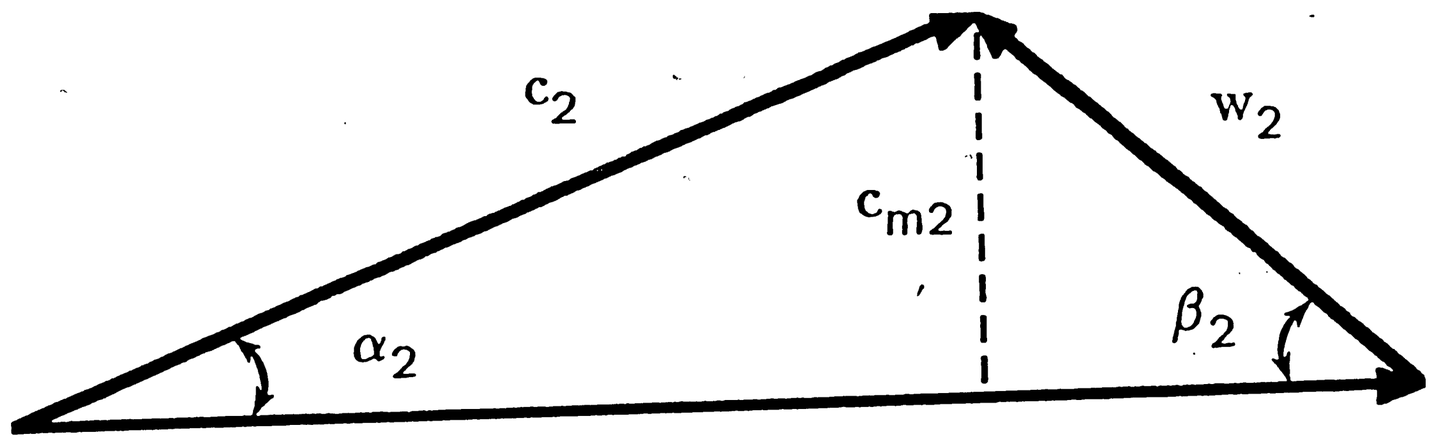

Figure A3: Outlet velocity triangle.

Flow Coefficient :

$$\phi = \frac{Q}{U_2 \cdot A_2} = \frac{0.01841}{3.004 \cdot 0.0552} = 0.111 \qquad \rightarrow \phi = 0.111$$

Theoretical Head :

$$H_{th} = \frac{1}{g}(c_{u2}\, U_2 - c_{u1}\, U_1)$$

$g = 32.2\ ft/s^2$ $\qquad$ $c_{u1} = 0$ since $\alpha_1 = 90^\circ$ (Radial flow)

$$H_{th} = \frac{1}{32.2}\,(2.3495 \cdot 3.004) \qquad \rightarrow H_{th} = 0.2206 \text{ ft}$$

Hydraulic Efficiency :

$$\eta_H = 1 - \frac{0.8}{Q^{0.25}} = 1 - \frac{0.8}{8.2614^{0.25}} \qquad \rightarrow \eta_H = 0.528$$

Slip Factor :

The definition of the slip factor is as follows : Even under ideal frictionless conditions the relative flow leaving a pump impeller receives less than perfect guidance from the vanes and the flow is said to *slip*. (Dixon, 1986)

$z = 6 \qquad \beta_2 = 27^\circ$

$$\mu = 1 - \frac{\pi \text{ Sin } \beta_2}{z} \qquad \text{[STODOLA SLIP FACTOR]}$$

$$\mu = 1 - \frac{\pi \text{ Sin } 27^\circ}{6} \simeq 0.760$$

$$\mu = \frac{1}{1 + \frac{a}{z}\,(1 + \frac{\beta_2}{60})\,\frac{2}{1 - (r_i/r_2)^2}} \qquad \text{[PFLEIDERER SLIP FACTOR]}$$

$$\mu = \frac{1}{1+\frac{0.7}{6}\cdot(1+\frac{27}{60})\cdot\frac{2}{1-(1/3)^2}} \simeq 0.724$$

Coefficient " a " changes with the type of the diffusing system. In our case " a " is chosen as 0.7 .

Volute : 0.65 – 0.85

Vaned Diffuser : 0.6

Vaneless Diffuser : 0.85 – 1.0

After calculating The Slip Factor by the equations given by Stodola and Pfleiderer, The Slip Factor is chosen as ; $\rightarrow \mu = 0.74$

Total Head :

$$H_t = \mu\ \eta_H \frac{U_2^2}{g}\left(1-\frac{c_{m3}}{U_2}\ \mathrm{Cot}\beta_2\right)$$

$$H_t = 0.74 \cdot 0.528 \cdot \frac{(3.004^2/144)}{32.2} \cdot \left(1-\frac{0.3335}{3.004}\cdot \mathrm{Cot}\ 27^\circ\right)$$

$$\rightarrow H_t = 0.1713 \text{ ft}$$

$H_{th} = H_t + \Delta h_p$ where Δh_p is the total losses, such as the losses in the pipes elbows and pump itself.

$$\Delta h_p = H_{th} - H_t = 0.2206 - 0.1713 = \qquad \rightarrow \Delta h_p = 0.0493 \text{ ft}$$

Specific Speed :

$N = 102$ RPM $\quad Q = 8.2614$ gpm $\quad H_t = 0.1713$ ft

$$N_s = \frac{N\sqrt{Q}}{H_t^{3/4}} = \frac{102 \cdot \sqrt{8.2614}}{0.1713^{3/4}} = 1101. \qquad \rightarrow N_s = 1101$$

Number of Blades :

$D_1 = 2.25$ in $\quad D_2 = 6.75$ in

$\beta_1 = 20^\circ \quad \beta_2 = 27^\circ$

$$z = 6.50 * \frac{D_2 + D_1}{D_2 - D_1} * \text{Sin}\left(\frac{\beta_1 + \beta_2}{2}\right)$$

$$z = 6.50 * \frac{6.75 + 2.25}{6.75 - 2.25} * \text{Sin}\left(\frac{20^\circ + 27^\circ}{2}\right) = 5.18 \qquad \rightarrow z = 6$$

Head Coefficient :

$$\psi = \frac{g\, H_t}{U_2^{\,2}} = \mu\, \eta_H \left(1 - \phi\, \text{Cot}\beta_2\right)$$

$$\psi = \frac{32.2 \cdot 0.1713}{3.004^2} \qquad \rightarrow \psi = 0.611$$

Slip Condition :

$U_2 = 3.004$ ft/s $\qquad c_{u2} = 2.3495$ ft/s

$\beta_2 = 27.0^\circ \qquad \alpha_2 = 9.014^\circ \qquad w_{u2} = 0.6545$ ft/s

$$c_{u2}' = \mu\, c_{u2} = 0.74 \cdot 2.3495 \qquad \rightarrow c_{u2}' = 1.7386 \text{ ft/s}$$

$$c_{m2}' = c_{m2} \qquad \rightarrow c_{m2}' = 0.3335 \text{ ft/s}$$

$$\text{tg}\beta_2' = \frac{c_{m2}'}{U_2 - c_{u2}'} = \frac{0.3335}{3.004 - 1.7386} \qquad \rightarrow \beta_2' = 15.0^\circ$$

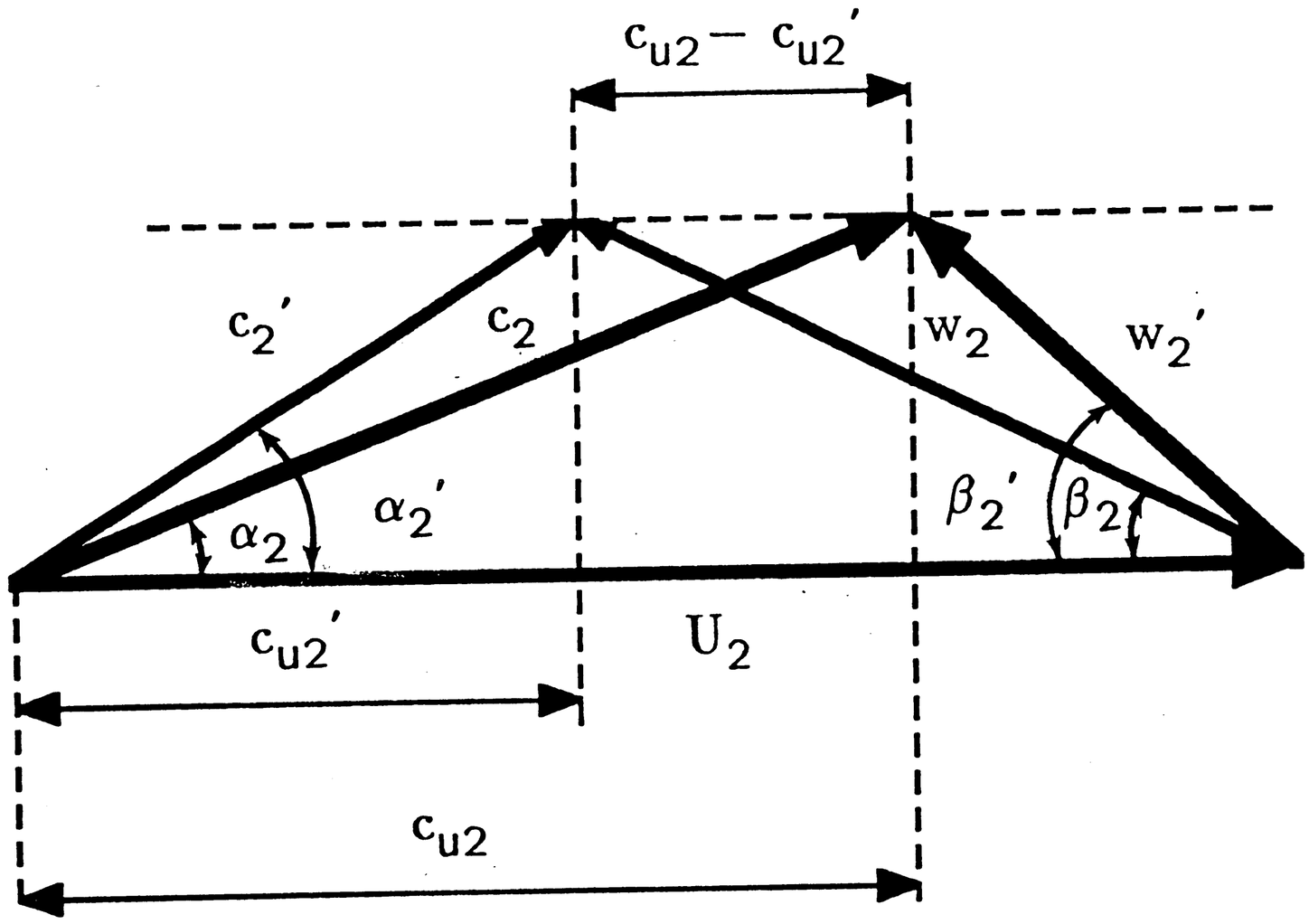

Figure A4: Slip condition.

$$c_2' = \sqrt{c_{u2}'^2 + c_{m2}'^2} = \sqrt{1.7386^2 + 0.3335^2} \qquad \rightarrow c_2' = 1.7703 \text{ ft/s}$$

$$\text{tg}\alpha_2' = \frac{c_{m2}'}{c_{u2}'} = \frac{0.3335}{1.7386} \qquad \rightarrow \alpha_2' = 11.0^\circ$$

$*_2'$ Represents the final exit condition, including the slip. Therefore we will designate them as $*_3$.

$\alpha_2' = \alpha_3$ $\quad c_2' = c_3$ $\quad w_2' = w_3$ $\quad \beta_2' = \beta_3$ $\quad c_{m2}' = c_{m3}$

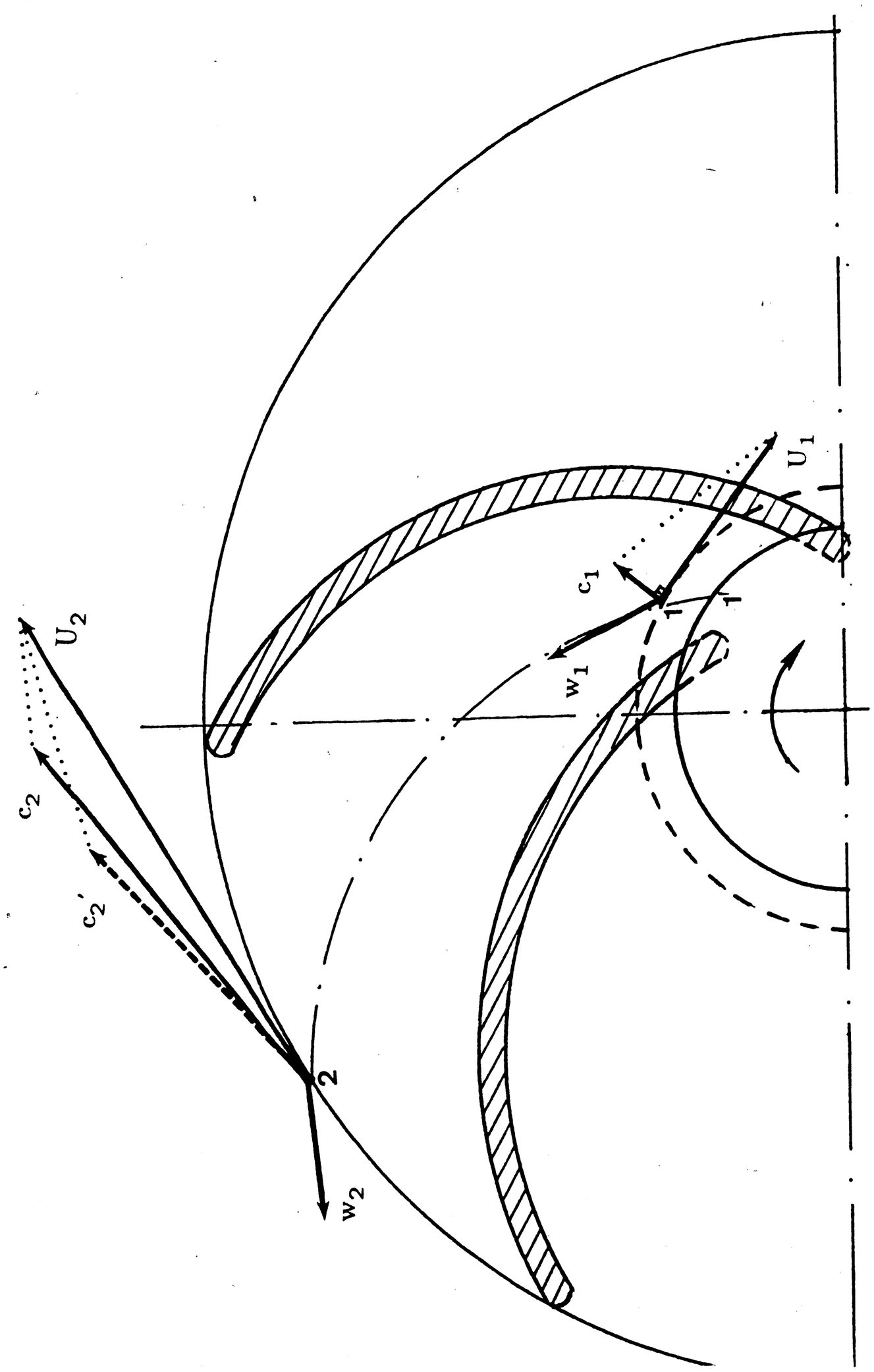

Figure A5: Velocity triangles at the inlet and outlet of the impeller.

Overall Efficiency of The Pump :

$N_s = 1101$ → $\eta = 0.50$

Note that $\eta = \eta_H \cdot \eta_V \cdot \eta_m$

Since η=0.5 and η_H=0.528 → $\eta_V \cdot \eta_m$=0.947 which is high enough.

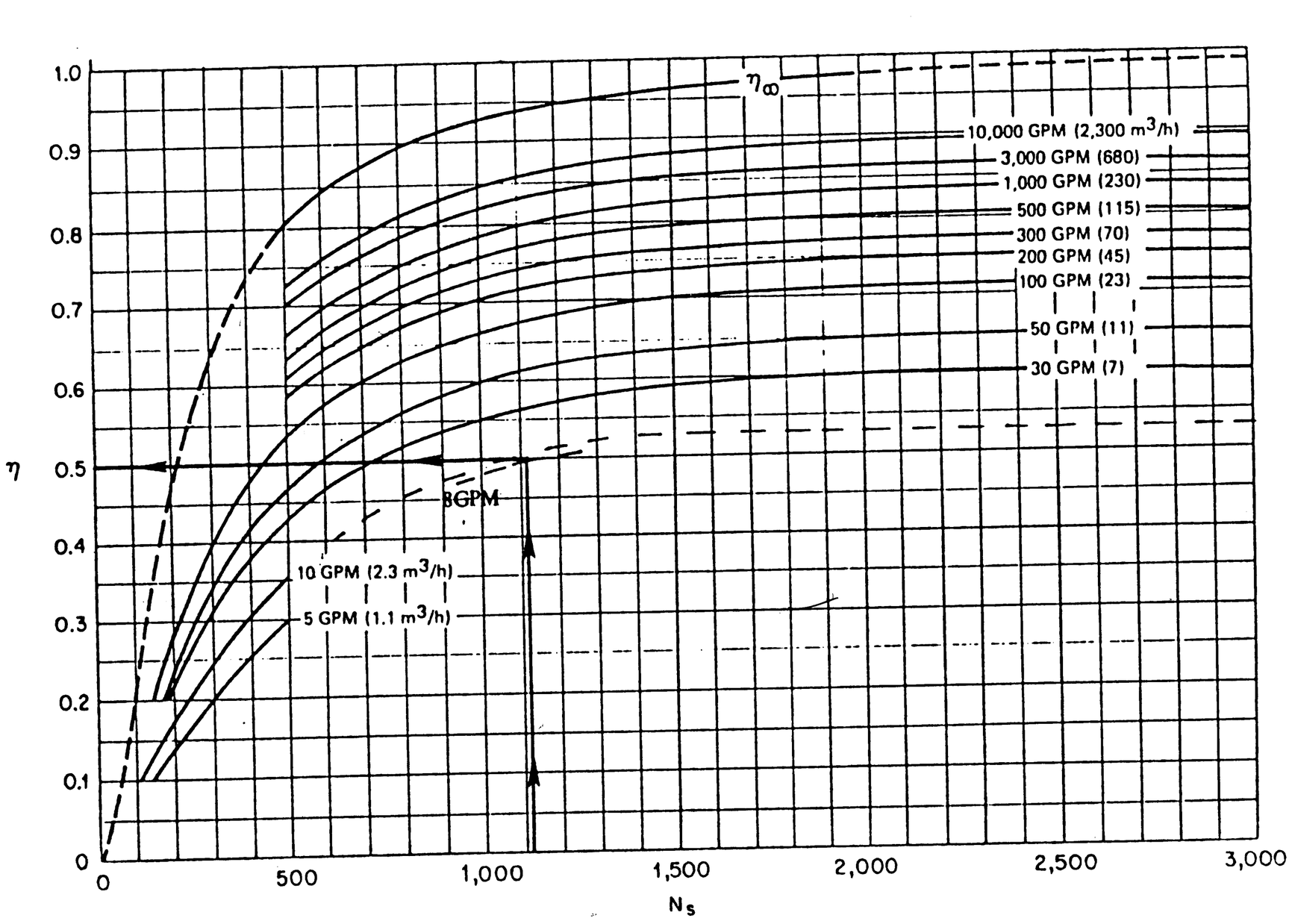

Figure A6: Efficiency as a function of specific speed and flow rate. [Reproduced from Karassik, 1986]

Impeller Discharge Angle :

$N_s = 1101$ - $\rightarrow \beta_2 = 27.0^\circ$

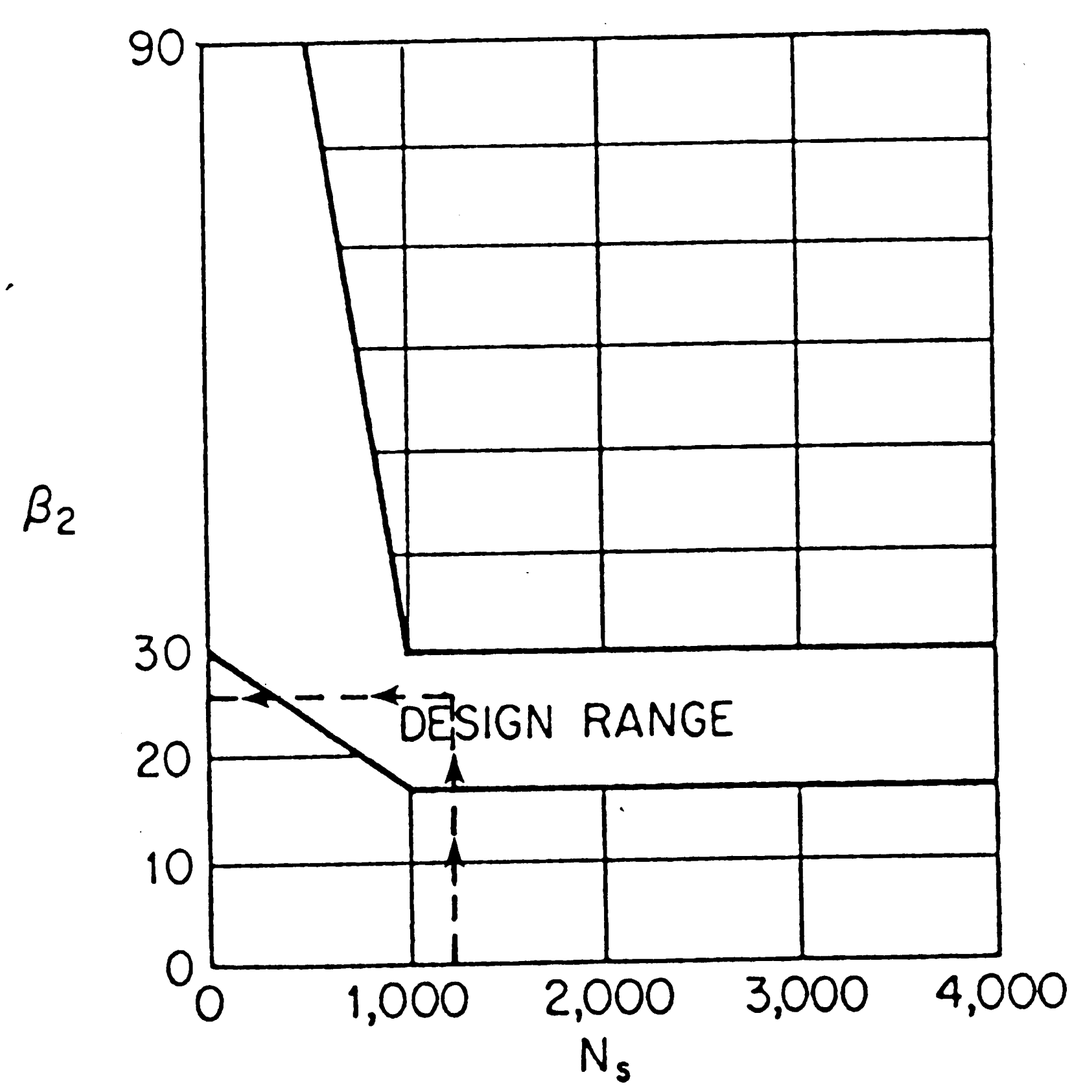

Figure A7: Impeller discharge blade angle versus specific speed.
[Reproduced from Karassik, 1986]

Design Flow Coefficient :

$$N_s = 1101 \qquad - \qquad \rightarrow \phi = 0.111$$

$$\frac{c_{m3}}{U_2} = \frac{c_{m2}}{U_2} = \phi$$

The design flow coefficient is slightly above the design range, which is recommended by Krassik (1986).

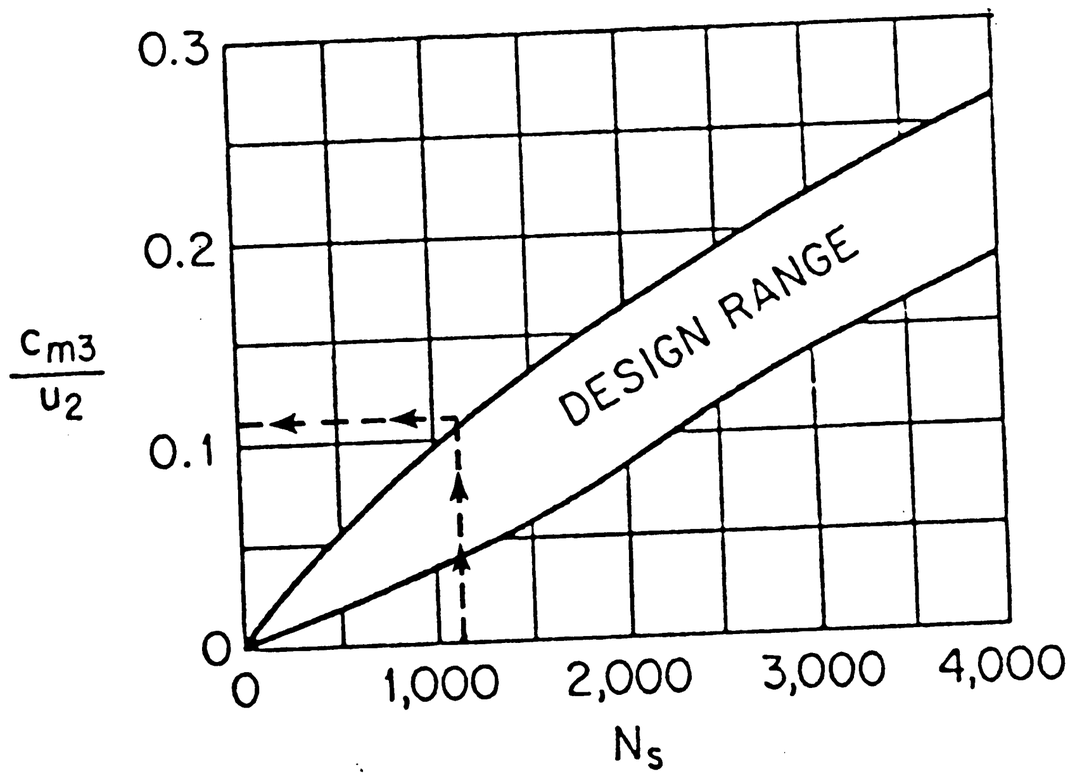

Figure A8: Flow coefficient versus specific speed.
[Reproduced from Karassik, 1986]

7.2. DESIGN OF VANELESS DIFFUSER

Liquid leaves the impeller with a relatively high velocity. There are different ways to reduce the velocity or, in other words, to diffuse the flow. The simplest and fist efficient method is use of a vaneless diffuser. The vaneless diffuser consists of two smooth discs. The distance between the discs, the breadth of the diffuser, can be constant or increase slightly towards the outlet. The breadth of the diffuser is generally smaller than the breadth of the impeller discharge. The leading edges of the discs are rounded in order to create a jet flow at the diffuser inlet. The aim of creating the jet flow is to reduce the losses at the inlet and maintain uniform flow in the diffuser.

The proportion of kinetic energy converted into pressure energy depends on the area ratio, A_2/A_5 where A_2 and A_5 correspond to the discharge area of the impeller and the vaneless diffuser. The loss of energy due to friction depends on the smoothness of the surfaces and the length of the path the liquid must follow. The outside diameter of the diffuser is chosen slightly large so it can also be used as a vaned diffuser.

Dimensions of The Diffuser :

$D_2 = 6.75$ in

The magnitude of the radial clearance between the impeller blades and the diffuser ring is chosen as 3.7% of the impeller radius. $\frac{D_3 - D_2}{2} = 0.0625$ in

Therefore $D_3 = 6.875$ in

The optimum value of the outside diameter of the vaneless diffuser , in terms of friction losses, is given as $D_5 = (1.4 \simeq 1.7)\, D_2$ or $\frac{D_5}{D_2} < 2.0$.

$D_5 = 11.0$ in

$\frac{D_5}{D_2} = 1.63$

$b_2 = 0.375$ in

The breadth of the diffuser is 10% smaller than the breadth of the impeller outlet; $\frac{b_3}{b_2} = 0.9$.

$b_3 = 0.3375$ in

Area Ratios :

$$\frac{A_3}{A_2} = \frac{\pi\, D_3\, b_3}{\pi\, D_2\, b_2} = \frac{6.875 \cdot 0.3375}{6.75 \cdot 0.375} \qquad \rightarrow \frac{A_3}{A_2} = 0.92$$

$b_3 = b_4 = b_5 = 0.3375$

$$\frac{A_5}{A_3} = \frac{\pi\, D_5\, b_5}{\pi\, D_3\, b_3} = \frac{11.0}{6.875} \qquad \rightarrow \frac{A_5}{A_3} = 1.60$$

62.5% of the flow is diffused in the vaneless diffuser.

$$\rightarrow \frac{c_{m5}}{c_{m3}} = 0.625$$

$$\frac{A_5}{A_2} = \frac{A_3}{A_2} \cdot \frac{A_5}{A_2} = 0.92 \cdot 1.60 \qquad \rightarrow \frac{A_5}{A_2} = 1.47$$

$$\rightarrow \frac{c_{m5}}{c_{m2}} = 0.682$$

7.3. DESIGN OF VANED DIFFUSER

The vaned diffuser has a series of symmetrically spaced vanes forming gradually widening passages, in which the velocity of flow is reduced and the kinetic energy is converted into pressure energy.

In our experimental system, the main dimensions of the diffuser are chosen since we decided to use the vaneless diffuser discs as the hub and shroud of the vaned diffuser. These adjustable discs allowed us to change the angle of attack of the diffuser blade and the gap between the diffuser inlet and the the leading edge of its blade.

The gap between the leading edge of the diffuser blade and the inlet of the diffuser is chosen as 0.0625 in.

$D_2 = 6.750$ in. $\qquad b_2 = 0.3750$ in.

$D_3 = 6.875$ in. $\qquad b_3 = 0.3375$ in.

$D_4 = 7.0$ in. $\qquad b_4 = 0.3375$ in.

$D_5 = 11.0$ in. $\quad b_5 = 0.3375$ in.

Design of The Diffuser Blade :

$D_2 = 6.750$ in. $\quad b_2 = 0.375$ in. $\quad \beta_2 = 27.0^\circ$

$D_3 = 6.875$ in. $\quad b_3 = 0.3375$ in.

$c_{u3} = 1.7386$ ft/s $\quad \alpha_3 = 11.0^\circ$

$$\text{tg } \alpha_4 = K_3 \frac{t_4}{t_4 - s_{u4}} \text{ tg } \alpha_3$$

" K_3 " is the constriction coefficient for the inlet. K_3 depends on the number of vanes and on the blade outlet angle of the impeller. $K_3 \simeq 1.5 - 2.0$ for $\beta_2 \leq 30.0^\circ$ (Lazerkiewicz, 1965)

Let $\frac{t_4}{t_4 - s_{u4}} = 1.2$ and $K_3 = 1.3$

The number of the diffuser blades is chosen as 8.

$z_d = 4$ $\quad t_4 = \frac{\pi D_4}{z_d} = \frac{\pi \cdot 7.0}{8} = 2.7489$ in.

$\text{tg } \alpha_4 = 1.3 * 1.2 * \text{tg } 11.0^\circ \quad \alpha_4 = 16.7^\circ$

Choose s_4 as $s_4 = 0.0625$ in.

$$s_{u4} = \frac{s_4}{\text{Sin } \alpha_4} = \frac{0.0625}{\text{Sin } 16.7^\circ} = 0.2175$$

$$\frac{t_4}{t_4 - s_{u4}} = \frac{2.7489}{2.7489 - 0.2175} = 1.086$$

$$\text{tg } \alpha_4 = 1.3 * 1.086 * \text{tg } 11.0^\circ \qquad \rightarrow \alpha_4 = 15.0^\circ$$

7.4. DESIGN OF VOLUTE

A correctly designed volute, combined with a diffuser, helps to increase the efficiency of a pump. The shape of the volute is very important in order to produce small hydraulic losses. The basic function of the volute is to collect the liquid at the discharge of the impeller or diffuser. It is the last stage to convert the remaining kinetic energy into pressure energy. In our experimental system the aim of the volute was to collect the flow at the discharge of the diffuser rather than diffusing the flow. Without the volute, the liquid is introduced into the tank at the diffuser discharge where the velocity of the liquid can be considered as zero. In order to create more realistic experimental conditions a rectangular collector, with gradually increasing cross-section area from the throat to the exit, is designed. This straight walled collector also eliminated the affects of possible fluctuations caused by the gear-chain system.

In order to maintain full visual access, the collector is machined out of plexiglass. The front disc of the diffuser is replaced by the wall of the collector so the leakage between the diffuser ring and the collector wall is prevented.

The method of designing the volute is base on the assumption that the flow in the volute obeys the principle of constant moment of momentum.

$$M = c_u \cdot r = \text{constant} \qquad c_{u5} \cdot r_5 = c_{thr} \cdot r_{thr}$$

Assume that $\frac{A_{thr}}{A_{II}} \simeq 0.4$ where A_{II} is the total discharge area; in our case it is the diffuser discharge area.

$$A_{II} = A_5 = \pi\, D_5\, b_5 = 0.09 \text{ ft}^2$$

$$A_{thr} = 0.09 * 0.4 = 0.036 \text{ ft}^2 = 5.184 \text{ in}^2$$

Since the collector is rectangular; $A_{thr} = x_{thr} * h_{thr} = x^2_{thr}$

$$x^2_{thr} = 5.184 \text{ in}^2 \quad \rightarrow \quad x_{thr} = 2.28 \text{ in.}$$

Since " x" is constant , choose $x = 2.25$ in. $\rightarrow A_{thr} = 5.0625 \text{ in}^2$

$$r_{thr} = r_5 + t + \frac{h_{thr}}{2} = r_5 + t + \frac{x_{thr}}{2} = r_5 + t + \frac{x}{2}$$

" t " is chosen as $t = 0.1875$ in.

$$r_{thr} = 5.5 + 0.1875 + 1.125 = 6.8125 \text{ in.}$$

$$A_{v^\circ} = A_{thr} \cdot \frac{\gamma_{v^\circ}}{360^\circ} \qquad \frac{A_{v^\circ}}{x} = h_{v^\circ}$$

$$r_{v^\circ} = 5.5 + 0.1825 + \frac{h_{v^\circ}}{2}$$

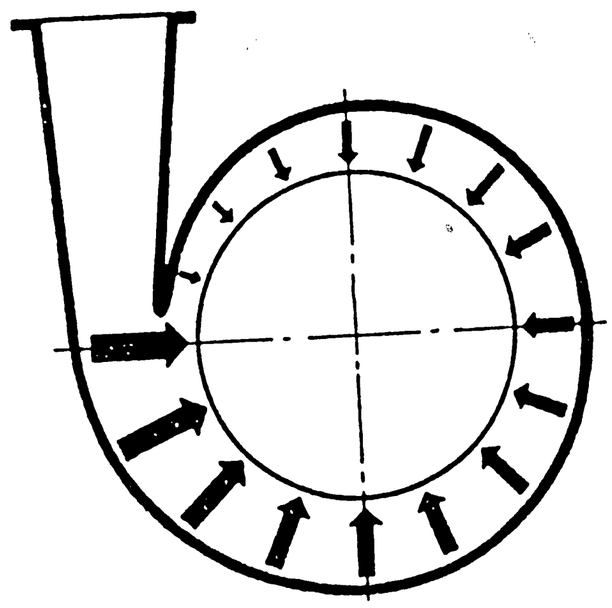

Figure A9: Pump volute.

γ_{v°	r_{v°
0°	$5.5 + 0.1825$
10°	$5.5 + 0.1825 + 0.03125$
..	.....
..	.....
355°	$5.5 + 0.1825 + 1.1094$

The angle of the exit walls of the collector is chosen as 5.0° .

8. APPENDIX C : MECHANICAL AND ELECTRICAL NOISE

After designing the experimental system, one of the biggest problems was eliminating, or at least decreasing, the noise level. In some cases, the overall amplitude of the noise spectrum was higher than the amplitude of the peaks related to the flow. We had to deal basically with both mechanical and electrical noise. High frequency noise is filtered out by an analog filter irrespective of the source. The most difficult problem was finding out the sources of the low frequency noise and bringing the level of the noise to a reasonable value.

8.1. MECHANICAL NOISE

It was very difficult to predict the amplitude and frequency of the mechanical noise at the design stage. Two Compumotors were the main sources of the mechanical noise. Therefore we took some basic precautions in order to damp, or at least minimize, the level of the mechanical vibrations transmitted to the other components of the system. Since the components of the system are connected to each other, the vibrations can be transmitted easily.

The first precaution was using rubber shock absorbers at the connection of each component within the experimental system. Most of the vibrations are transmitted through the steel frame. Therefore the entire system, especially the tank, is supported by rubber shock absorbers.

Since we were trying to damp the vibrations at very low frequencies (<15

Hz) it was difficult to find commercial shock absorbers that would be useful in that frequency range. Therefore we decided to use natural rubber without considering the absorbing range.

None of the Compumotors were in direct contact with the frame. The first motor was connected to the ball bearing screw with an elastic coupling. The second motor is mounted on an aluminum beam which was sitting on the tank. The connection between the beam and the tank is supported by rubber shock absorbers.

The second source of the mechanical noise was the piston-cylinder system. At the beginning, the piston was guided by a plexiglass rod. Due to the flexibility of Plexiglass, the rod could be bend easily and force the piston to tilt inside the cylinder. We replaced the plexiglass rod with a steel rod and increased the length of the piston so that it would not tilt. This application had a significant effect on the noise level, but it was still high.

The piston was sealed with two rubber O-rings in order to prevent the leakage between the piston and the cylinder. We could not find a way to lubricate the surface between the rubber O-rings and the plexiglass cylinder. The lubricant could either dissolve in water or make the particles, that are used for the laser techniques, stick on the inner surface of the cylinder. We increased the clearance between the cylinder and the piston, but the noise level was still high and it started to leak. Therefore we decided to use teflon O-rings instead of rubber. The self lubricating characteristics of Teflon decreased the surface friction. Due to the change in the surface friction, the noise level decreased

drastically.

The ball bearing and the screw were the other noise sources. In order to be able to change the motor and the screw without interfering with the other components of the system, one end of the screw was left free. The idea of supporting the screw, somehow, increased the noise level. We put some grease both on the screw and the rods which were guiding the table.

The second Compumotor, which was driving the impeller with a gear-chain system, was another source of mechanical noise. We designed the connection between the impeller and the contraction very carefully so that the impeller would either tilt because of high clearance or stall because of low clearance. We also used a plastic coated steel chain instead of a regular steel chain. The preliminary experiments proved that the level of the noise, generated at this part of the system, was relatively low.

Finally the mechanical noise level is brought to the electrical noise level. But this time it became impossible to distinguish the mechanical noise from the electrical noise on the spectra. Therefore the preliminary experiments, which are focused on decreasing the noise level, and their results will be explained in the electrical noise section.

8.2 ELECTRICAL NOISE

Eliminating the electrical noise was more challenging than the mechanical noise. The first problem was detecting the sources of the electrical noise. It is

known that the electrical noise can be transmitted through the cables or in the form of radiation.

Each electronic equipment can be considered as a source of noise; including the lighting system of the lab. The major sources of noise were the Compumotors and their drives. However, the computer itself was generating noise. It was impossible to eliminate the electrical noise generated inside the computer. Therefore we focussed on the Compumotors and their drives. Some of the cables were transmitting the noise or picking up the noise like an antenna. The computers and other electronic lab or office equipment, running in the building, had a big effect on the overall noise level. The only way to get rid of this noise was to work at night, when most of the equipment was off.

We could decrease the noise level about 50% by applying the following procedure.

▷ *Choose the right set up.*

Choosing the right set up can change the noise level drastically. Never cross two or more cables, otherwise even if you shield them, they may work like an antenna and pick up all the radiation noise. Keep the data transmitting cables, especially the cable between the transducer and the scope, away from the power cables and noise generating equipment. If it is possible use a different power source for your data acquisition equipment.

▷ *Shield some of your cables and equipment depending on your set up.*

Try to use low noise coaxial cables.- If you already have the cables connected to your equipment, such as the power cables, then shield them. There are different types of shielding materials, such as aluminum or lead. There are also some commercial tapes available for electrical noise insulation. In our experimental system we shielded the cables with aluminum foil and then covered them with a plastic tubing.

Shielding the noise sources, in our case the Compumotors and their drives, can be considered as an alternative. But these are delicate equipment, designed in a way that they totally depend on air cooling, and the air circulation may be inadequate. Therefore you may be risking the equipment by shielding.

Keep the A/D converter away from the noise sources. Try to minimize the length of the cable between the A/D converter and the computer. Shield the A/D converter and the cables connected to it. We obtained a big decrease in the noise level after shielding the A/D converter with aluminum foil.

▷ *Ground your equipment and use isolation transformer.*

Use an isolation transformer for the equipment requiring high power. In our case we used three isolation transformers: Two for the Compumotor drives; and one for the computer. The isolation transformer blocks the electrical noise coming from the main power supply and protects the equipment against power fluctuations.

Ground the noise generating equipment and do not forget to shield the grounding cables. In our experimental system, we used a wide brass cable to ground the Compumotor drives and the computer.

During the preliminary experiments, we have been able to decrease the overall amplitude range of the electrical and mechanical noise level from 10^{-2} to 10^{-4}.

8.3. ELIMINATING RANDOM NOISE

Another attempt to eliminate the random noise was subtracting its spectrum from the flow spectrum. The idea behind this technique was obtaining a random noise spectrum, which was the ensemble average of six samples of noise data, then subtracting it from the flow spectrum, which also had some random noise in it.

We used an identical dummy transducer and transducer mount for this application. The sensitivities of the transducers were slightly different, but we calibrated both noise and flow voltage data.

The dummy transducer was initially mounted on the same ring (see page 87) at the exit of the impeller, as shown in Figure 8.1. The diaphragm of the dummy transducer was facing towards the wall of the tank instead of the impeller discharge. But the experiments revealed that the dummy transducer was still picking up the flow induced fluctuations. A small cylinder with small holes at one end was mounted in front of the pressure transducer mount. The

fluctuations generated by the flow were damped by those holes so that we could get pure noise data (Figure 8.2). After ensemble averaging the spectrum of ten repeats of this case, we obtained the final noise spectrum. At some frequencies the amplitude of the noise spectrum exceeded the amplitude of the flow spectrum.

The next step considered was to average the fluctuating noise spectrum, as shown in Figures 8.3 and 8.4, and obtain a smoothed curve so that we could subtract the amplitude of the curve from the amplitude of the flow spectrum. The mean amplitude of the noise spectrum was about 10^{-4}, and the mean amplitude of the flow spectrum was about 10^{-3}. Since the difference between 10^{-3} and 10^{-4} is negligible, we could not see a big decrease in the noise level (Figure 8.5). This result supports the fact that the fluctuations on the flow spectra are generated by the flow itself but not by the mechanical or electrical noise.

The electrical noise level, during the LDV measurements, was very low (Figure 8.6).

9. REFERENCES

Abdelhamid, A. N., Colwill, W. H. and Barrows, J. F. 1979 "Experimental Investigation of Unsteady Phenomena in Vaneless Diffusers", Transactions of the ASME, Vol. 101, pp. 52-60.

Arndt, N., Acosta, A. J., Brennen, C. E. and Caughey, T. K. 1983 "Rotor-Stator Interactions in a Diffuser Pump", ASME 5/83.

Bell, J. H. and Mehta, R. D. 1988 "Contraction Design for Small Low-Speed Wind Tunnels", Dept. of Aeronautics and Astronautics, Stanford Univ., Stanford, CA, JIAA Rept. TR-84.

Bell, J. H. and Mehta, R. D. 1988 "Boundary Layer Predictions for Small Low-Speed Contractions", AIAA Journal, Vol. 27, No. 3, pp. 372-374.

Binder, A., Forster, W., Mach, K. and Rogge 1986 "Unsteady Flow Interactions Caused by Stator Secondary Vortices in a Turbine Rotor", ASME Paper, No. 86-GT-302.

Choi, J-S., McLaughlin, D. K. and Thompson, D. E. 1990 "Experiments on the Aerodynamic Noise Sources in Centrifugal Turbomachinery", AIAA 13th Aeroacoustics Conference, AIAA-90-3948.
Dixon, S. L. 1986 "Fluid Mechanics Thermodynamics of Turbomachinery", New York: Pergamon Press Ltd.

Doebelin, E. O. "Measurement Systems Application and Design Third Edition", New York: McGraw-Hill Book Company.

Dutton, J. C., Piemsomboon, P. and Jenkins, P. E. 1986 "Flowfield and Performance Measurements in a Vaned Radial Diffuser", Journal of Fluids Engineering, Vol. 108, pp. 141-147.

Evans, R. L. 1974 "Turbulance and Unsteadiness Measurements Downstream of a Moving Blade Row", ASME Paper, No. 74-GT-73.

Gopalakrishnan, S. 1988 "A New Method For Computing Minimum Flow", Byron Jacson Products BW/IP International, Inc., LA, California.

Inoue, M. and Cumpsty, N. A. 1984 "Experimental Study of Centrifugal Impeller Discharge Flow in Vaneless and Vaned Diffusers", Journal of Engineering for Gas Turbines and Power, Vol. 106, pp. 455-467.

Johnson, M. W. and Moore, J. 1979 "The Development of Wake Flow in a Centrifugal Impeller", ASME Paper, No. 79-GT-152.

Karassik, I. J., Krutzsch, W. C., Fraser, W. H. and Messina, J. P. 1986 "Pump Handbook Second Edition", New York: McGraw-Hill Book Company.

Kemp, N. H. and Sears, W. R. 1953 "Aerodynamic Interference Between Moving Blade Rows", Journal of the Aeronautical Sciences, Vol. 20, No.9, pp.585-597.

Kinoshita, Y. and Senoo, Y. 1985 "Rotating Stall Induced in Vaneless Diffusers of Very Low Specific Speed Centrifugal Blowers", Transactions of the ASME, Vol. 107, pp. 514-521.

Kline, S. J. and Johnson, J. P. "Diffusers - Flow Phenomena and Design", Stanford University, Chp. 6.

Krain, H. 1981 "A Study on Centrifugal Impeller and Diffuser Flow", Transactions of the ASME, Vol. 104, pp. 688-697.

Lazarkiewicz, S. and Troskolanski, A. T. 1965 "Impeller Pumps", New York: Pergamon Press Ltd.

Lefcort, M. D. 1965 "An Investigation Into Unsteady Blade Forces in Turbomachines", Journal of Engineering for Power, pp. 345-354.

Lennemann, E. and Howard, J. H. G. 1968 "Unsteady Flow Phenomena in Rotating Centrifugal Impeller Passages", ASME Paper, No. 69-GT-35.

Lorett, J. A. and Gopalakrishnan, S. 1986 "Interaction Between Impeller and Volute of Pumps at Off-Design Conditions", Transactions of the ASME, Vol. 108, pp.12-18.

Meyer, R. X. 1957 "The Effect of Wakes on the Transient Pressure and Velocity Distributions in Turbomachines", ASME Paper, No. 57-A-83.

Mizuki, S., Hattori, T., Ariga, I. and Watanabe, I. 1976 "Reversed Flow Phenomena Within Centrifugal Compressor Channels at Lower Flow Rate", ASME Paper, No. 76-GT-86.

Morel, T. 1975 "Comprehensive Design of Axisymmetric Wind Tunnel Contractions", Journal of Fluids Engineering, pp. 225-233.

Morel, T. 1976 "Design of Two-Dimensional Wind Tunnel Contraction", ASME Paper, no. 76-WA/FE-4.

Murakami, M. and Heya, N. 1966 "Swirling Flow in Suction Pipe of Centrifugal Pumps", Bulletin of JSME, Vol. 9, No. 34, pp. 328-337.

Neise, W. 1976 "Noise Reduction in Centrifugal Fans: A Literature Survey", Journal of Sound and Vibration, Vol. 45(3), pp. 375-403.

Newland, D. E. 1987 "An Introduction to Random Vibrations and Spectral Analysis Second Edition", New York: Longman Scientific & Technical.

Otugen, M. V. and Hwang, B. C. 1988 "The Effect of Diffuser Geometry on Rotating Stall Behavior", ASME Paper, No. 88-GT-153.

Paone, N., Riehmuller, M. L. and Van den Braembussche 1989 "Experimental Investigation of the Flow in the Vaneless Diffuser of a Centrifugal Pump by Particle Image Displacement Velocimetry", Experiments in Fluids, Vol. 7, pp. 371-378.

Rao. K. V. 1975 "Secondary Flow in a Curved Channel as Revealed by a Laser Doppler Anemometer", Proceedings of the LDA Symposium, pp.710-734.

Schlichting, H. 1979 "Boundary Layer Theory Seventh Edition", New York: McGraw-Hill Book Company.

Senoo, Y., Hayami, H. and Ueki, H. 1983 "Low-Solidity Tandem-Cascade Diffusers for Wide-Flow-Range Centrifugal Blowers", ASME Paper, No. 83-GT-3.

Shersstyuk, A. N. and Kosmin V. M. "The Effect of the Slope of Vaneless Diffuser Walls on the Characteristics of a Mixed-Flow Compressor", Paper No. UDC 542.78, pp.116-121.

Stepanoff, A. J. 1957 "Centrifugal and Axial Flow Pumps", New York: John Wiley & Sons, Inc.

Tulapurkara, E. G. and Bhalla, V. V. K. 1988 "Experimental Investigation of Morel's Method for Wind Tunnel Contractions", Journal of Fluids Engineering, Vol. 110, pp. 45-47.

Watson, N. and Ingham, D. R. "Compressible Flow in a Radial Vaneless Diffuser", The Hatfield Polytechnic, Paper No. 8.

Yingkang, Z. and Sjolander, S. A. 1987 "Effect of Geometry on the Performance of Radial Vaneless Diffusers", Transactions of the ASME, Vol. 109, pp. 550-556.

Yedidiah, S. 1986 "Certain Effects of Recirculation on Cavitation in Centrifugal Pumps", Proc. Instn. Mech. Engrs., Vol. 200, No. A4, pp. 283-292.

Ziada, Z. and Rockwell, D. 1982 "Vortex-Leading-Edge Interactions", Journal of Fluid Mechanics, Vol. 118, pp.79-107.

LIST OF FIGURES

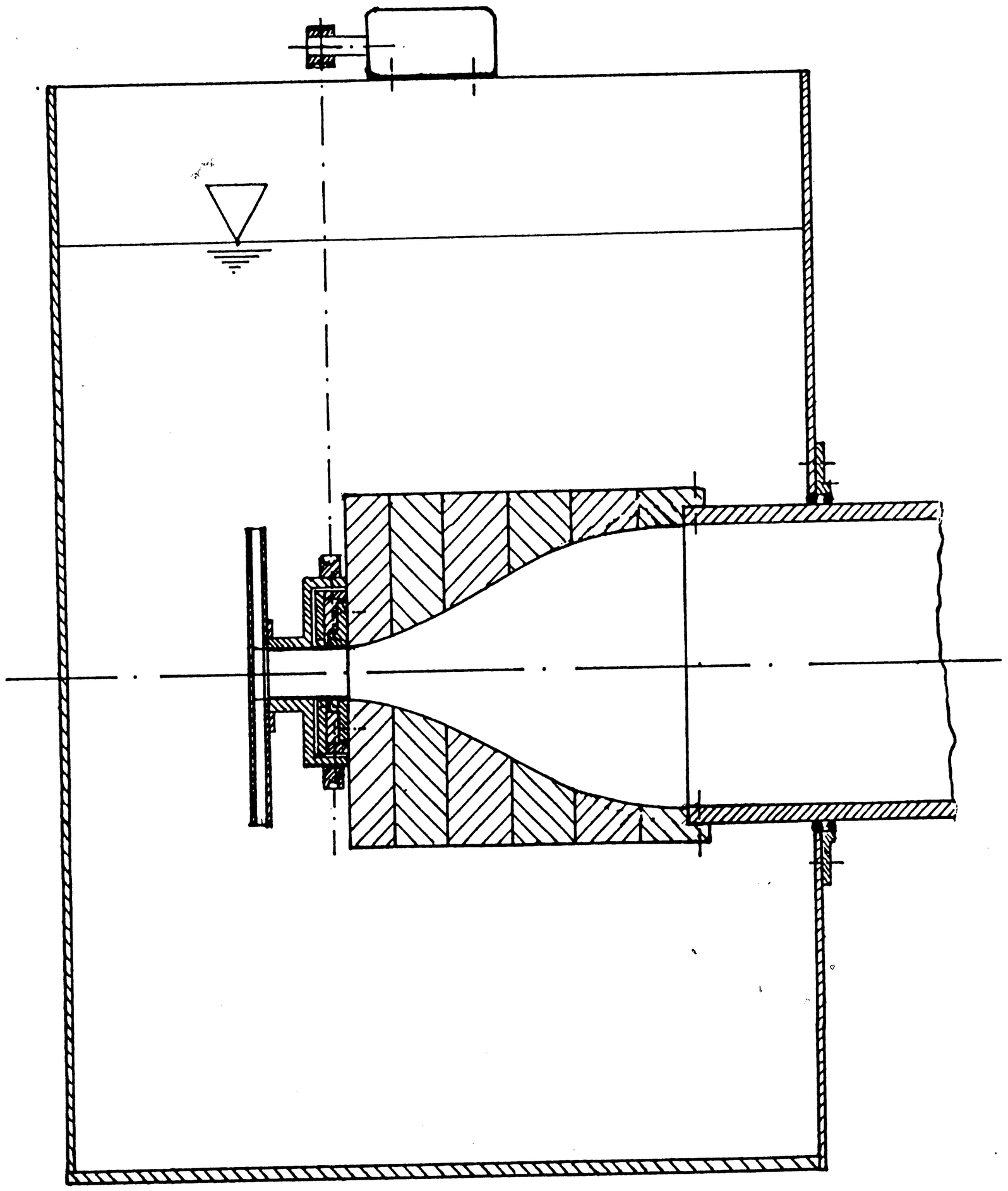

Figure 2.1.a: Inlet part of the experimental system including the impeller and the contraction.

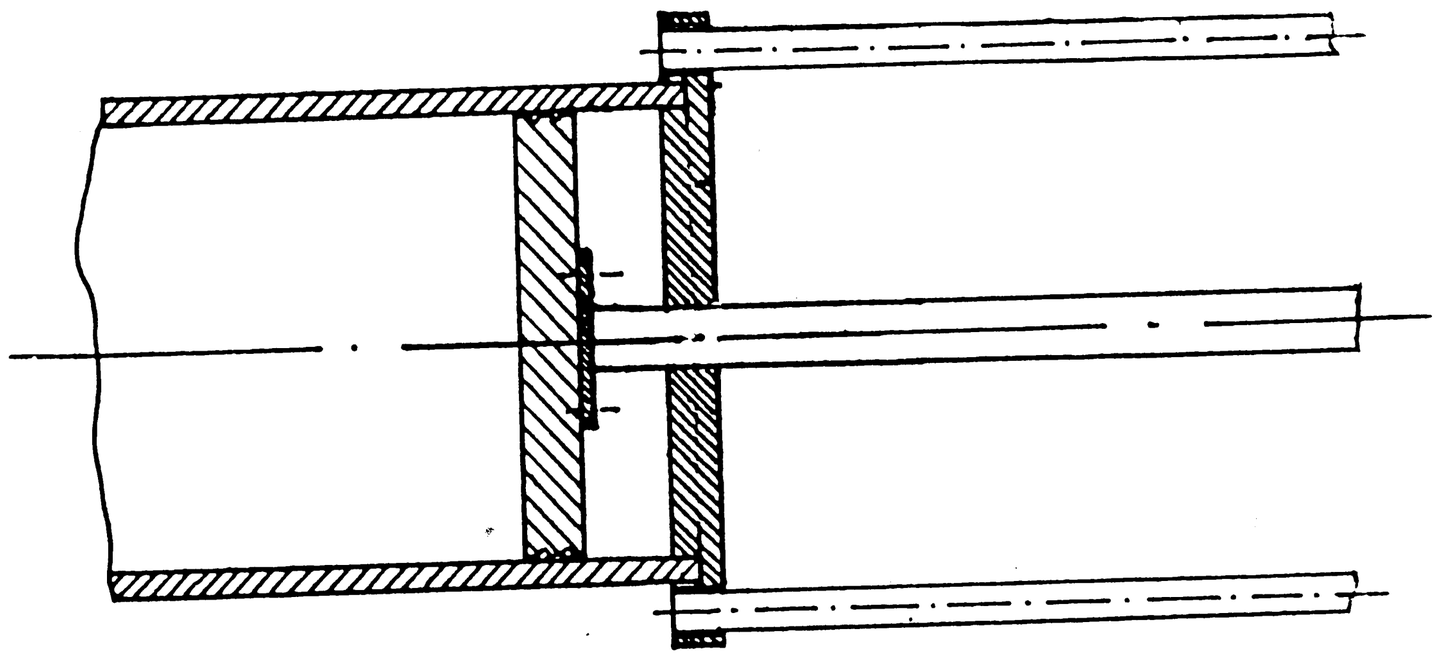

Figure 2.1.b: Mid section of the experimental system including the piston and the cylinder.

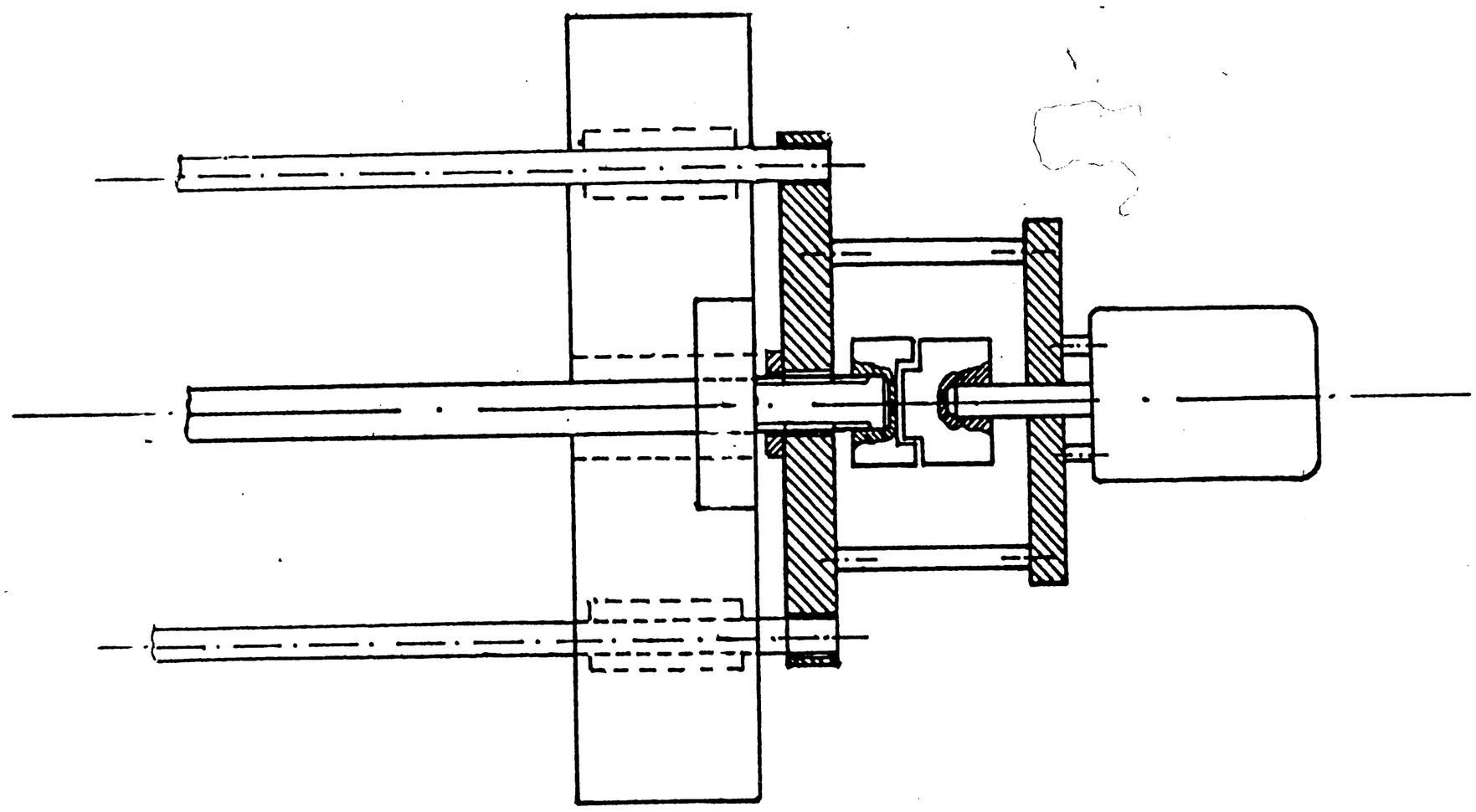

Figure 2.1.c: Rear part of the experimental system; Compumotor and the table which pushes the piston.

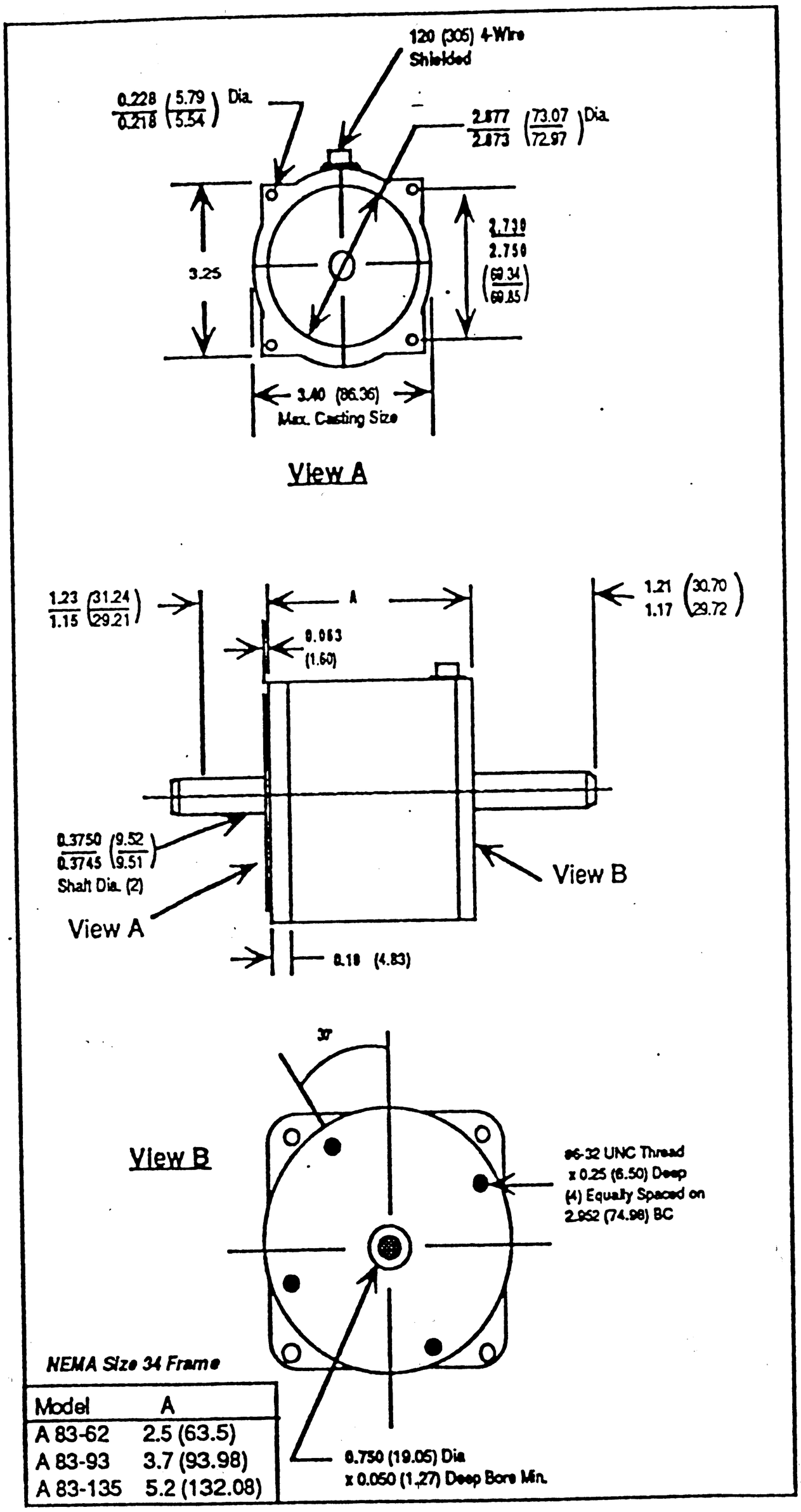

Figure 2.2: **Dimensions of the Compumotor.**
[Reproduced from PCB Piezotronics, Inc. Manual]

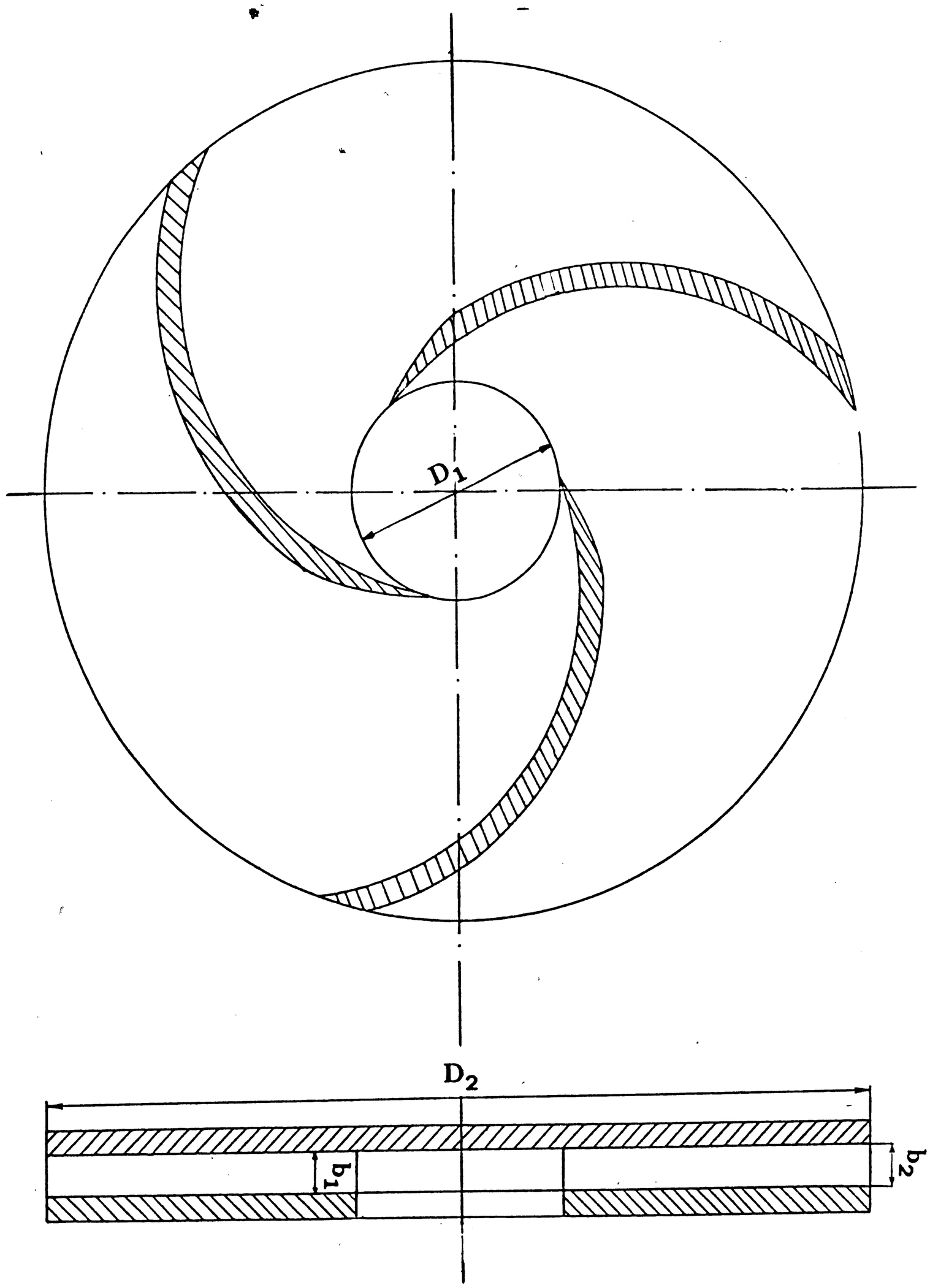

Figure 2.3: Three blade impeller.

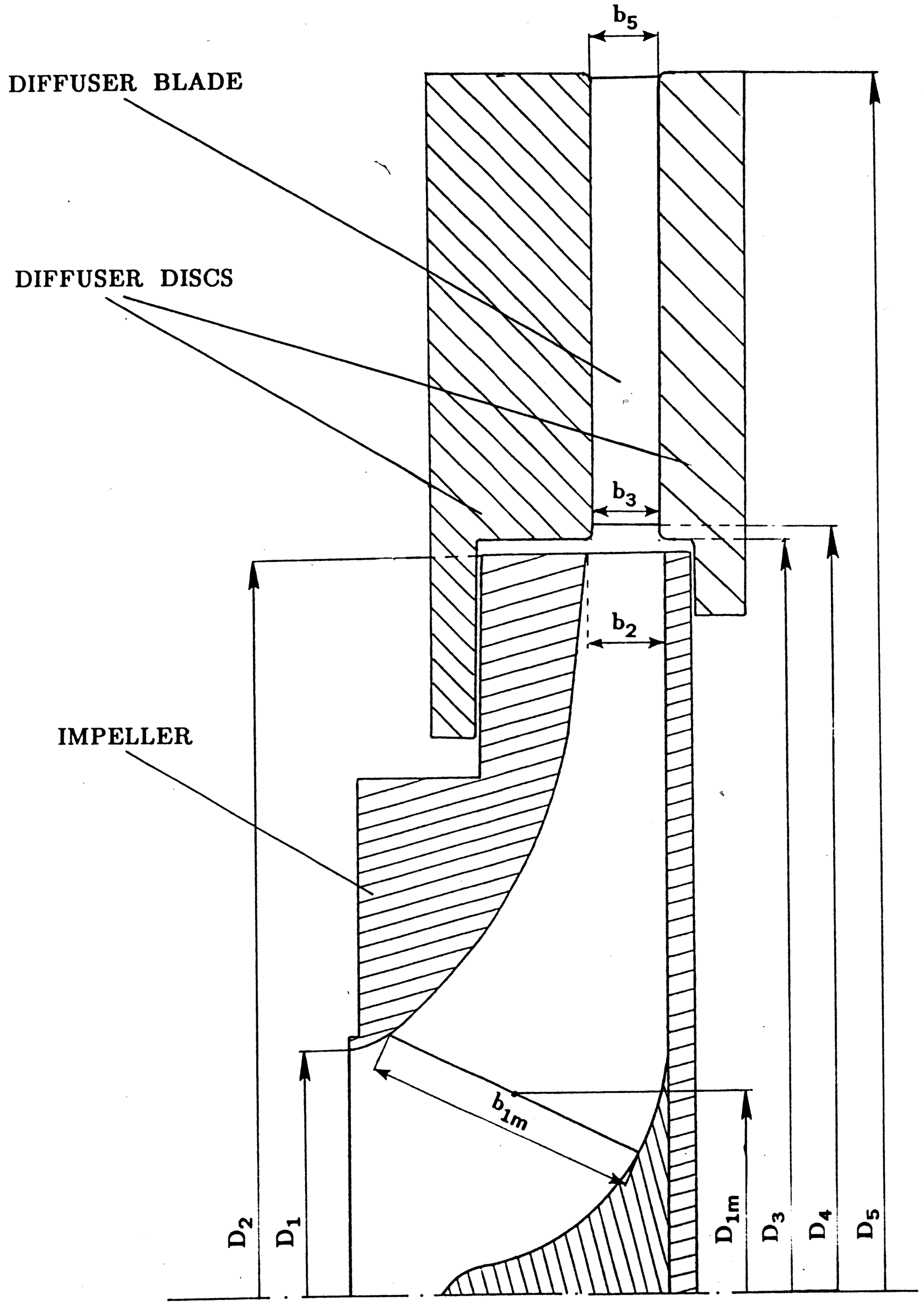

Figure 2.4: Six blade impeller with diffuser discs and diffuser blade.

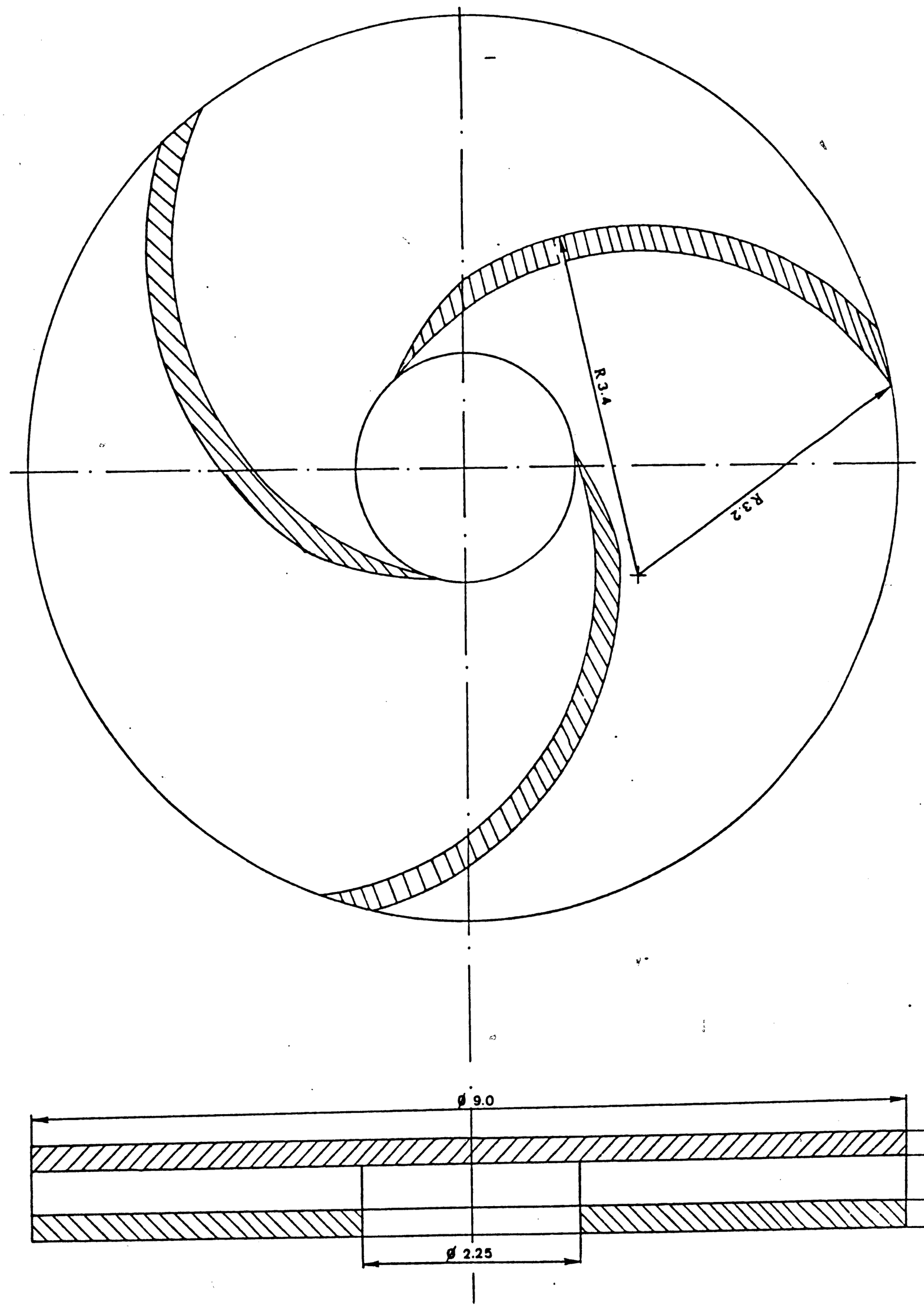

Figure 3.1: **Dimensions of the three blade impeller.**

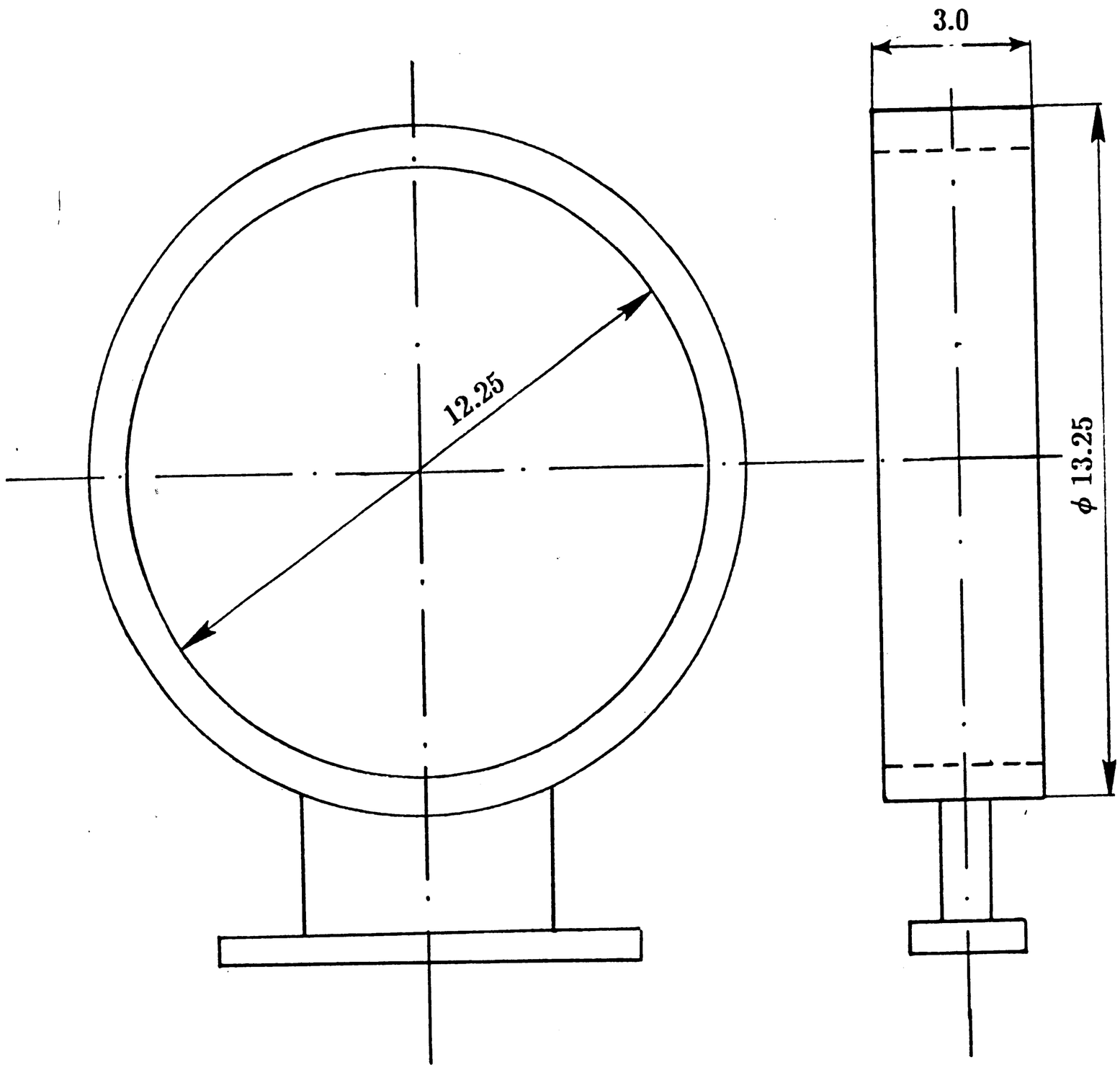

Figure 3.2: Simulated volute, designed for pressure measurements at the discharge of the impeller.

PCB PIEZOTRONICS

SPECIFICATIONS
VOLTAGE OUTPUT
PRESSURE TRANSDUCER

REVISIONS
-D- REV ECR# 2159 EOR 9/23/87

SHEET 1 OF 1

MODEL NO		106850
RANGE ±2.5V OUTPUT	±psi (db)	5 (182)
USEFUL OVERRANGE	psi	5
MAX PRESS (STEP)	psi	200
MAX PRESS (STATIC)	psi	500
RESOLUTION	psi (db)	.00007 RMS (86)
SENSITIVITY	mV/psi	500
RESONANT FREQUENCY	kHz	40
RISE TIME	µSec	8
DISCHARGE TIME CONST ⚠2	Sec	≥1
LOW FREQ RESPONSE	Hz -5%	.5
LINEARITY ⚠1	% FS	1
POLARITY		POSITIVE
OUTPUT IMPEDANCE	ohm	<100
OUTPUT BIAS	+volt	3 to 8
OVERLOAD RECOVERY	µSec	10
ACCELERATION SENS	psi/G	.002
TEMP COEFFICIENT	%/°F	≤.03
TEMPERATURE RANGE	°F	-65 to +250
MAXIMUM FLASH TEMP	°F	3000
VIBRATION/SHOCK	G's peak	500/1000
SEALING	welded	HERMETIC
CASE/DIAPHRAGM MAT'L	st. stl.	17-4/316L
WEIGHT	gm	32
CONNECTOR (micro)	coaxial	10-32
EXCITATION	+VDC/mA	18-28/2-20

⚠2 AT ROOM TEMPERATURE

⚠1 ZERO BASED BEST STRAIGHT LINE.

SUPPLIED ACCESSORIES:
SEAL MOD. 065A36
CLAMP NUT MOD. C30A11

APP'D	TPW	11/86	SPEC No. 105-2500-80
ENGR	[illegible]	[illegible]	
SALES	[illegible]	[illegible]	

Figure 3.3: Specifications of the PCB-106B50 pressure transducer. [Reproduced from PCB Piezotronics, Inc. Manual]

MODEL 106B50

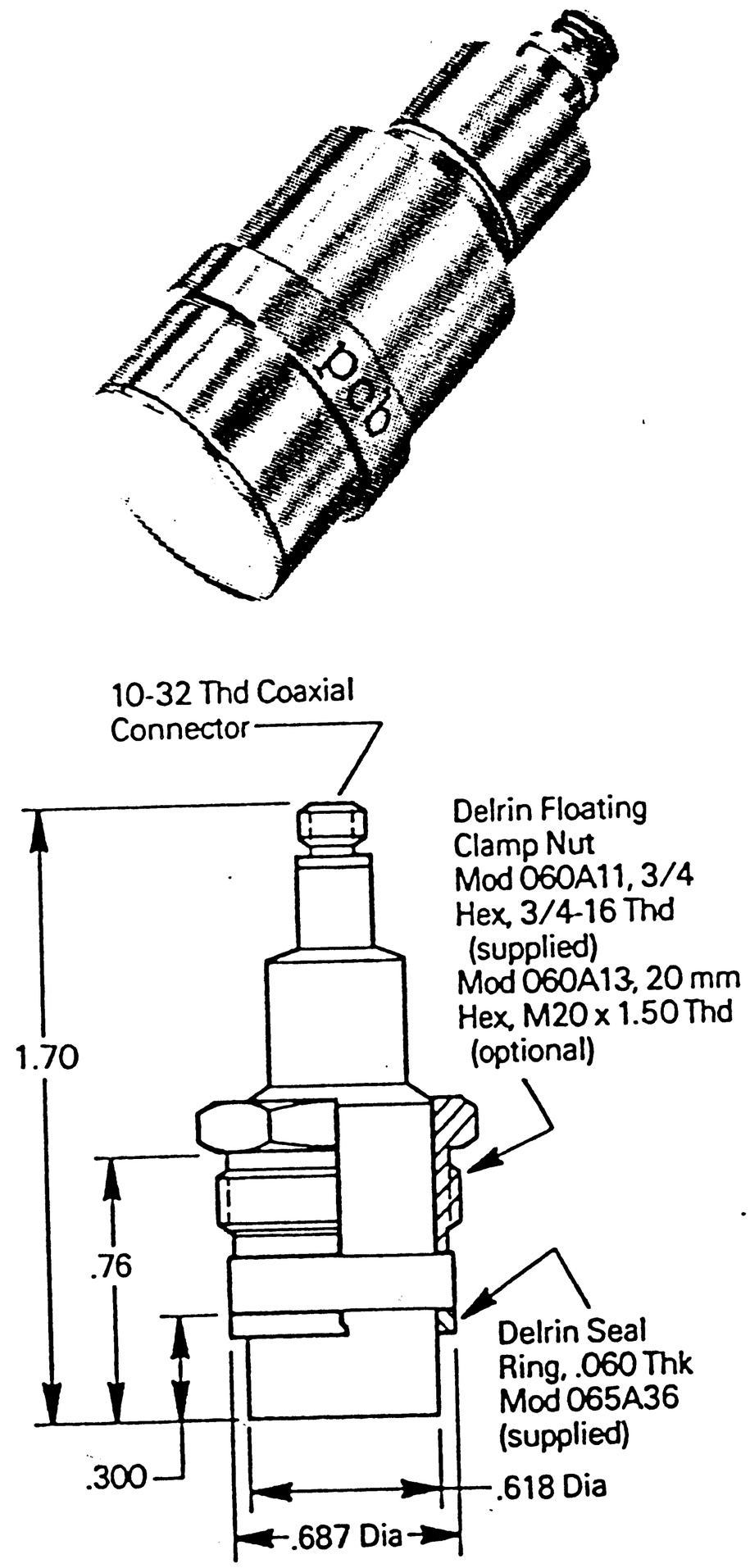

Figure 3.4: **Dimensions of the pressure transducer.**
[Reproduced from PCB Piezotronics, Inc. Manual]

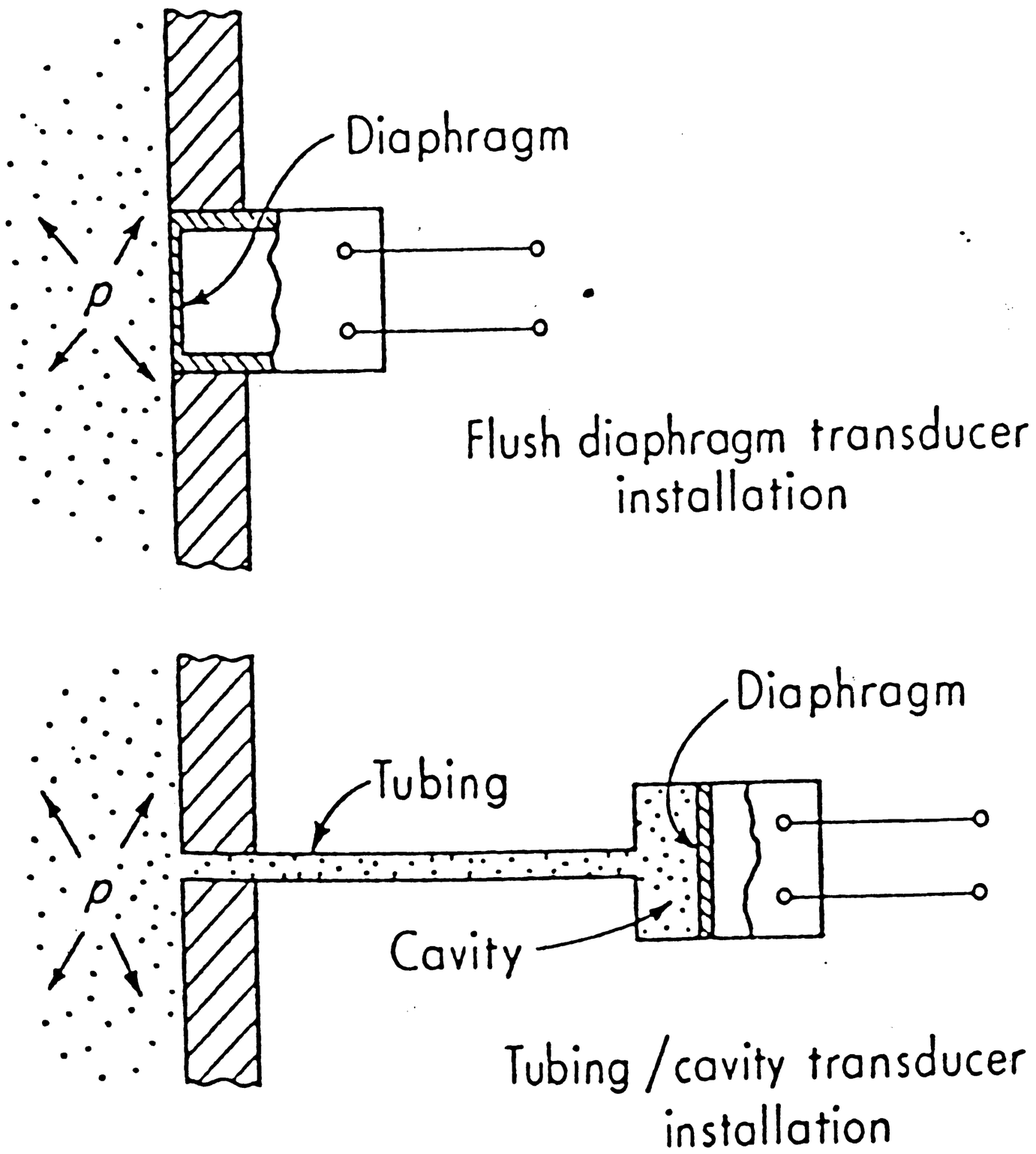

Figure 3.5: Flush diaphragm and tubing/cavity transducers.
[Reproduced from Doebelin, E. O., Measurements Systems]

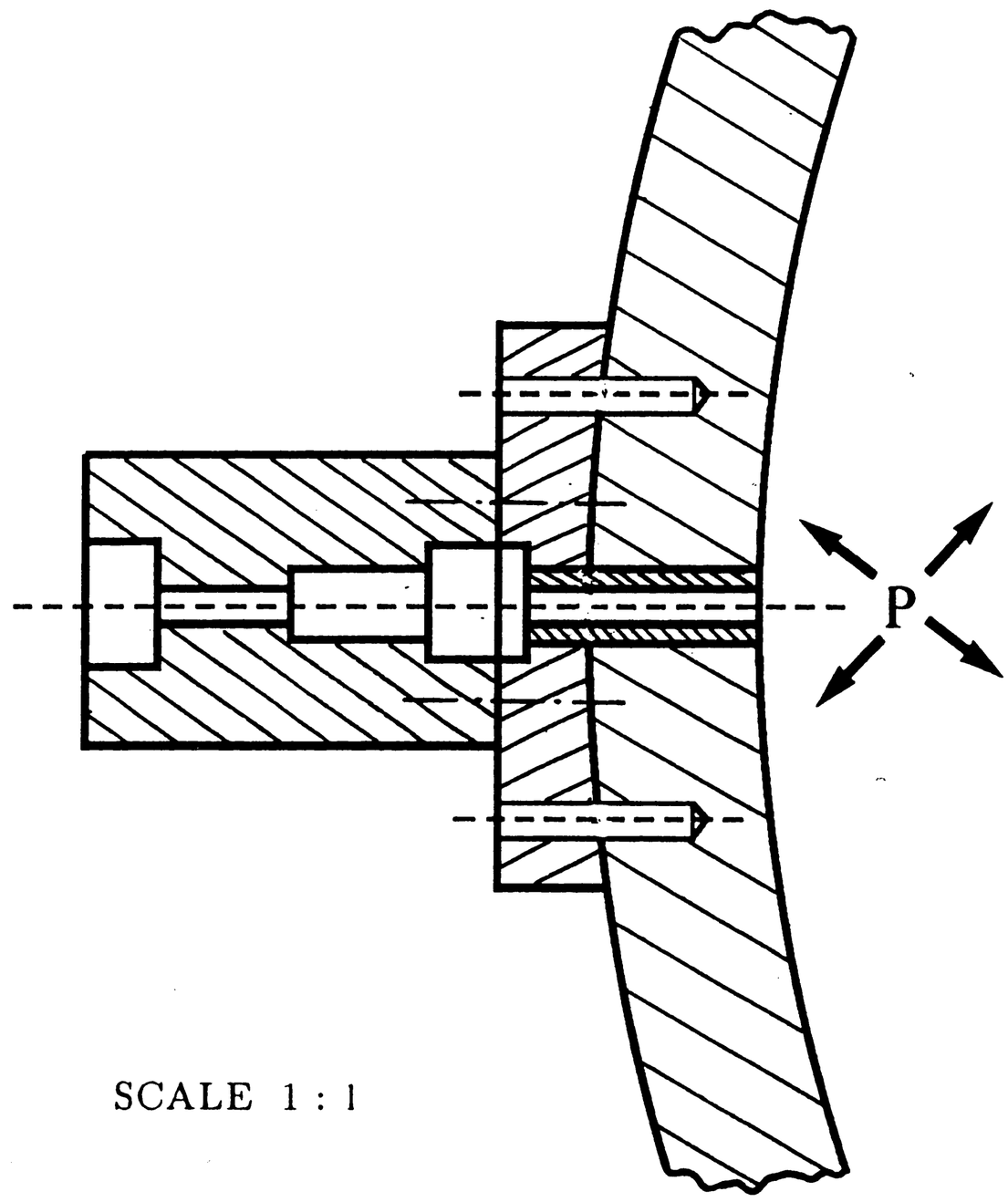

SCALE 1 : 1

Figure 3.6: **Pressure transducer mount, mounted on the volute simulation ring.**

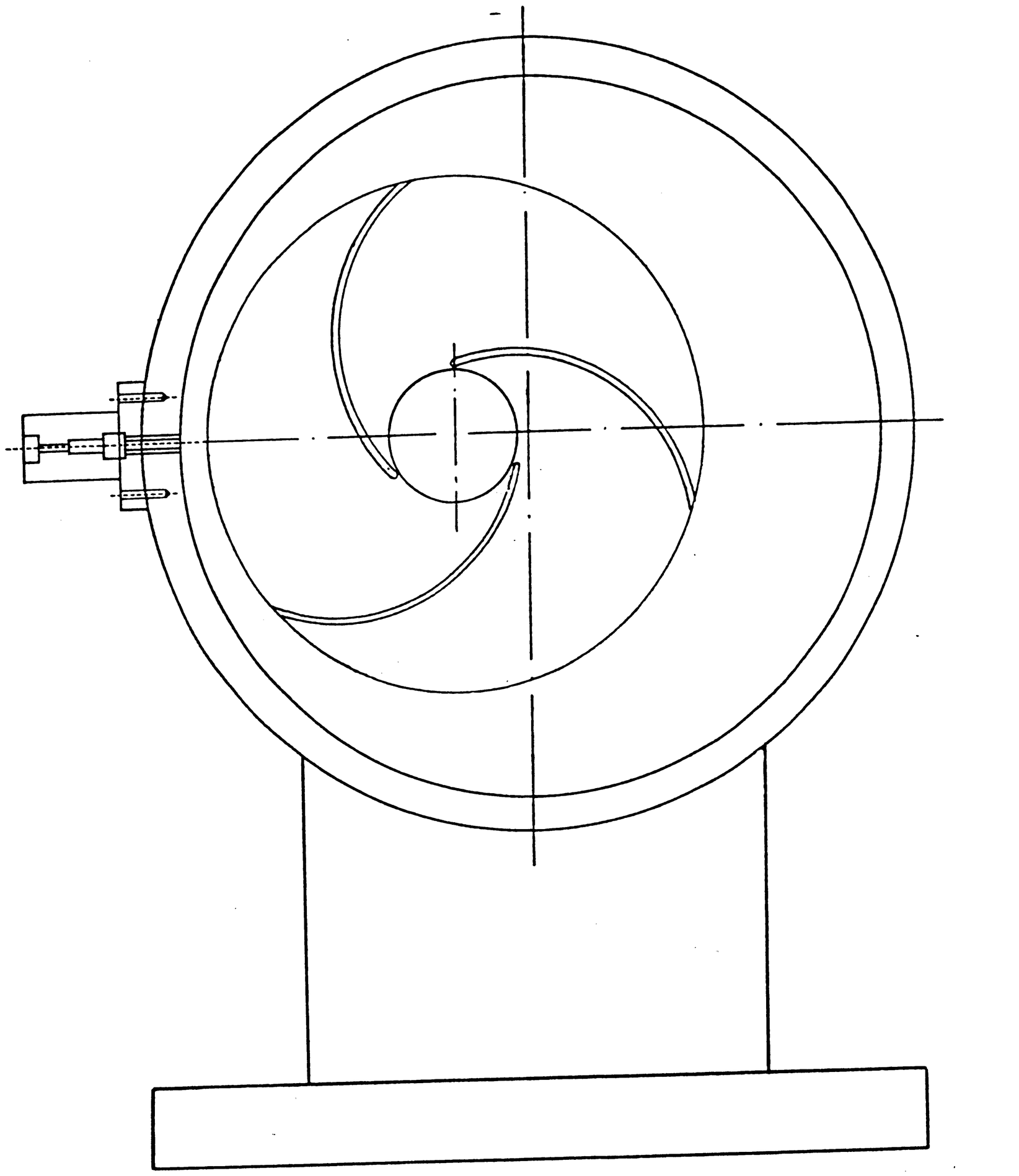

Figure 3.7: **Location of the pressure transducer relative to the impeller.**

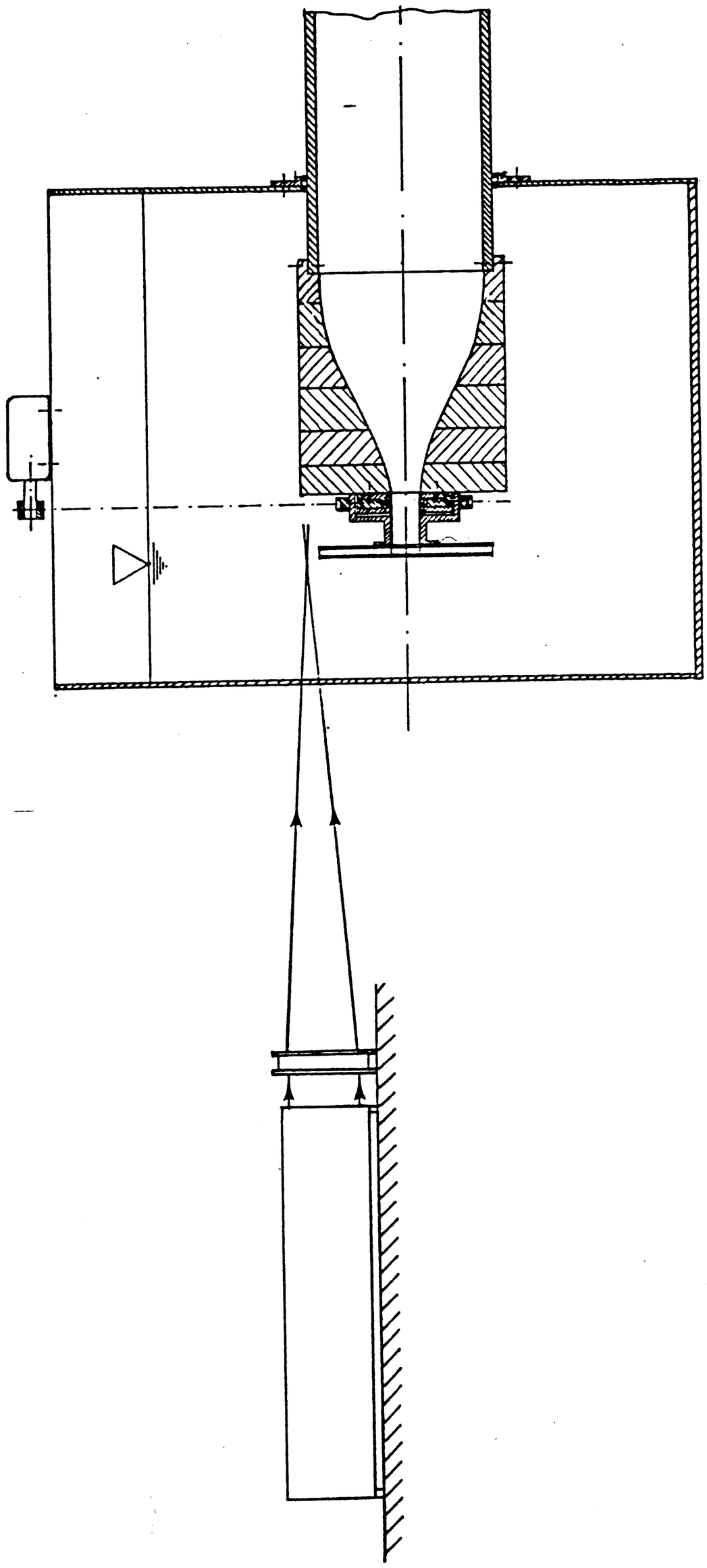

Figure 3.8: Laser Doppler Velocimetry setup.

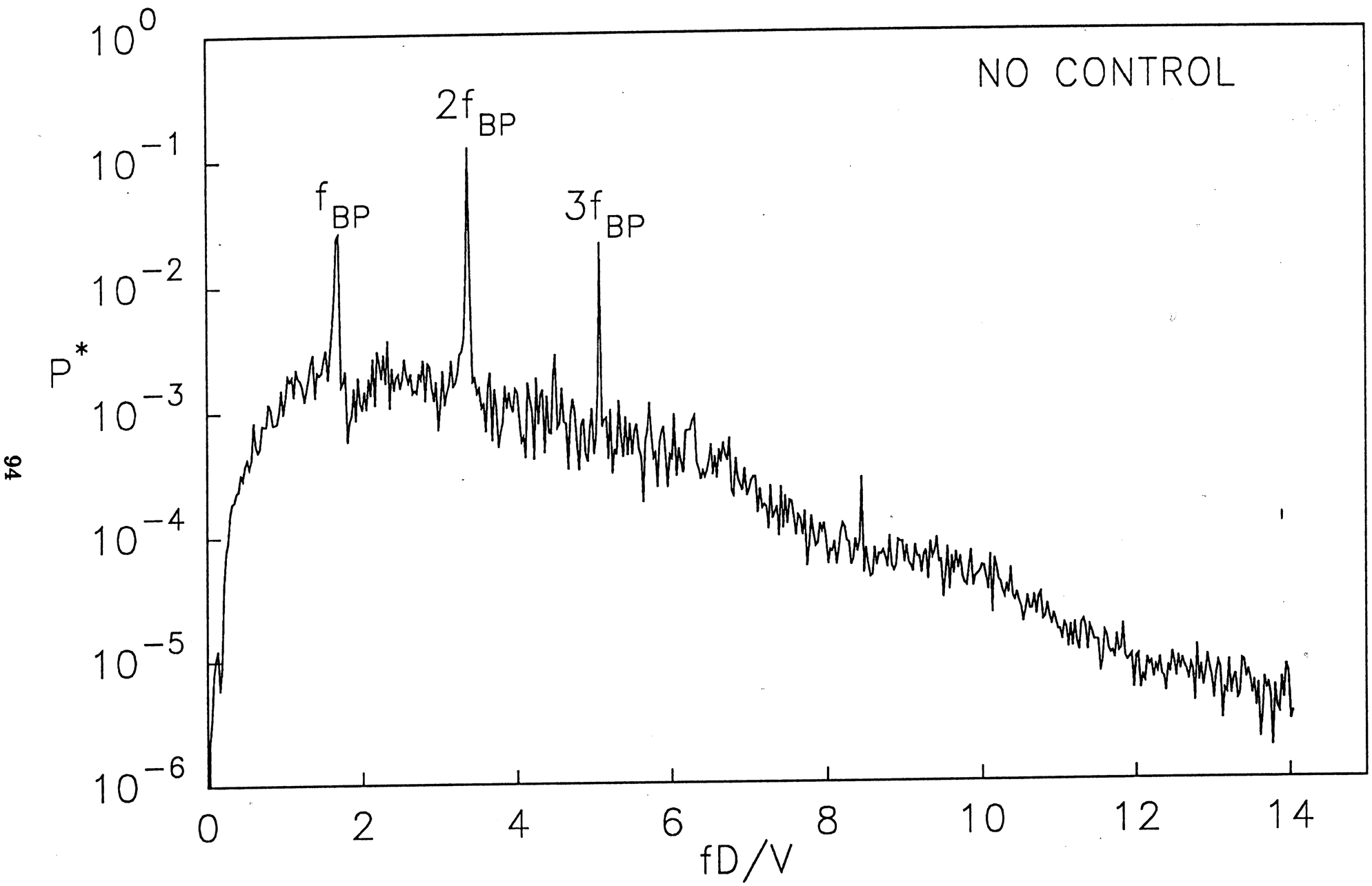

Figure 3.9.a (Plot P1)

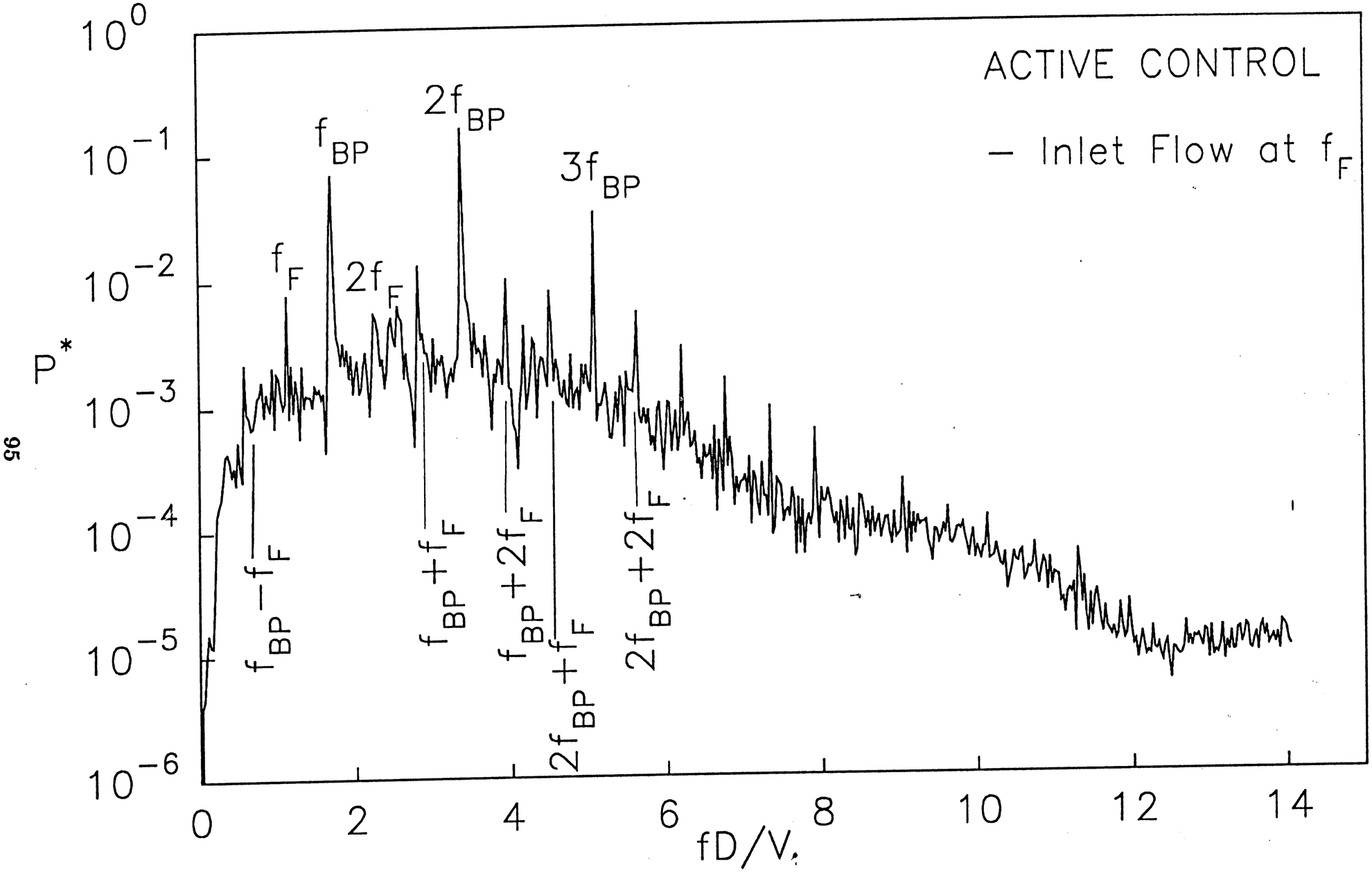

Figure 3.9.b (Plot P2)

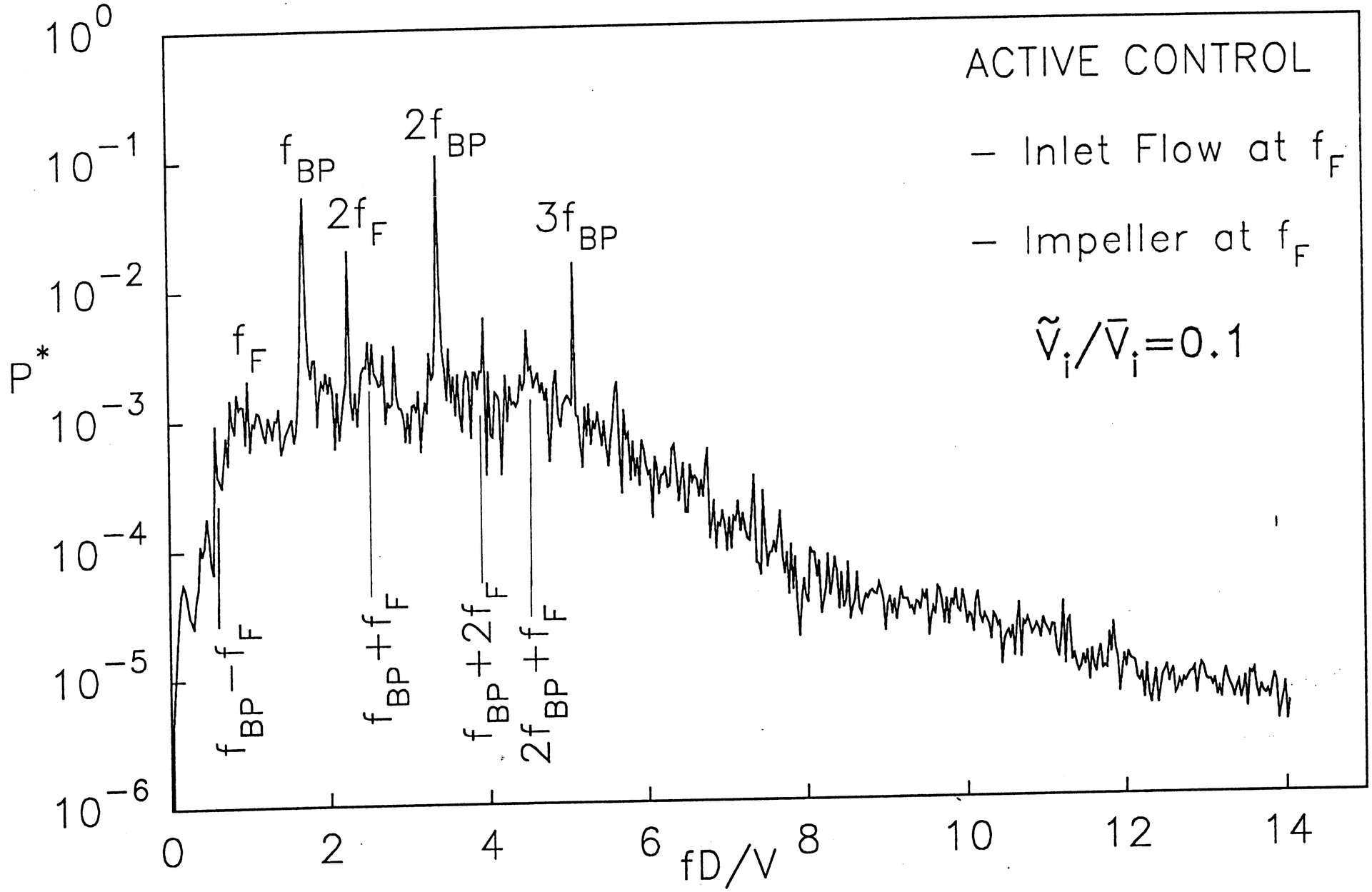

Figure 3.9.c (Plot P3)

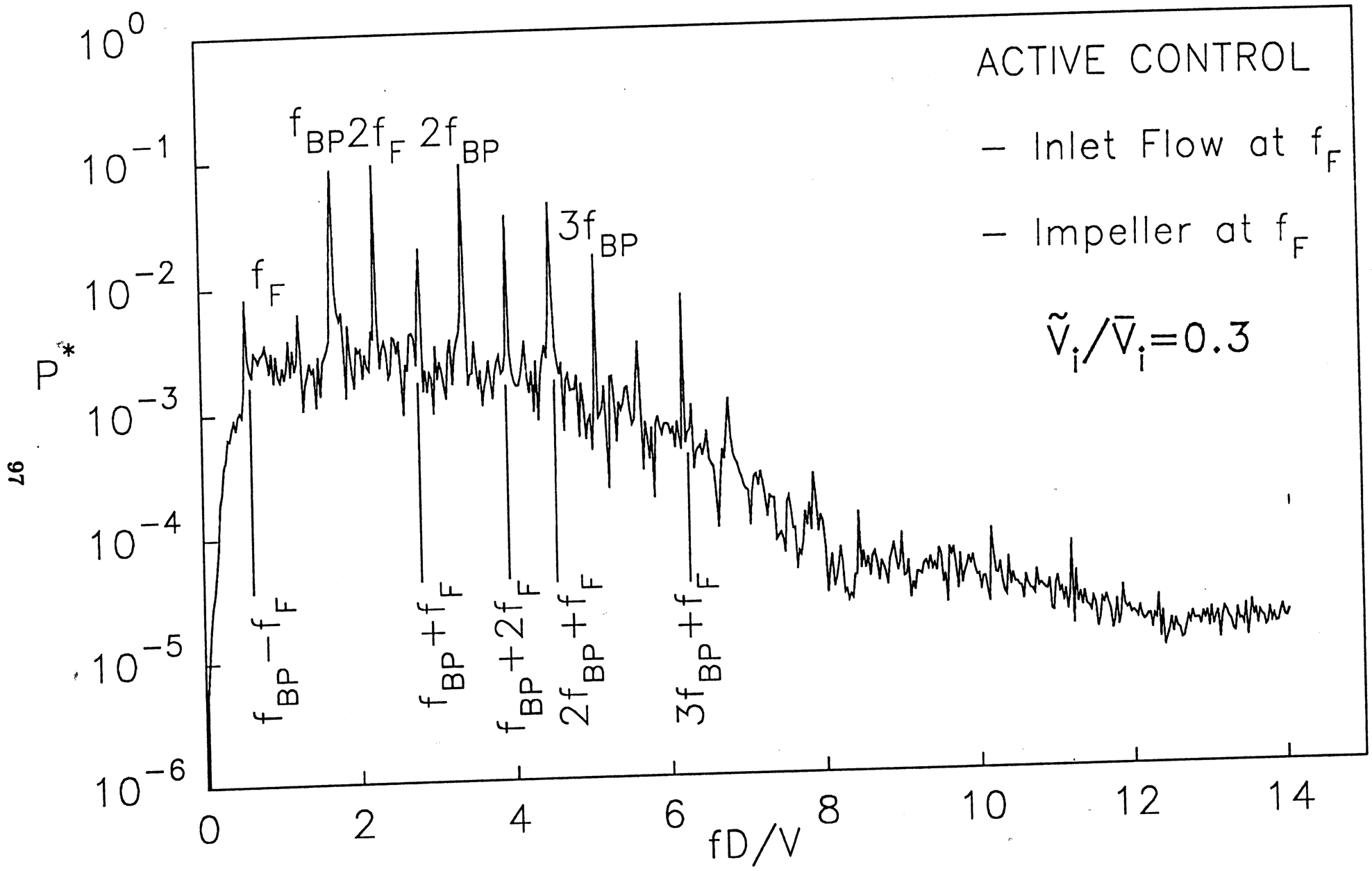

Figure 3.9.d (Plot P4)

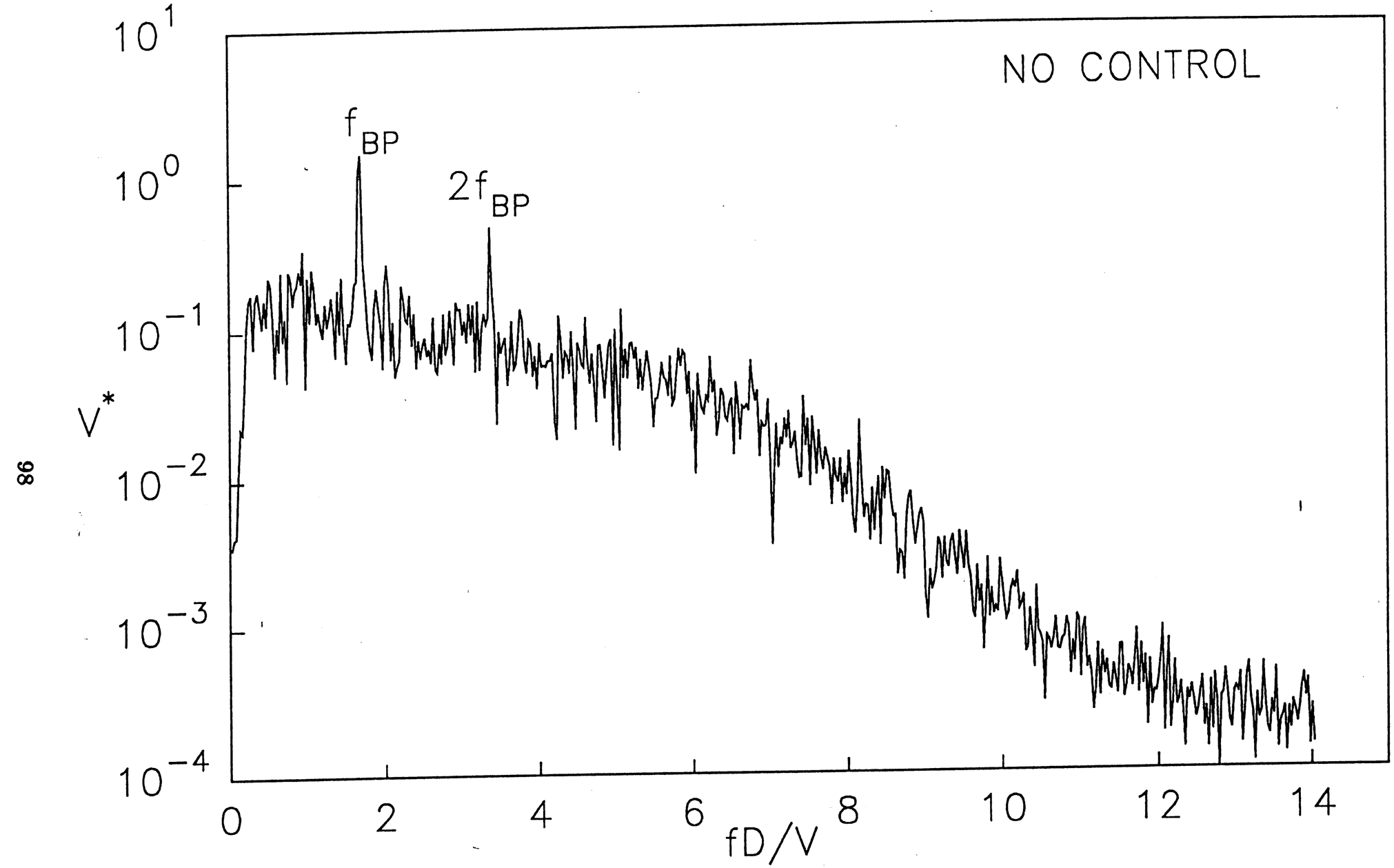

Figure 3.10.a (Plot V1)

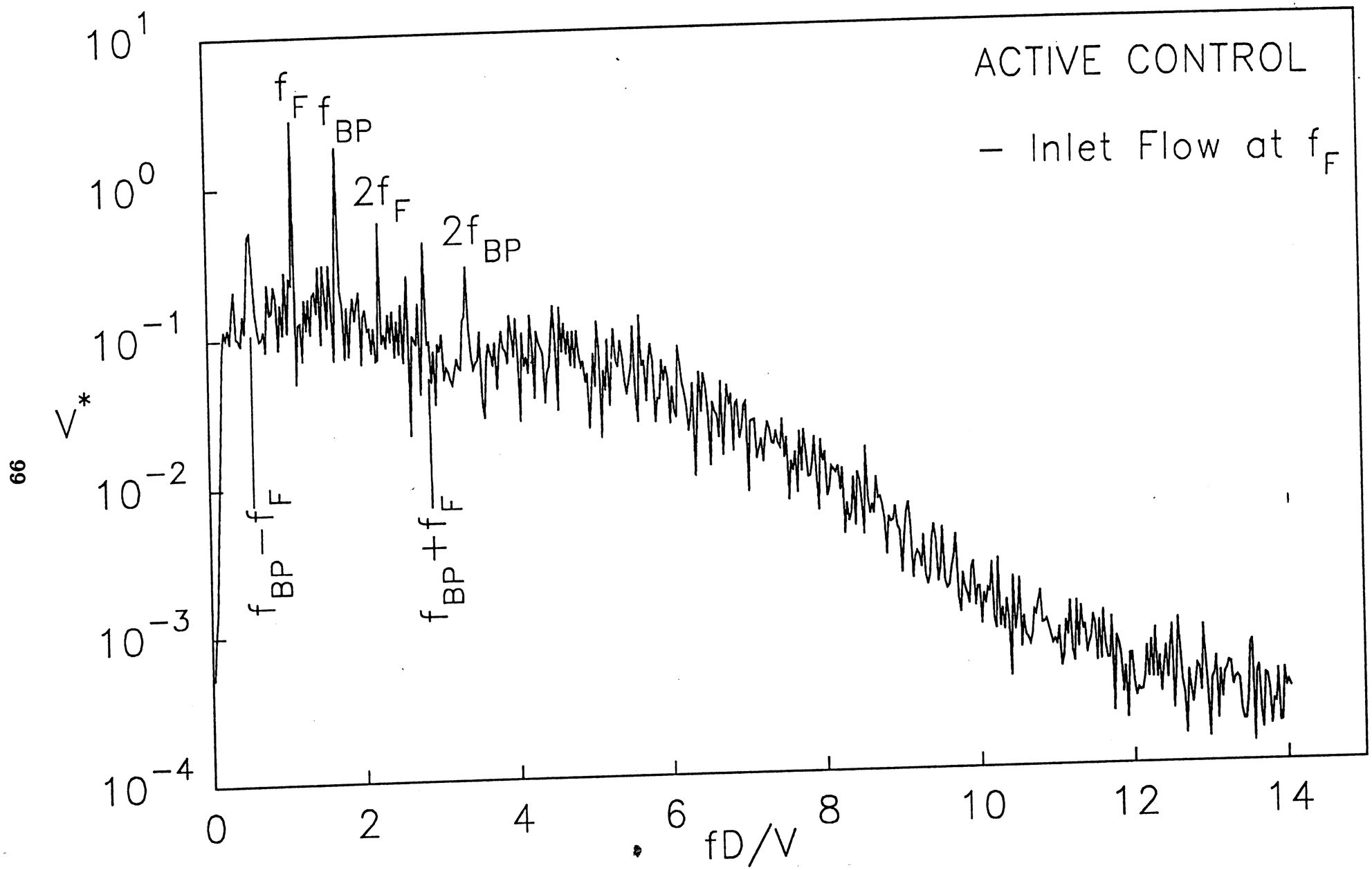

Figure 3.10.b (Plot V2)

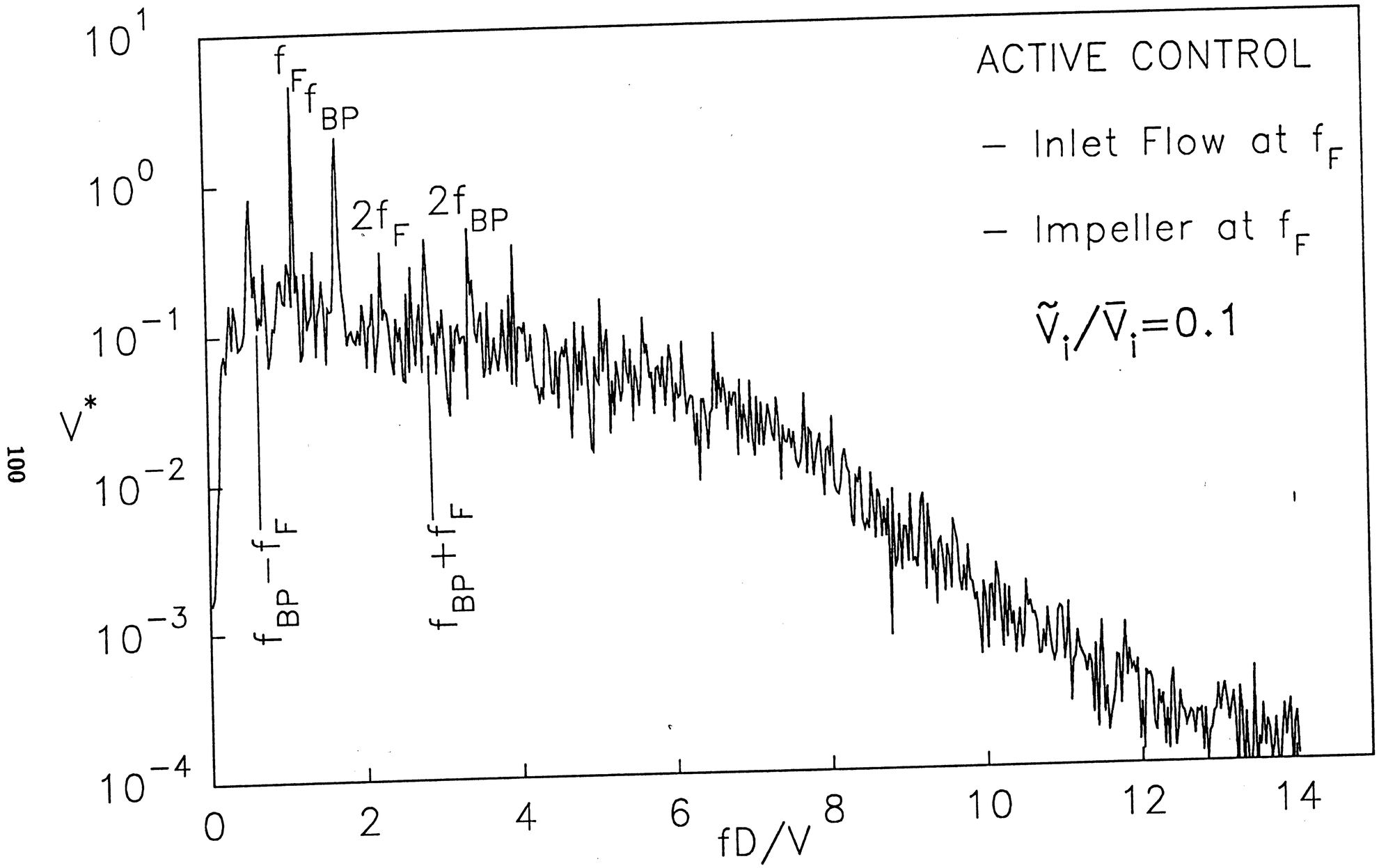

Figure 3.10.c (Plot V3)

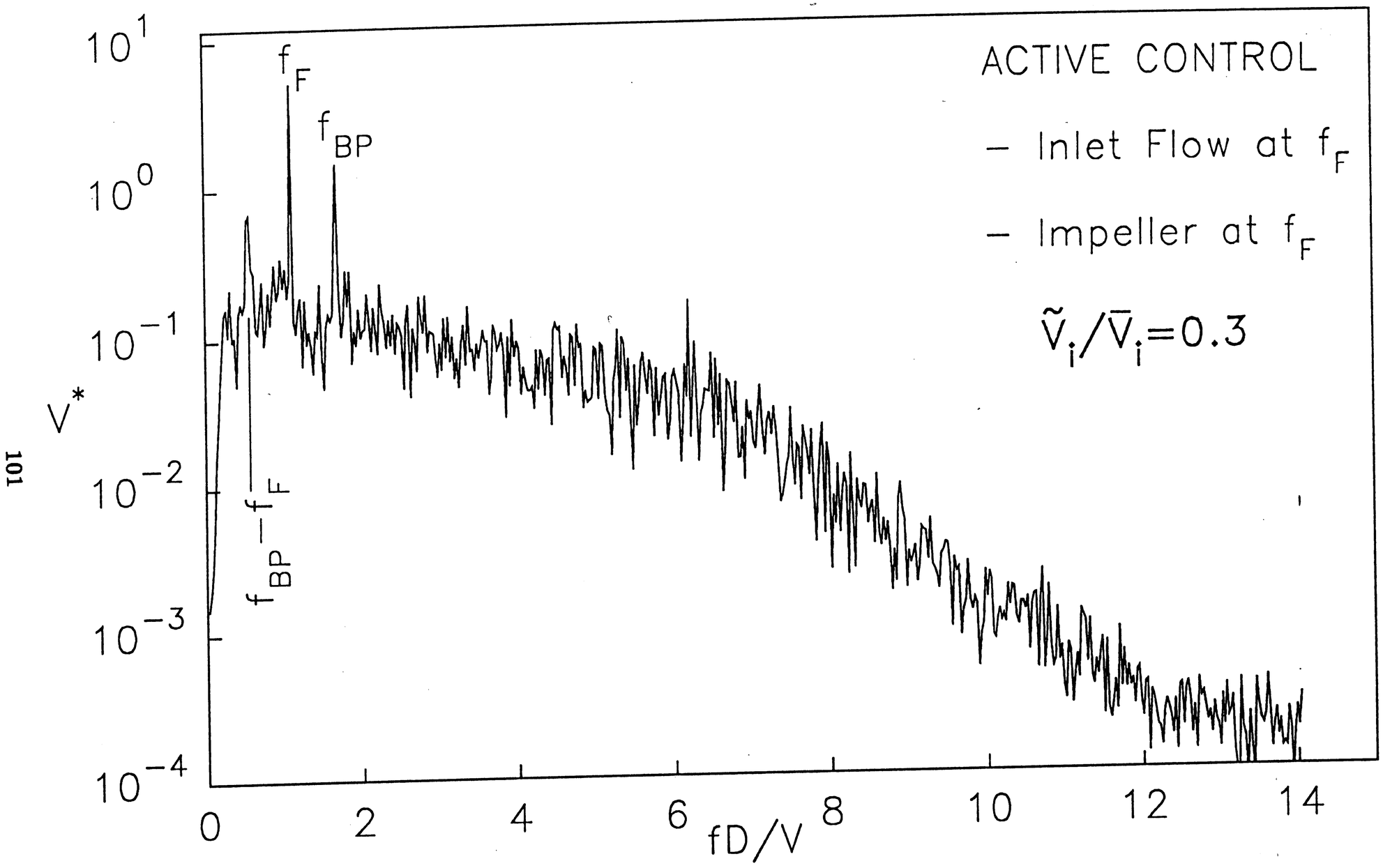

Figure 3.10.d (Plot V4)

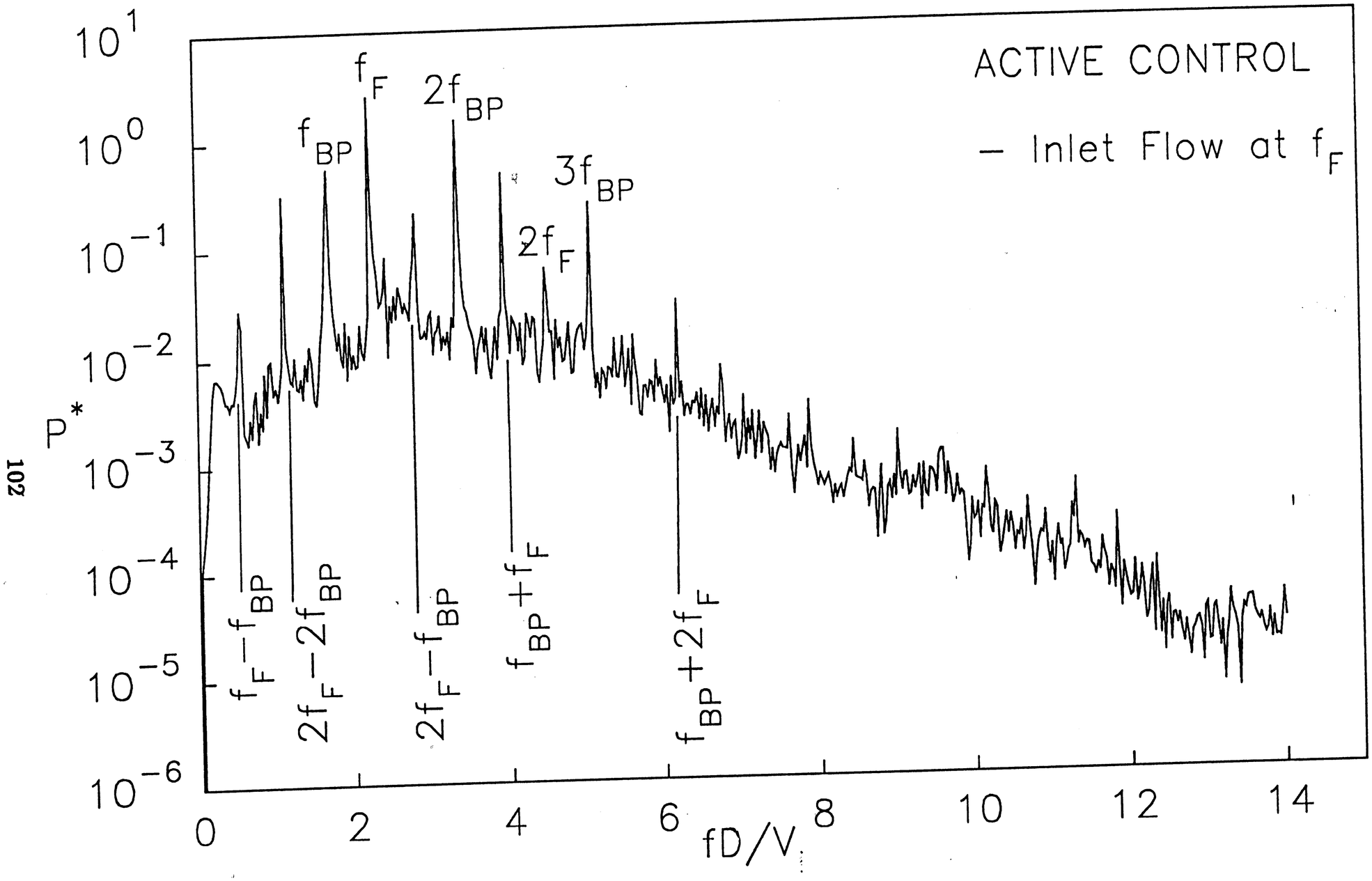

Figure 3.11.a (Plot P5)

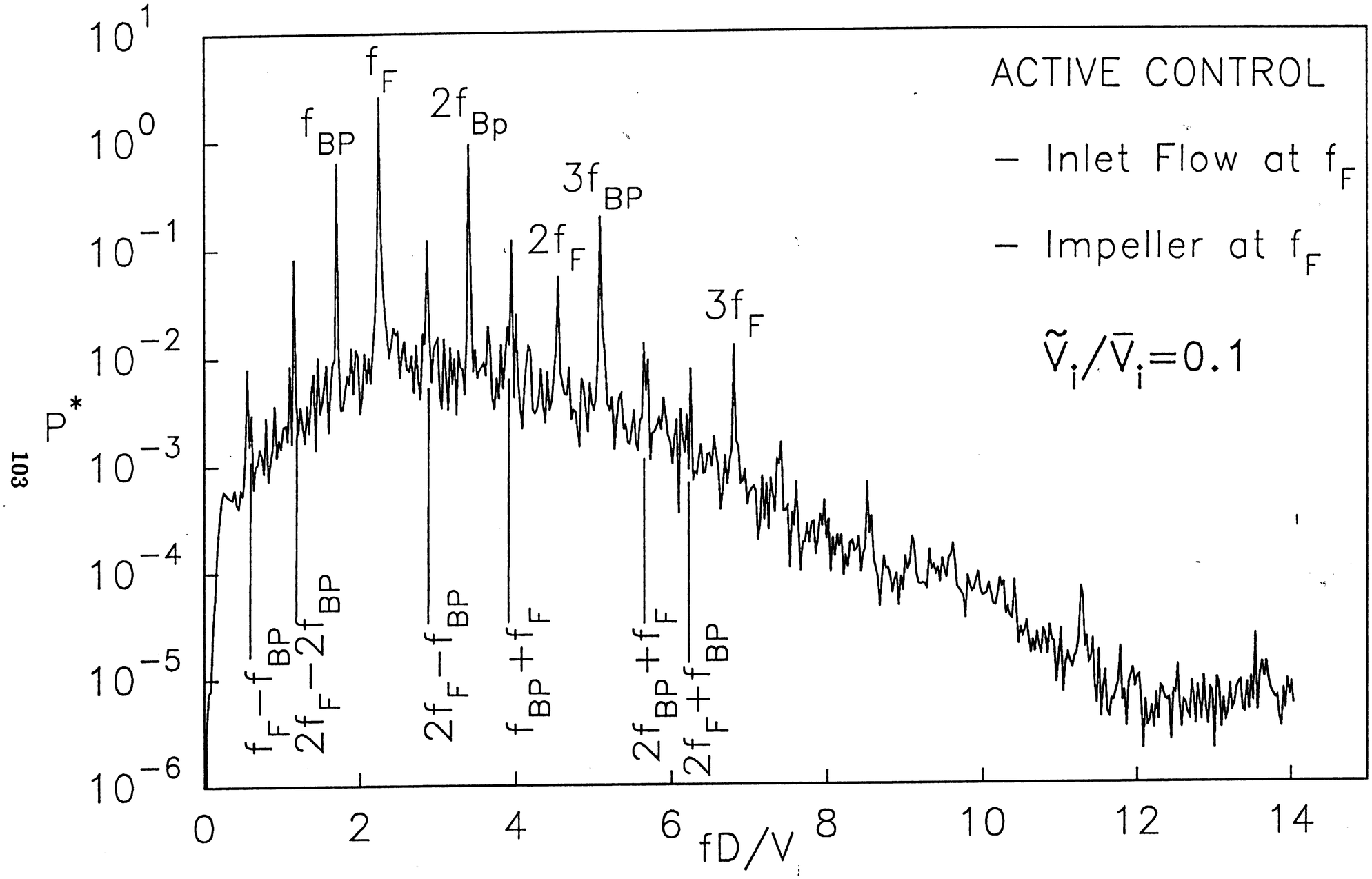

Figure 3.11.b (Plot P6)

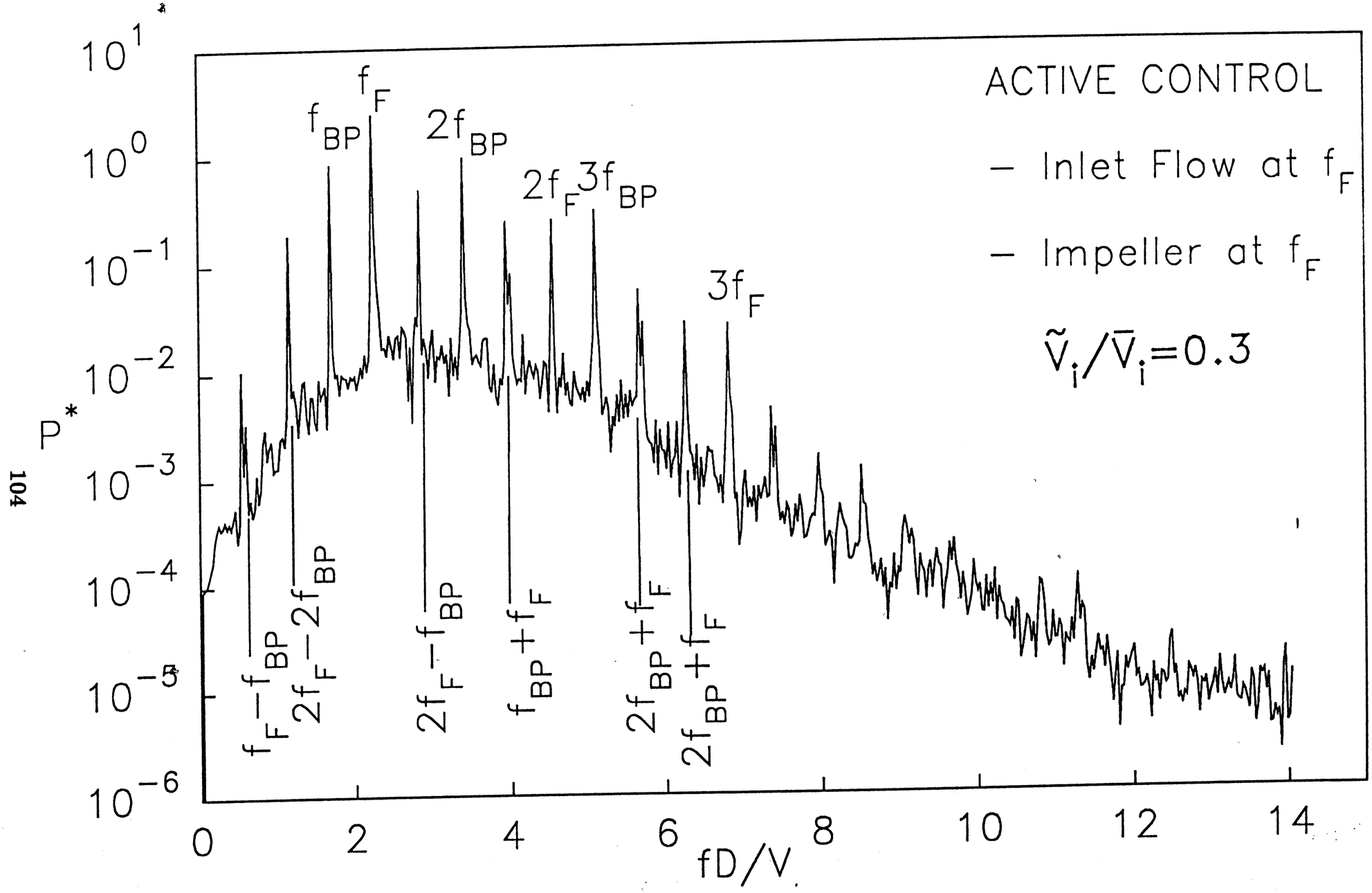

Figure 3.11.c (Plot P7)

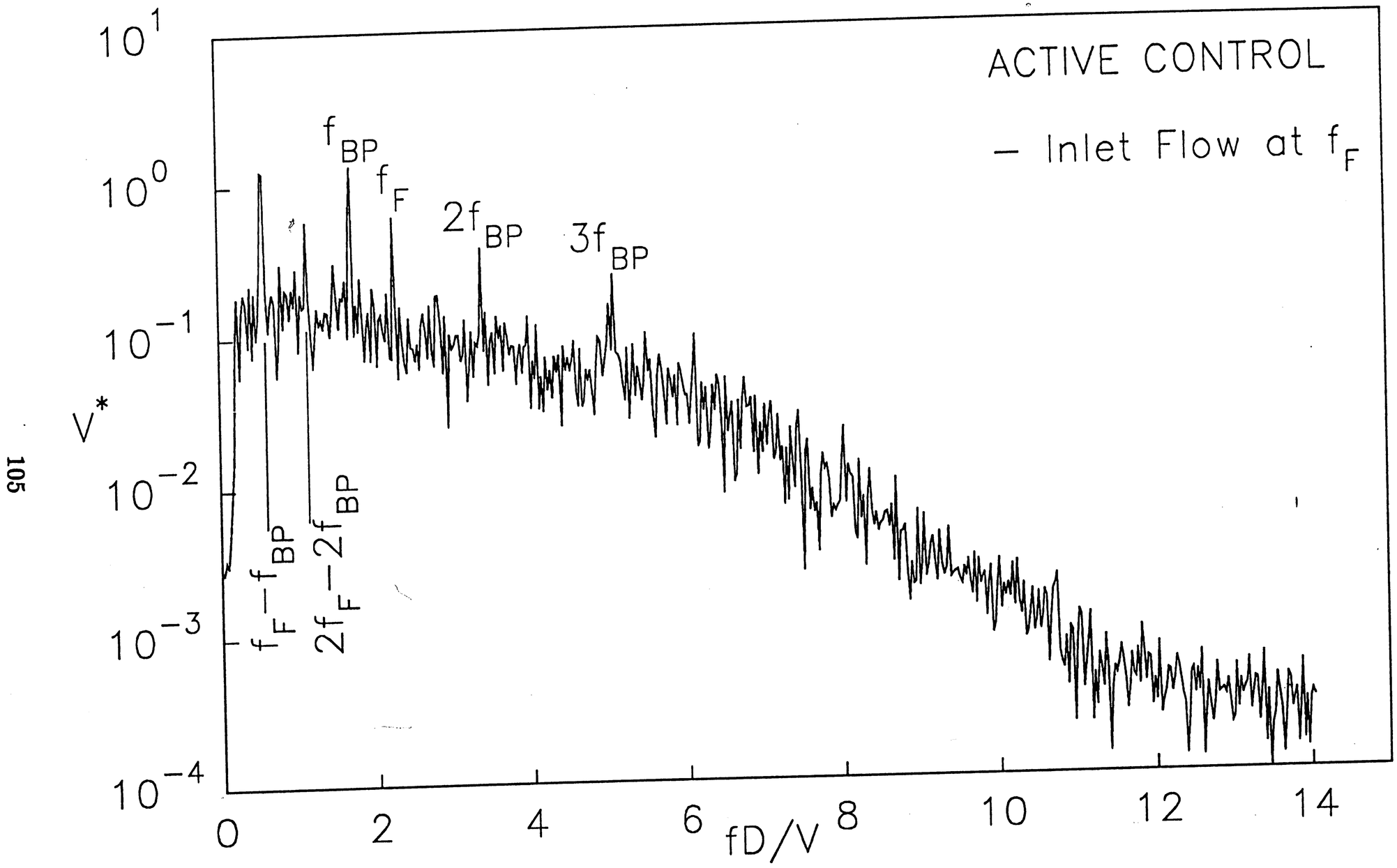

Figure 3.12.a (Plot V5)

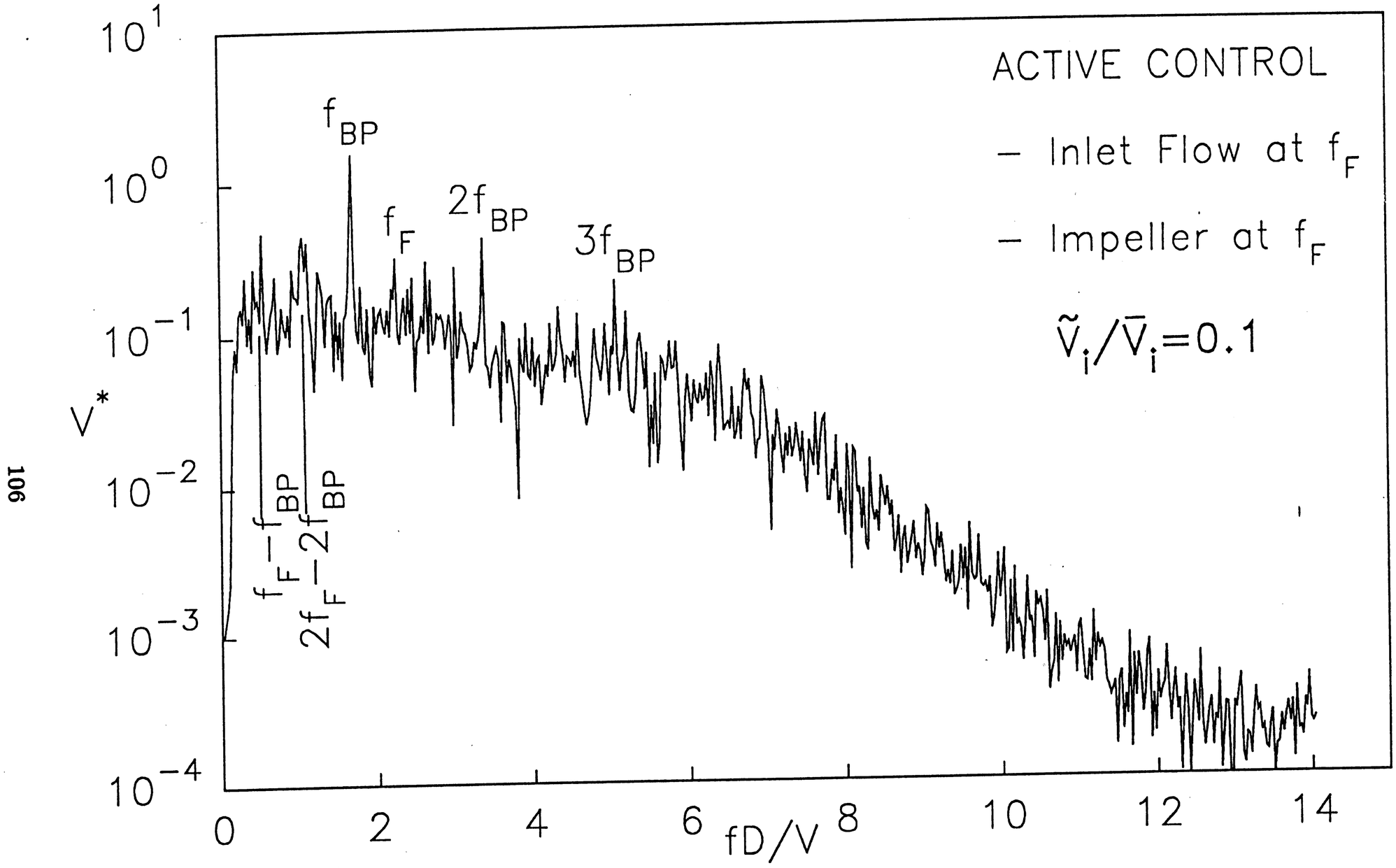

Figure 3.12.b (Plot V6)

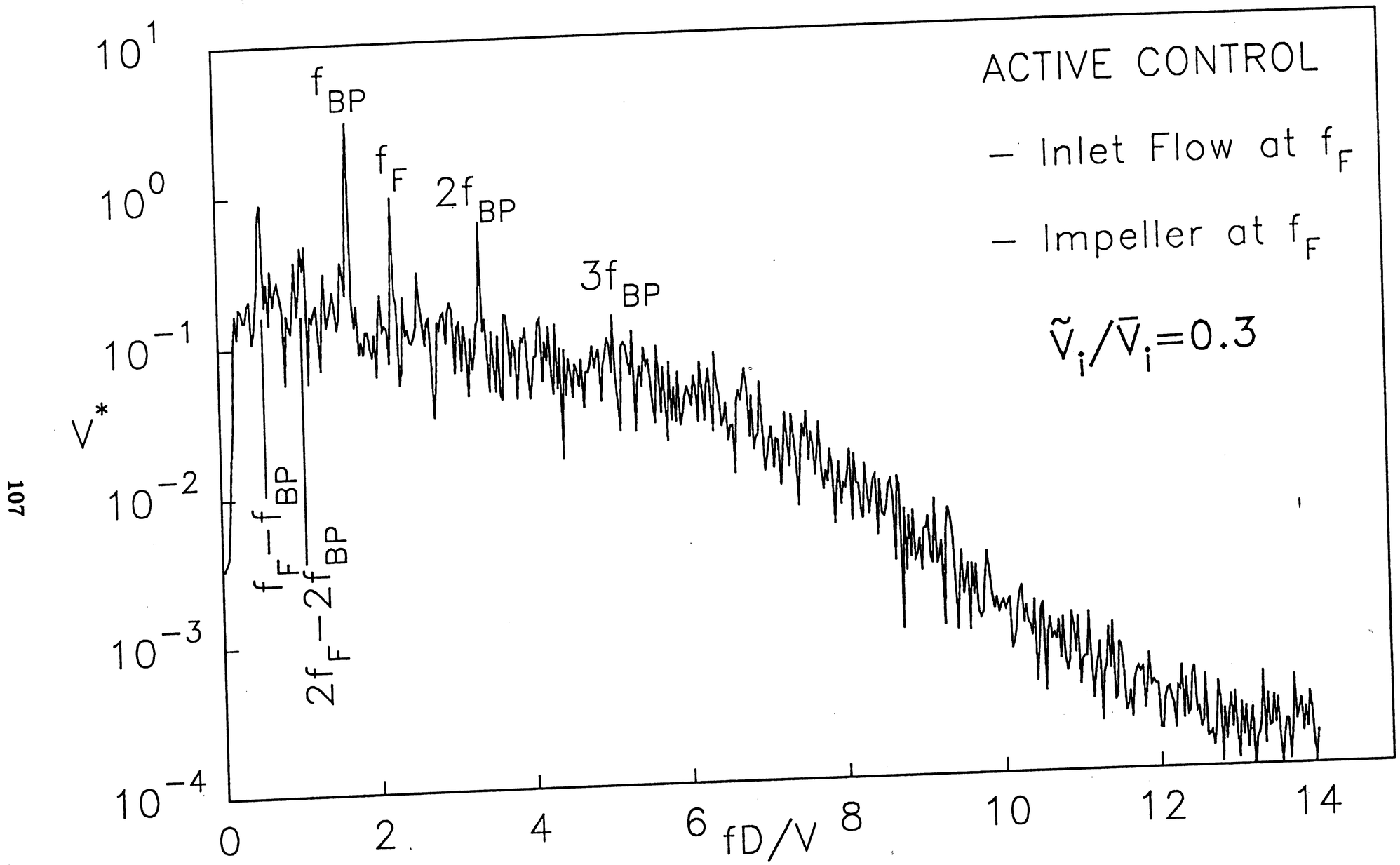

Figure 3.12.c (Plot V7)

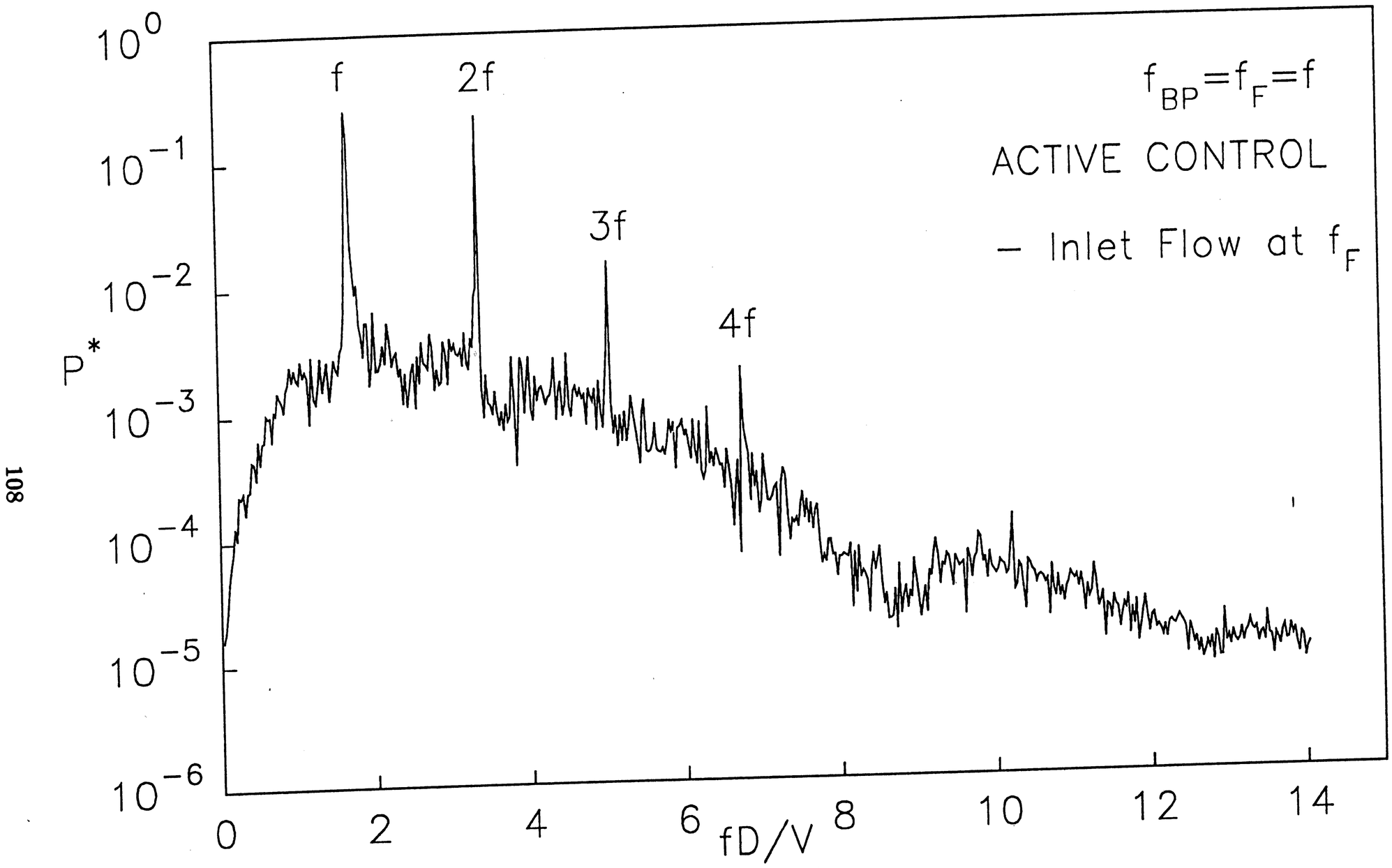

108

Figure 3.13.a (Plot P8)

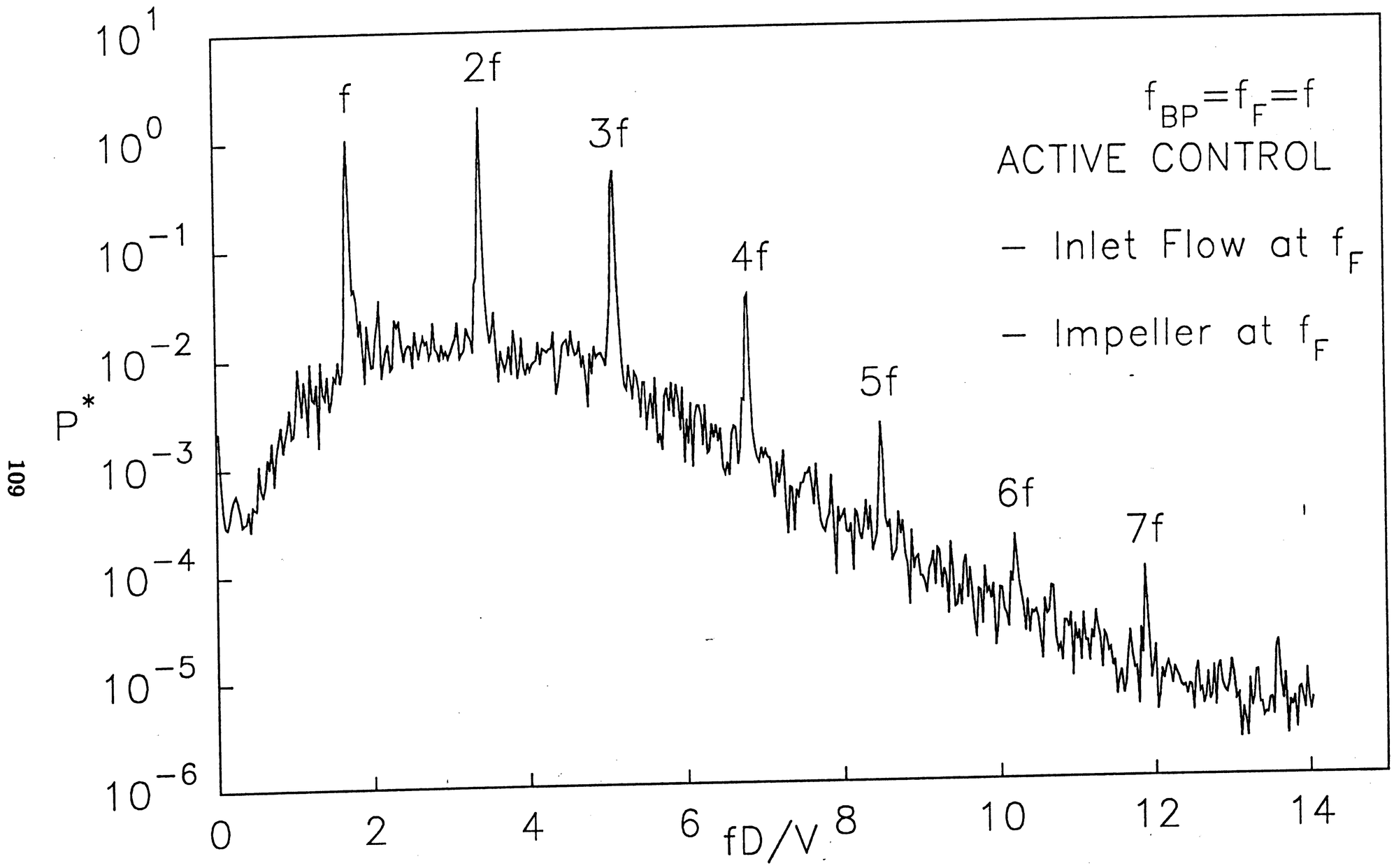

Figure 3.13.b (Plot P9)

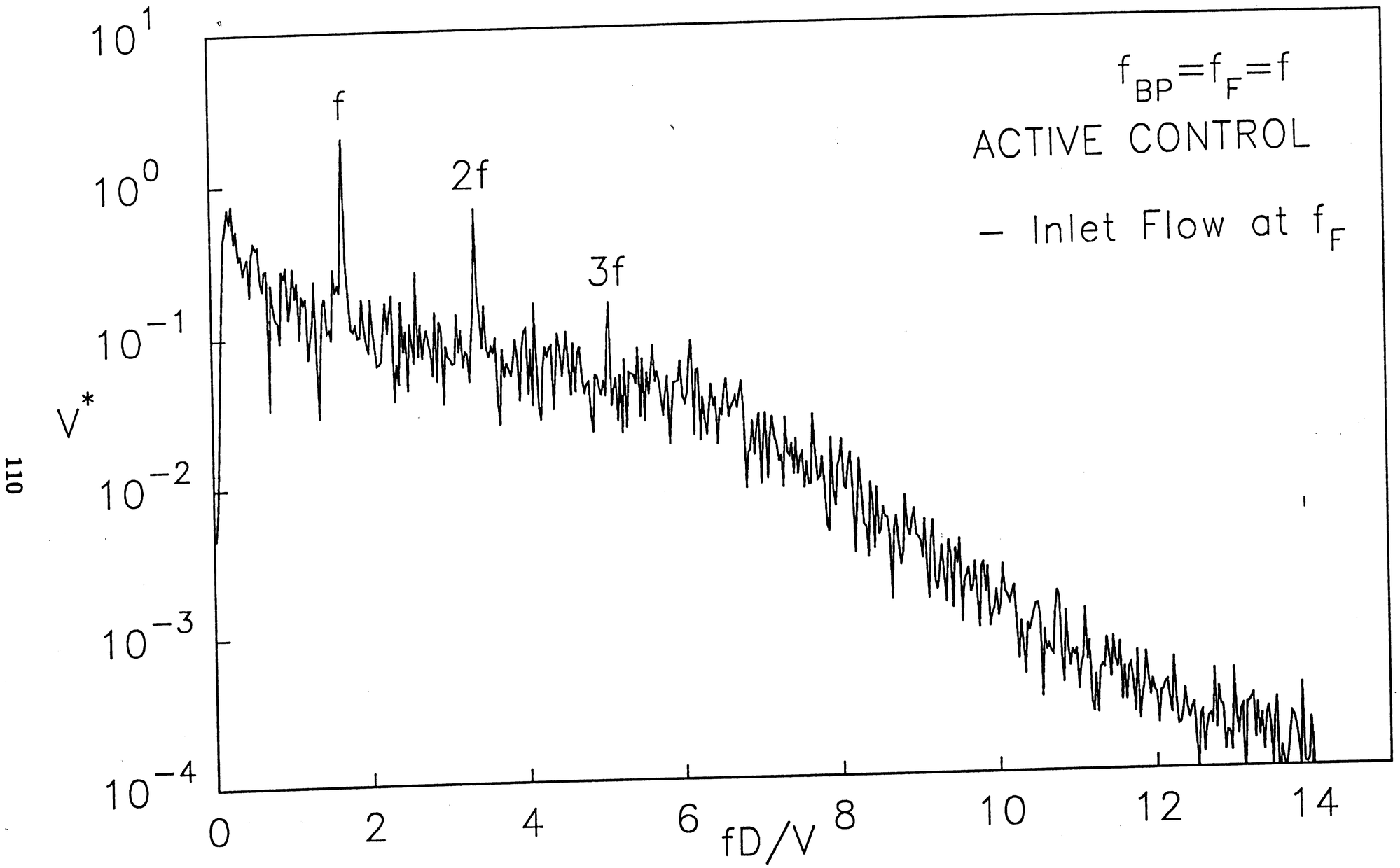

Figure 3.14.a (Plot V8)

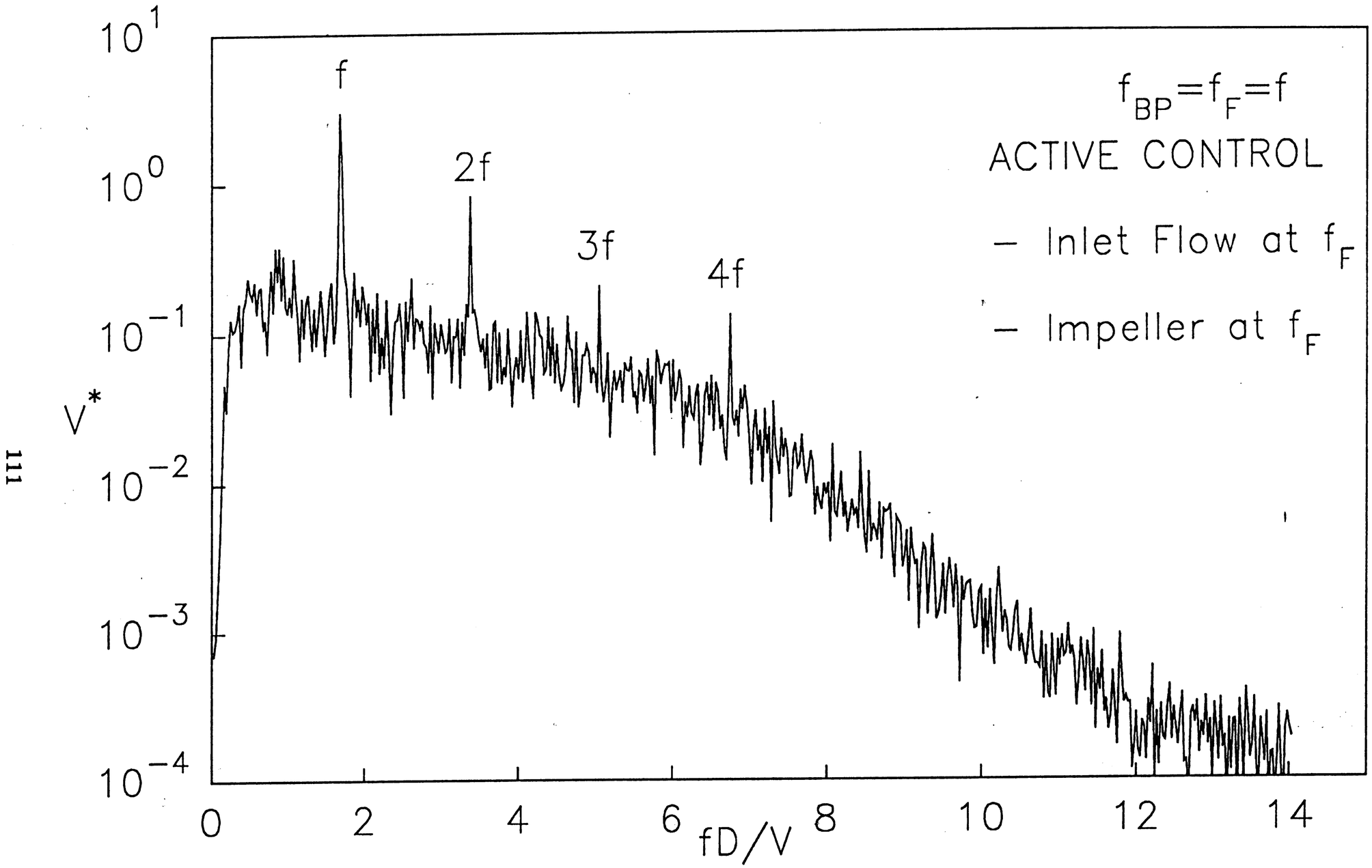

Figure 3.14.b (Plot V9)

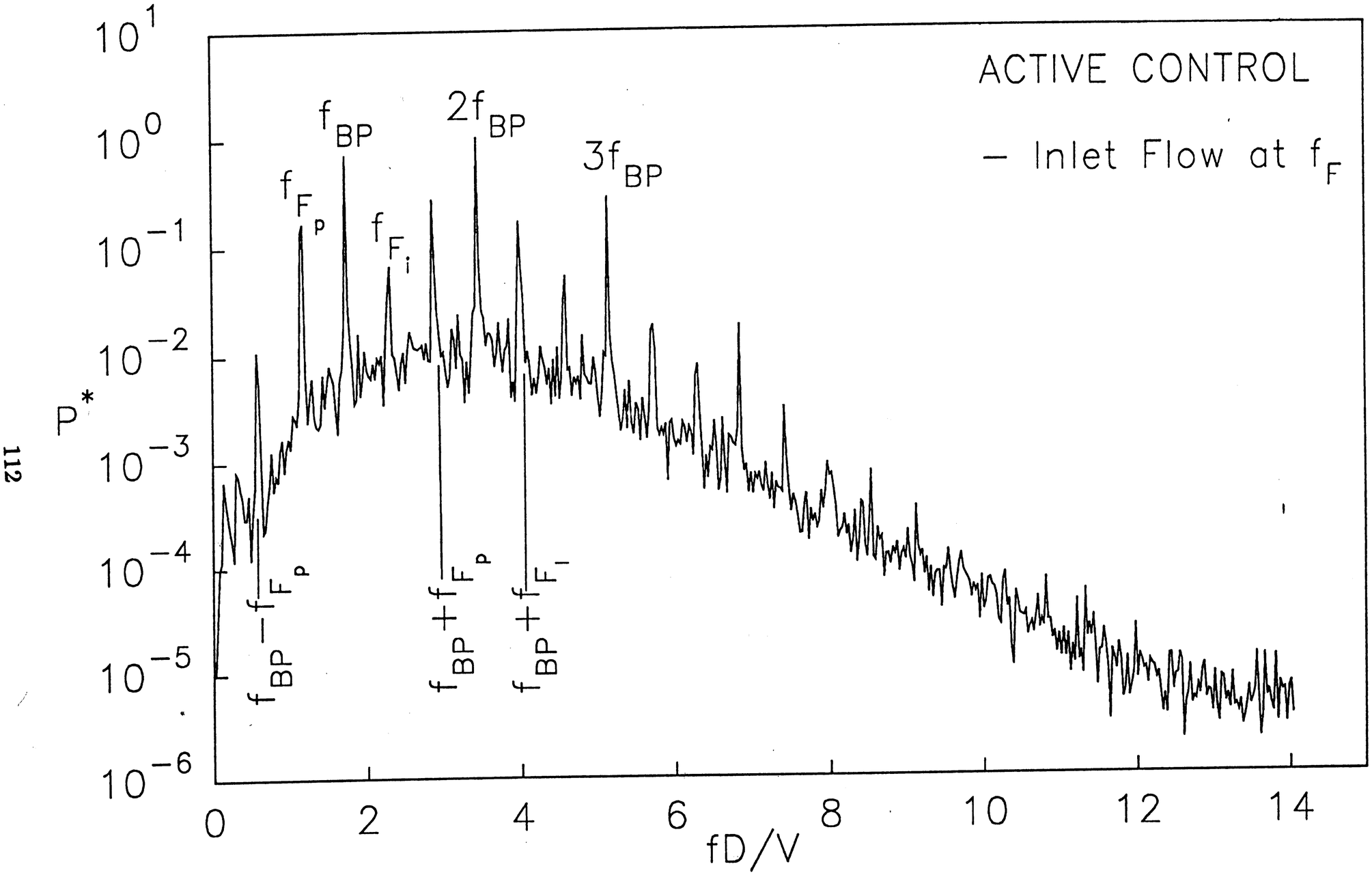

Figure 3.15.a (Plot P10)

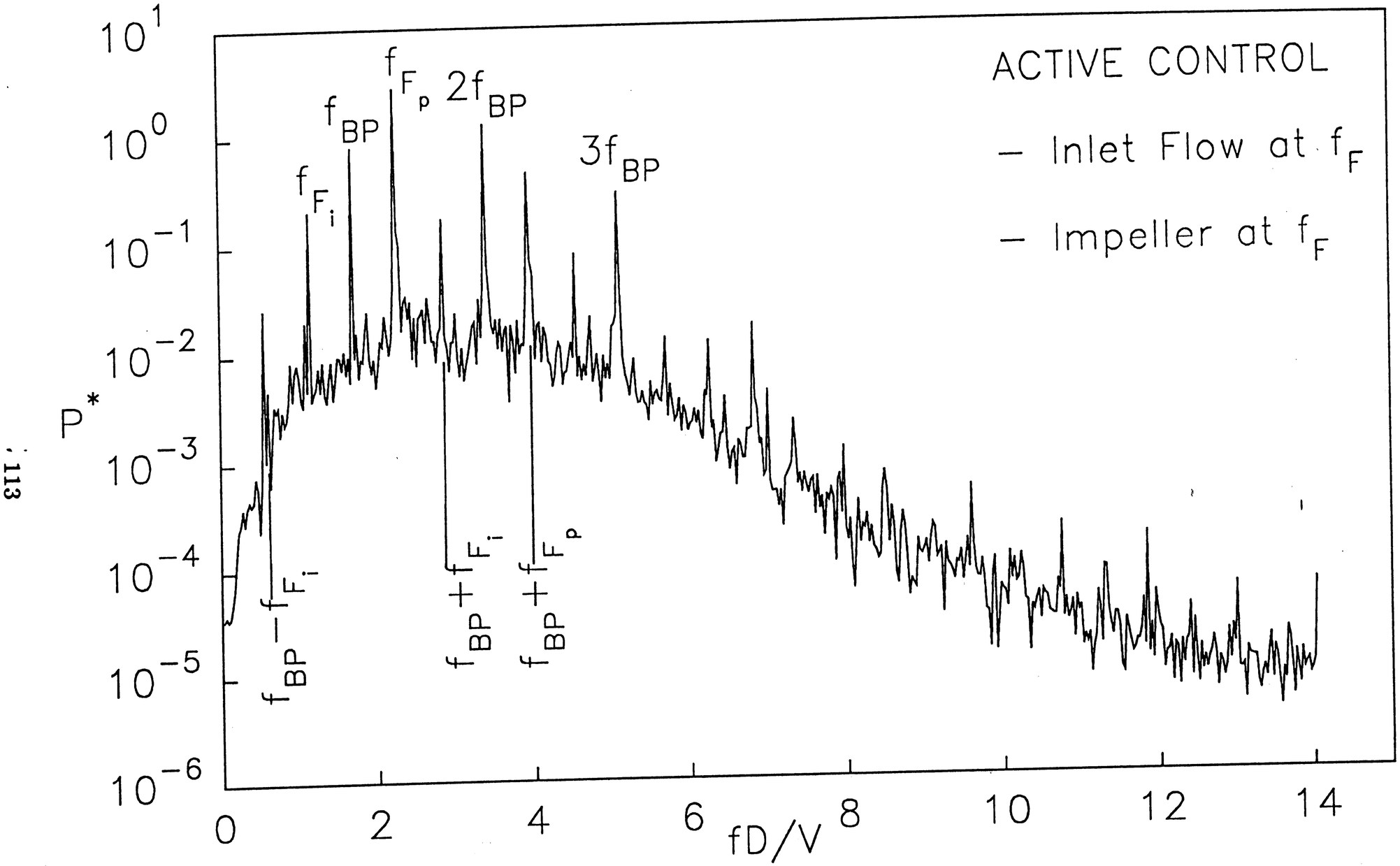

Figure 3.15.b (Plot P11)

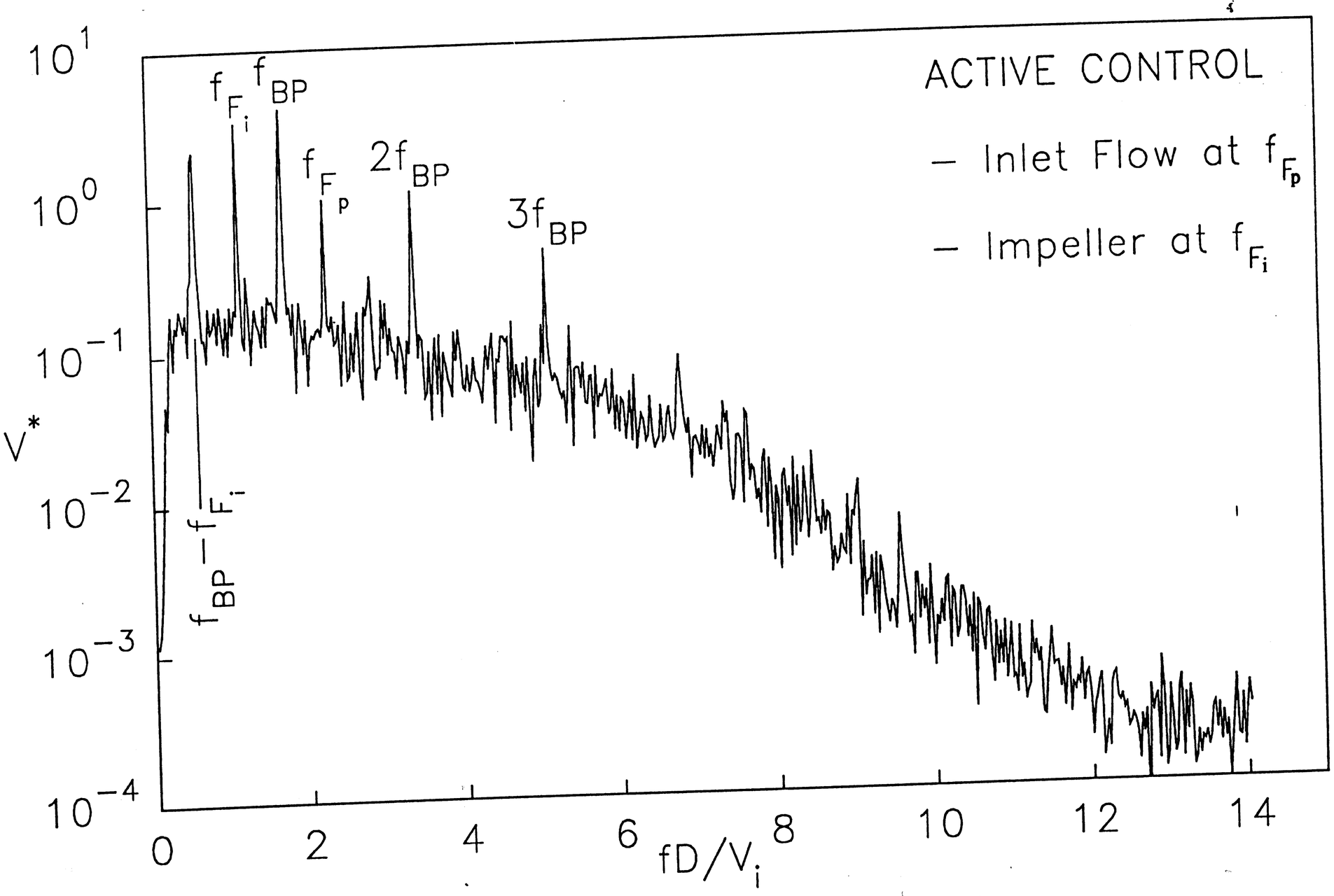

Figure 3.16.a (Plot V10)

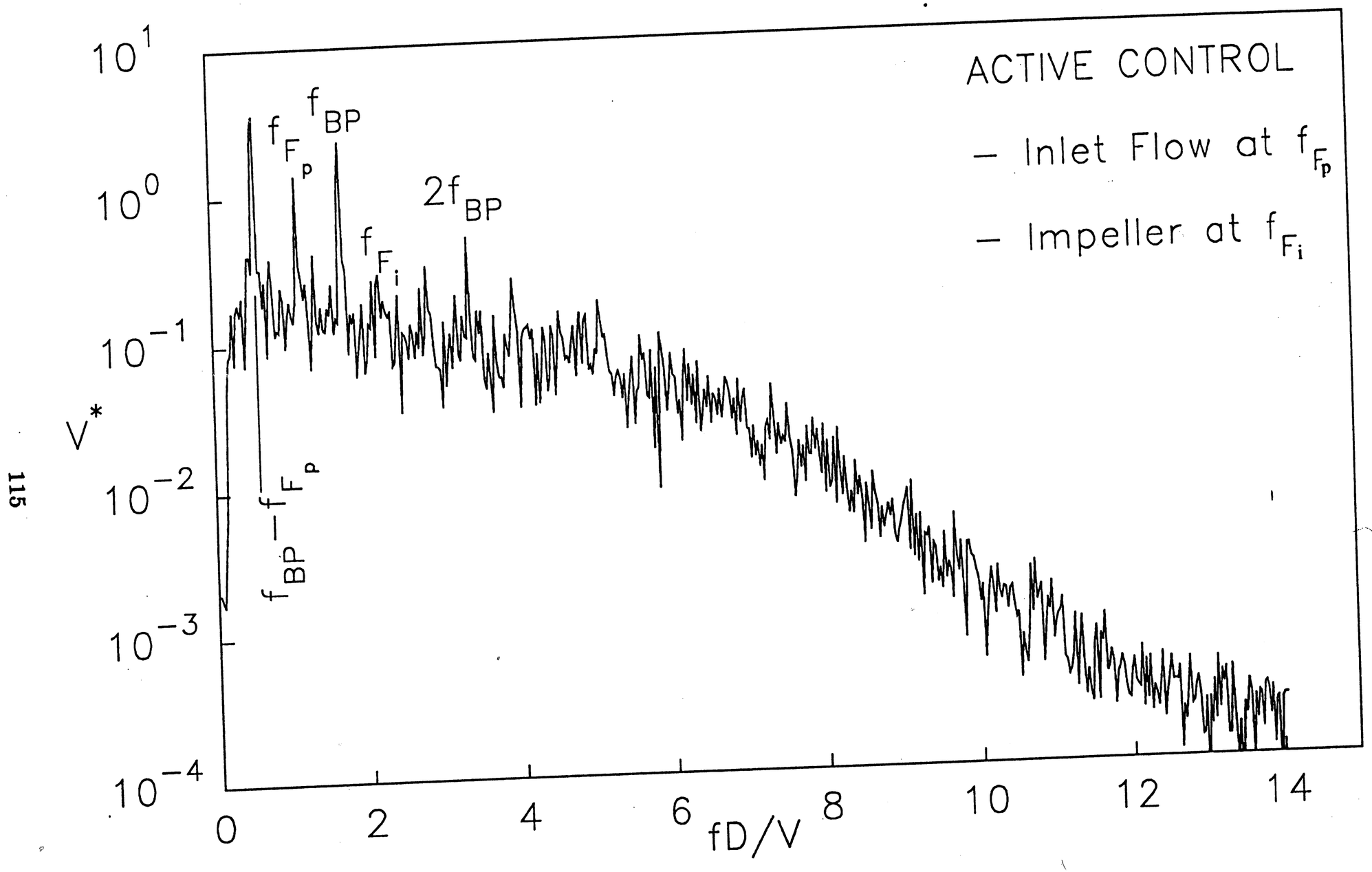

Figure 3.16.b (Plot V11)

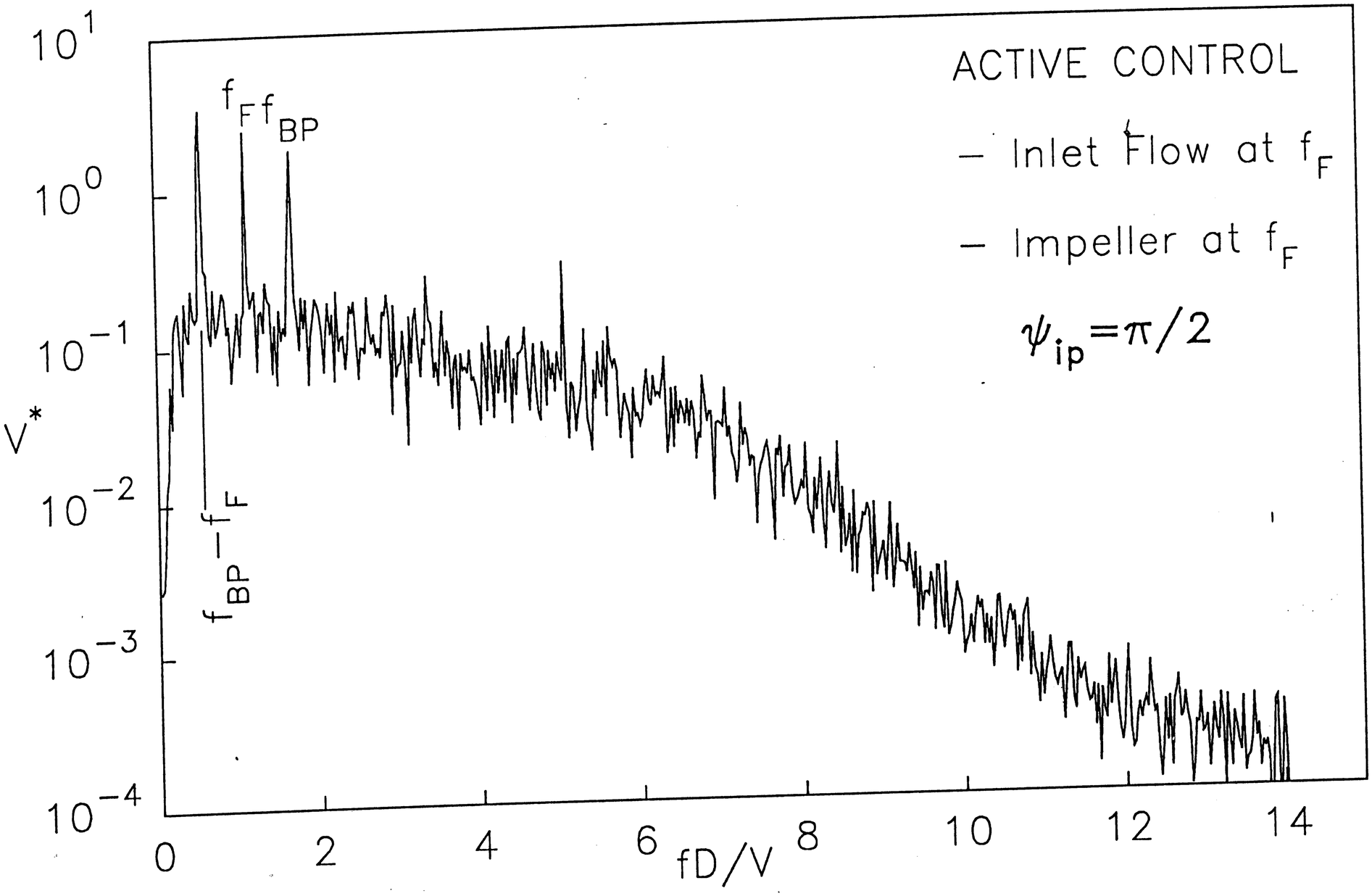

Figure 3.17.a (Plot V12)

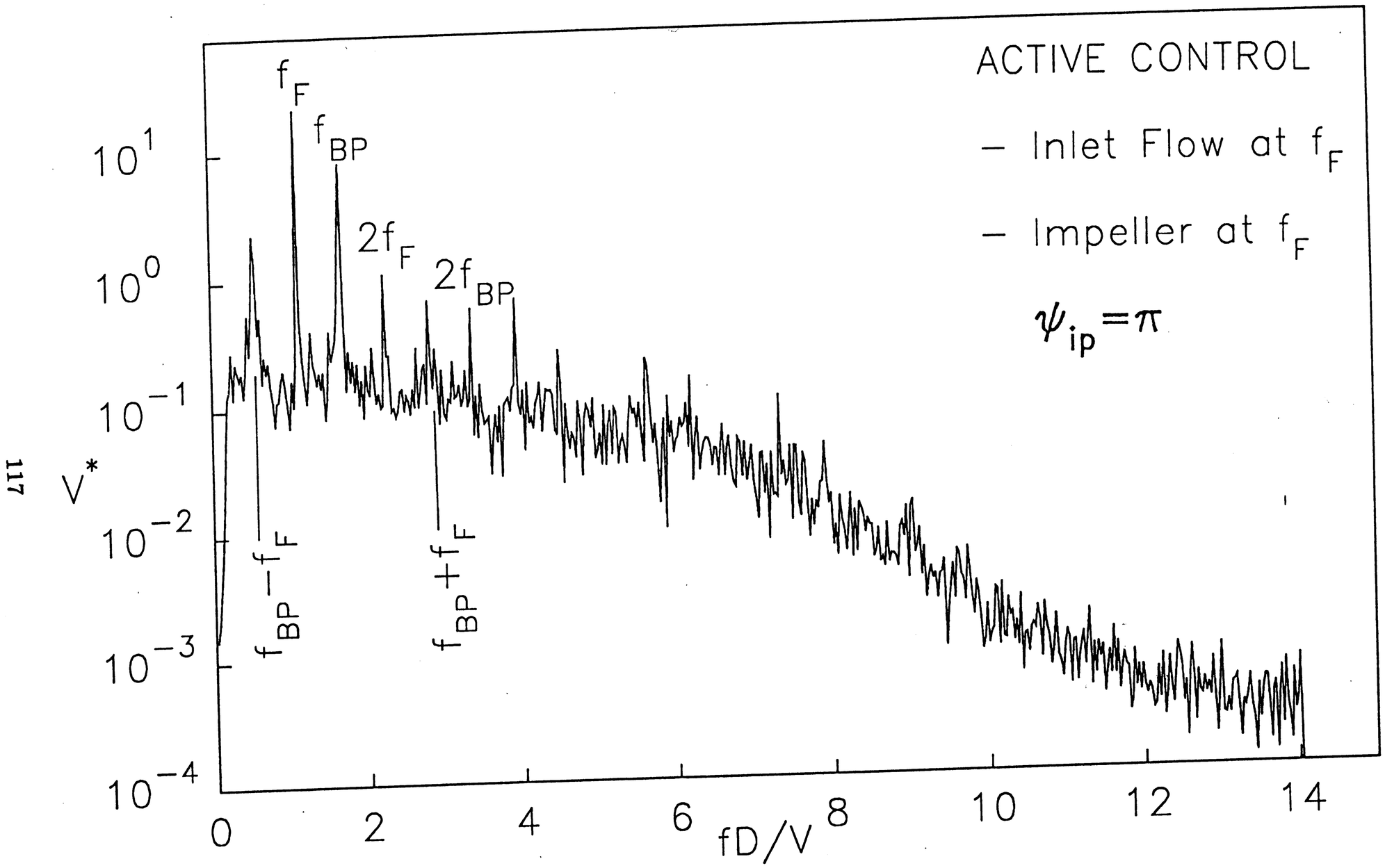

Figure 3.17.b (Plot V13)

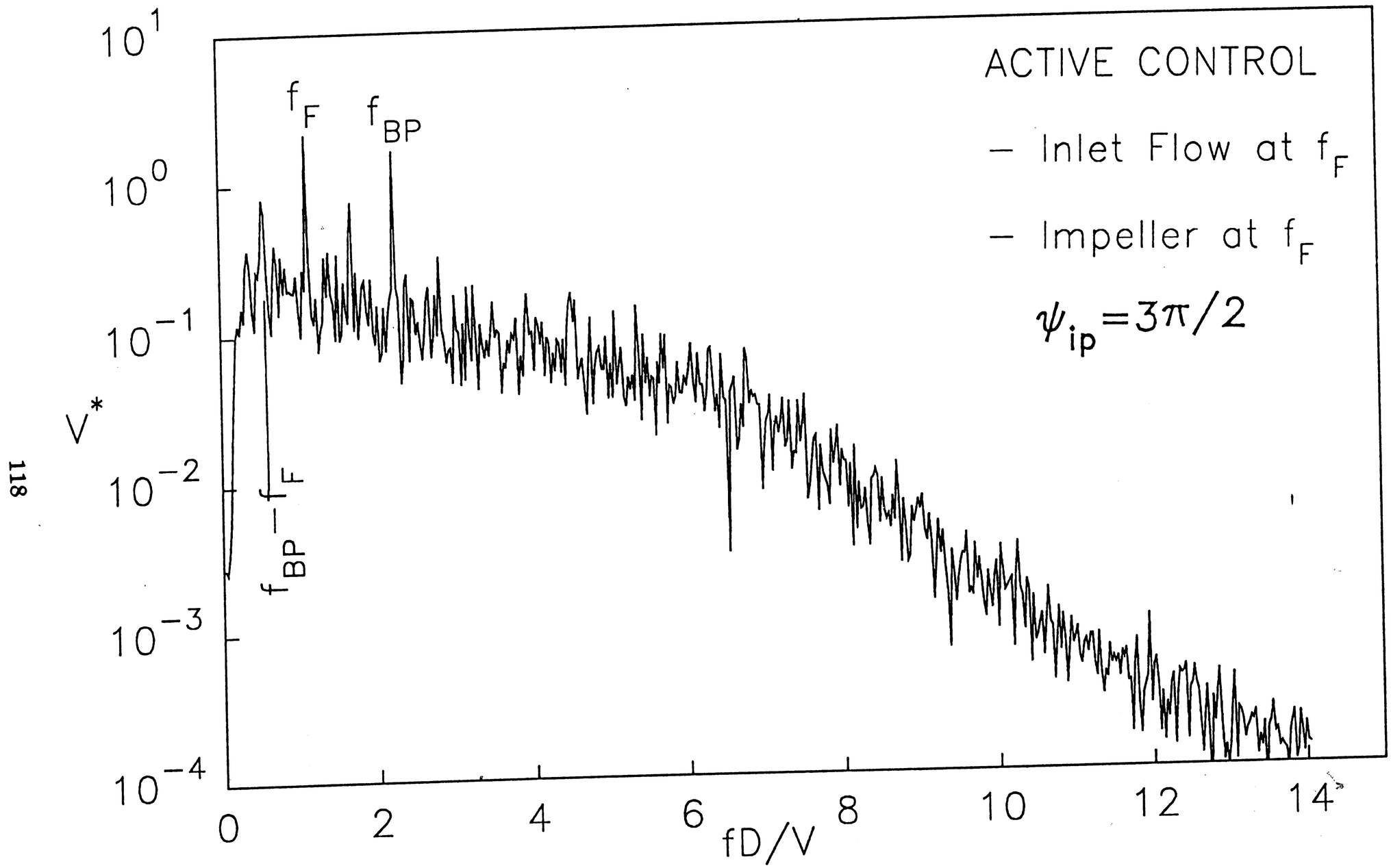

Figure 3.17.c (Plot V14)

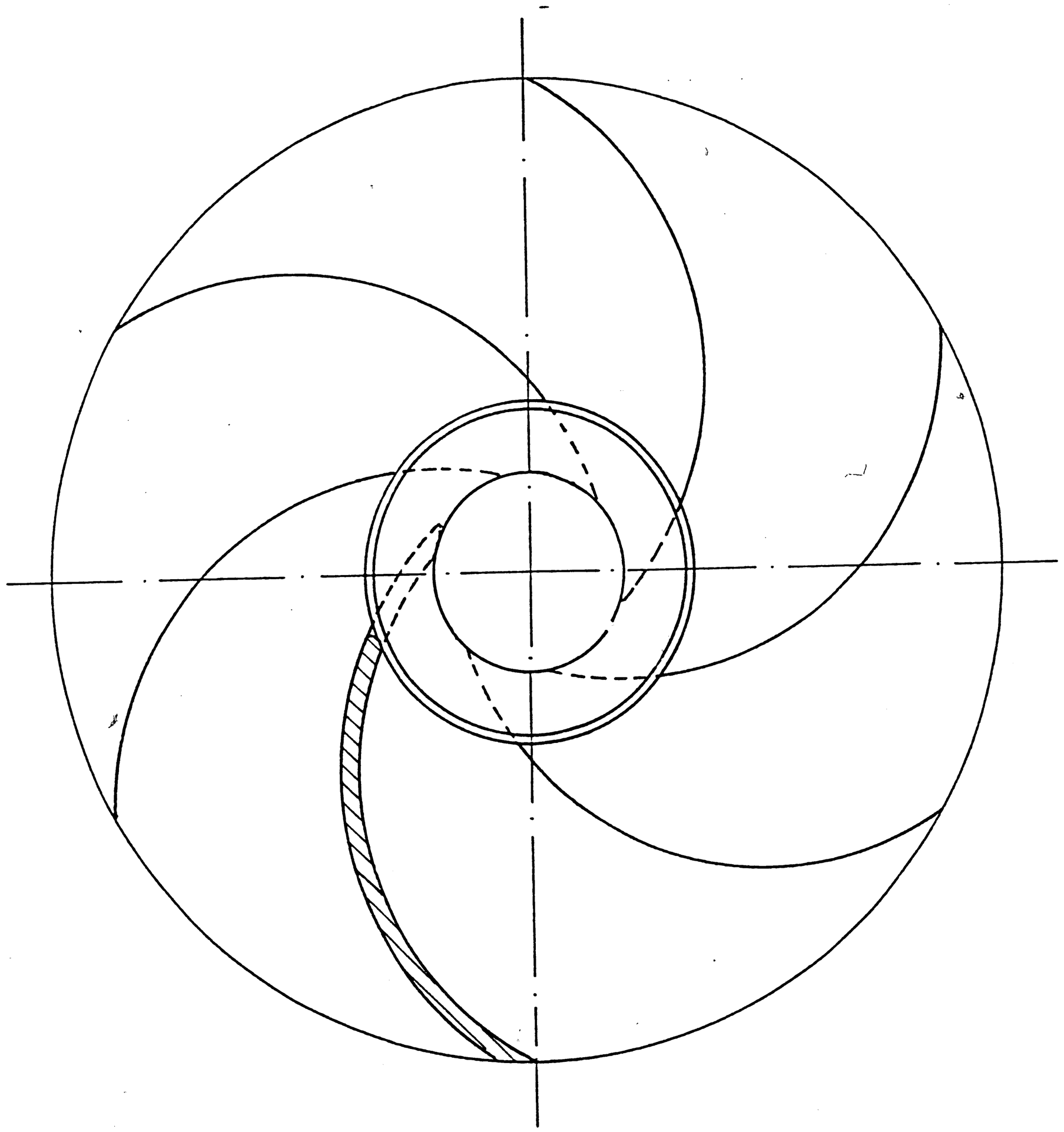

Figure 4.1: Six blade impeller.

f_{F_p}/f_{BP}=0.196

(a)

f_{F_p}/f_{BP}=0.39

(b)

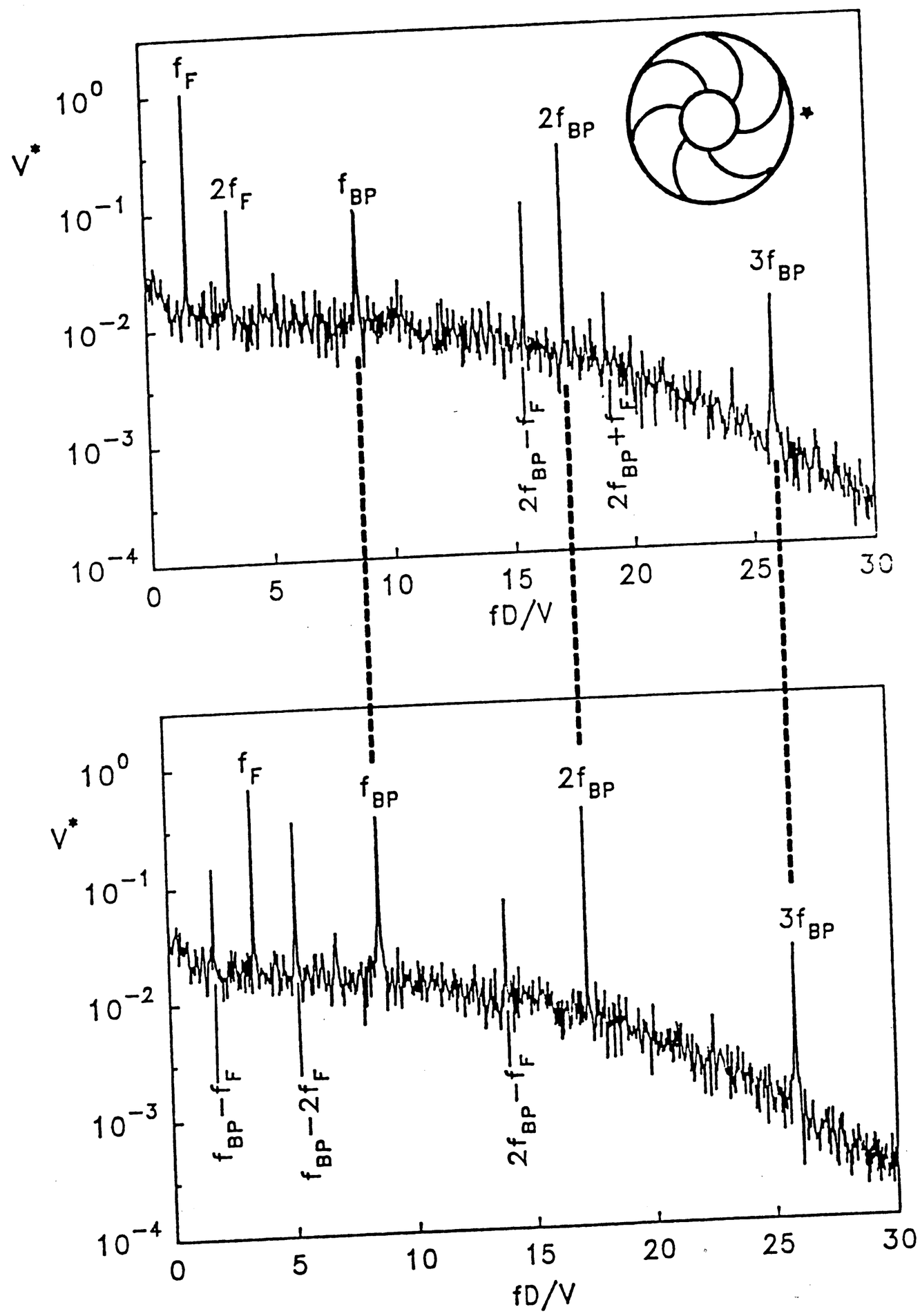

Figure 4.1.1

f_{F_p}/f_{BP}=0.78

(c)

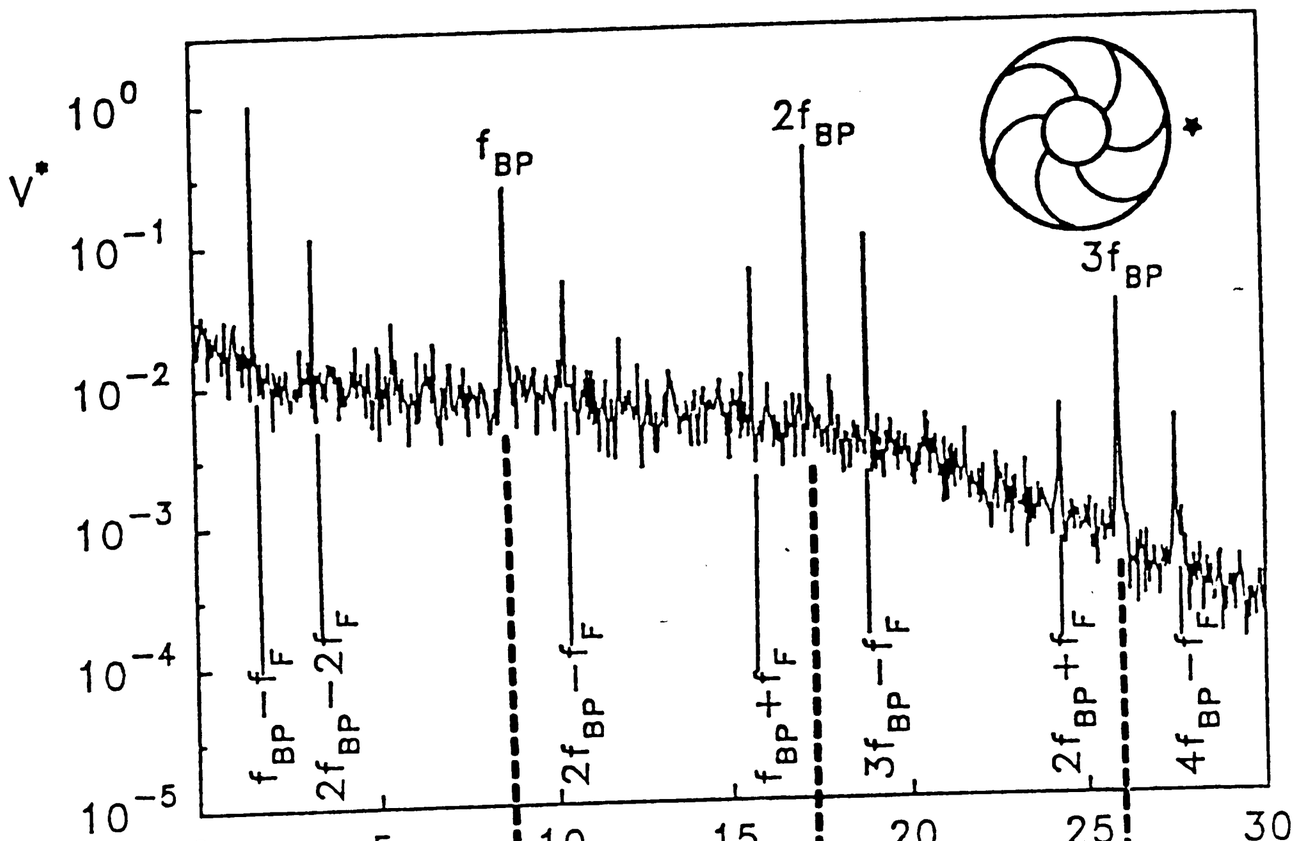

f_{F_p}/f_{BP}=0.88

(d)

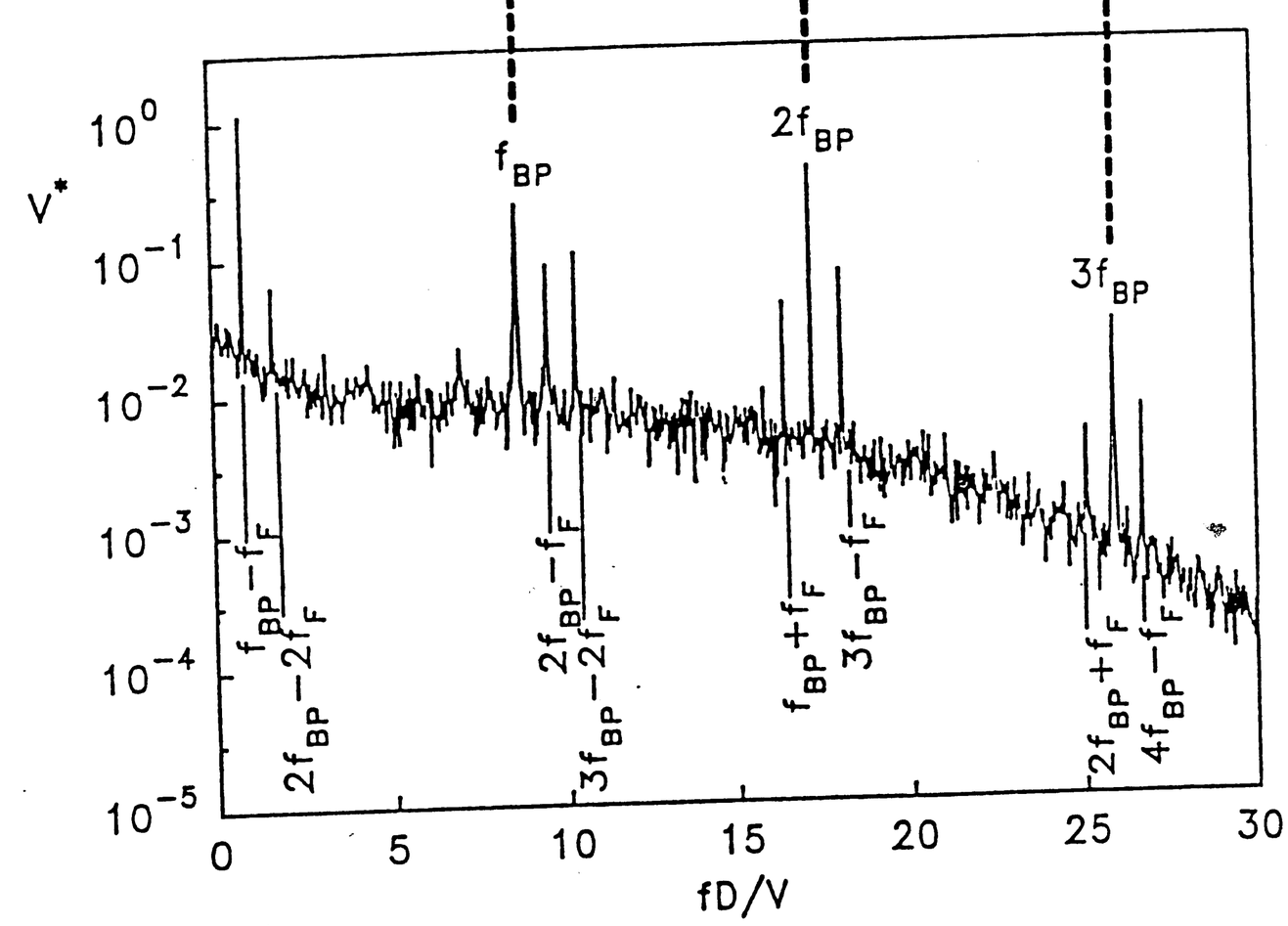

Figure 4.1.1

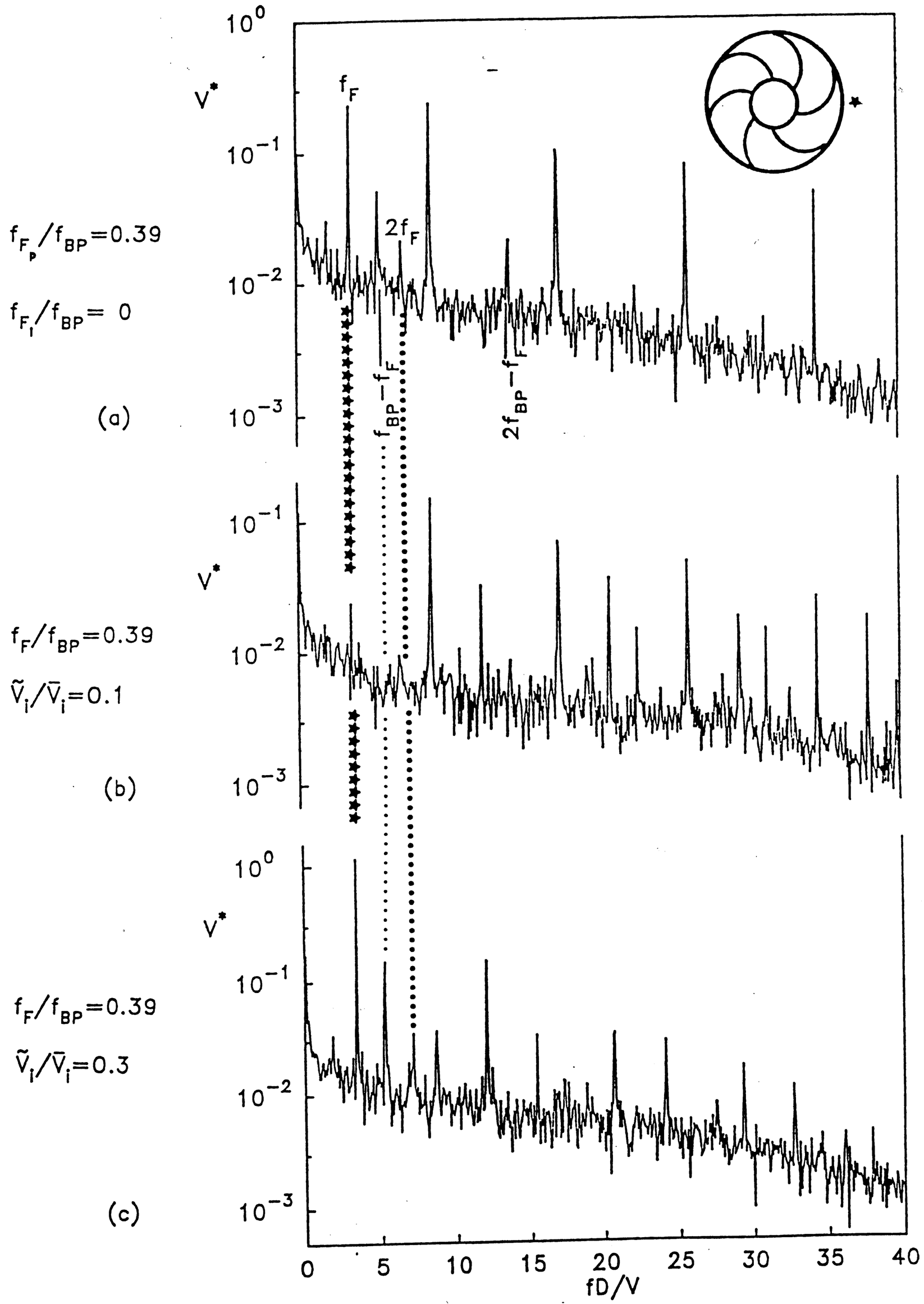
f_{F_p}/f_{BP}=0.39
f_{F_1}/f_{BP}= 0
(a)
f_F/f_{BP}=0.39
$\tilde{V}_i/\bar{V}_i$=0.1
(b)
f_F/f_{BP}=0.39
$\tilde{V}_i/\bar{V}_i$=0.3
(c)
V*
10^0
10^{-1}
10^{-2}
10^{-3}
f_F
$2f_F$
$f_{BP}-f_F$
f_{BP}
$2f_{BP}-f_F$
0
5
10
15
20
25
30
35
40
fD/V

Figure 4.1.2

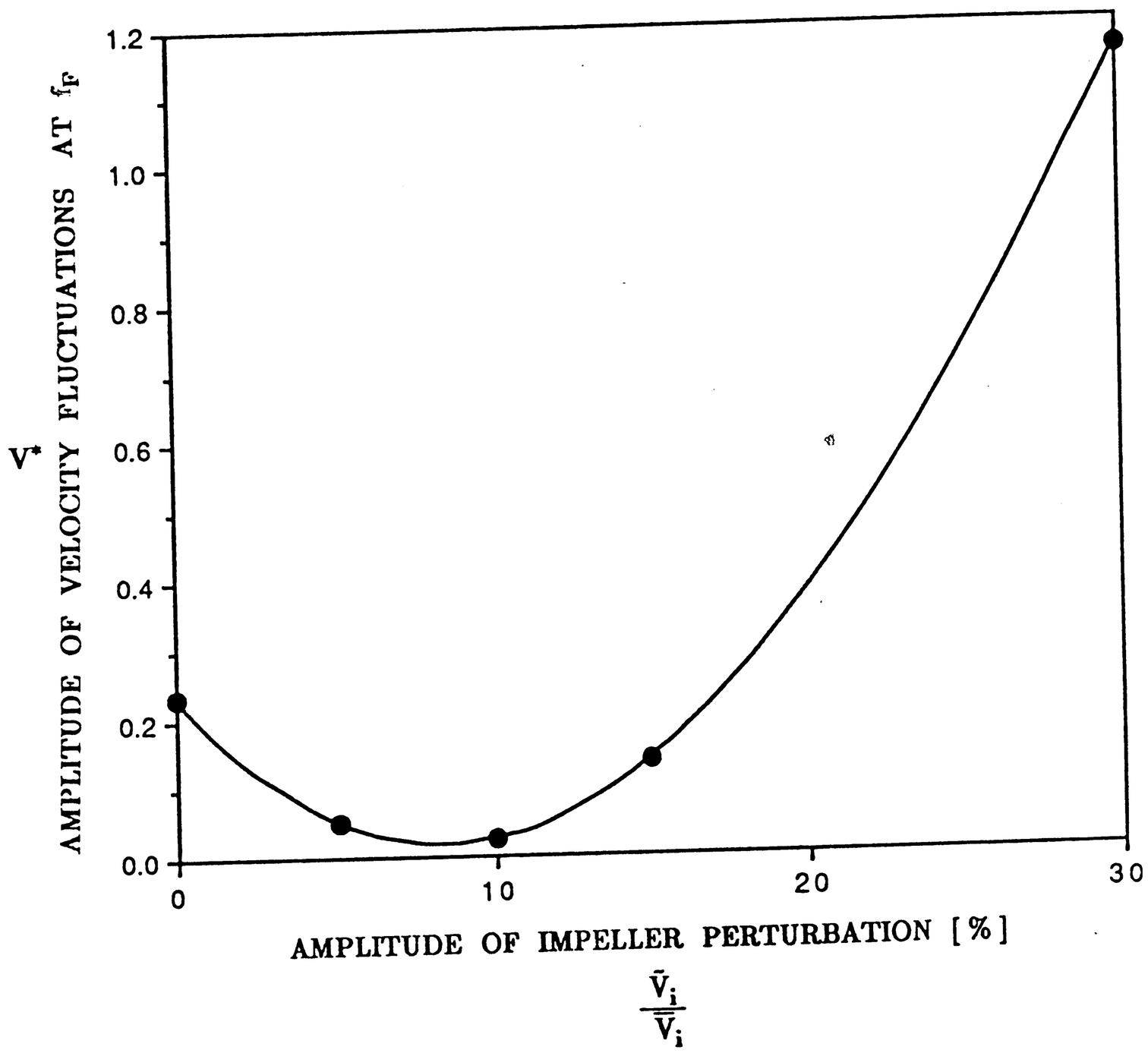
1.2
1.0
0.8
0.6
0.4
0.2
0.0
0
10
20
30
AMPLITUDE OF VELOCITY FLUCTUATIONS AT f_F
V^*
AMPLITUDE OF IMPELLER PERTURBATION [%]
$\tilde{V}_i$
$\overline{V}_i$

Figure 4.1.3

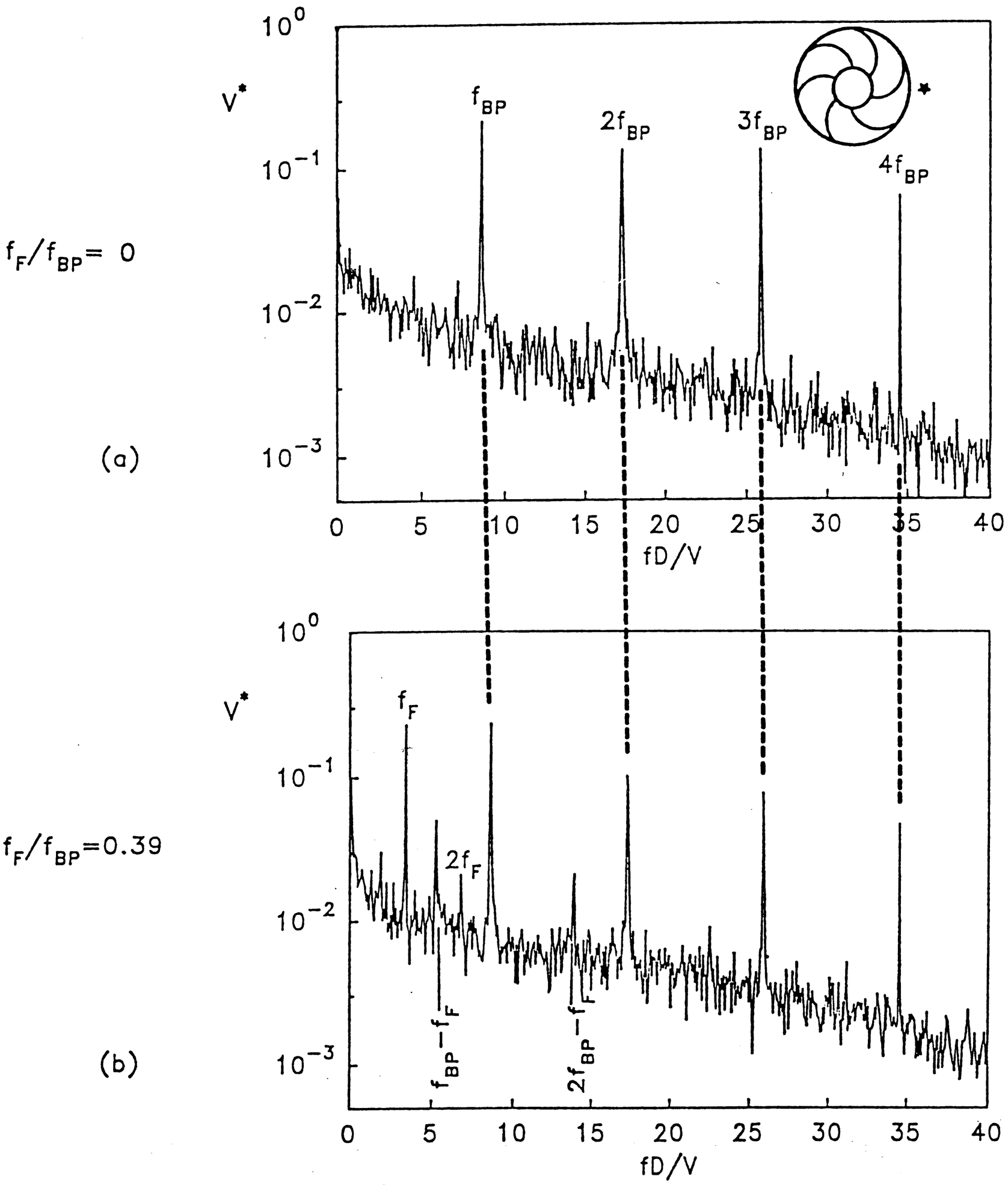
f_F/f_{BP}= 0
(a)
f_F/f_{BP}=0.39
(b)
10^0
10^{-1}
10^{-2}
10^{-3}
V*
f_{BP}
$2f_{BP}$
$3f_{BP}$
$4f_{BP}$
f_F
$2f_F$
$f_{BP}-f_F$
$2f_{BP}-f_F$
0 5 10 15 20 25 30 35 40
fD/V

Figure 4.1.4

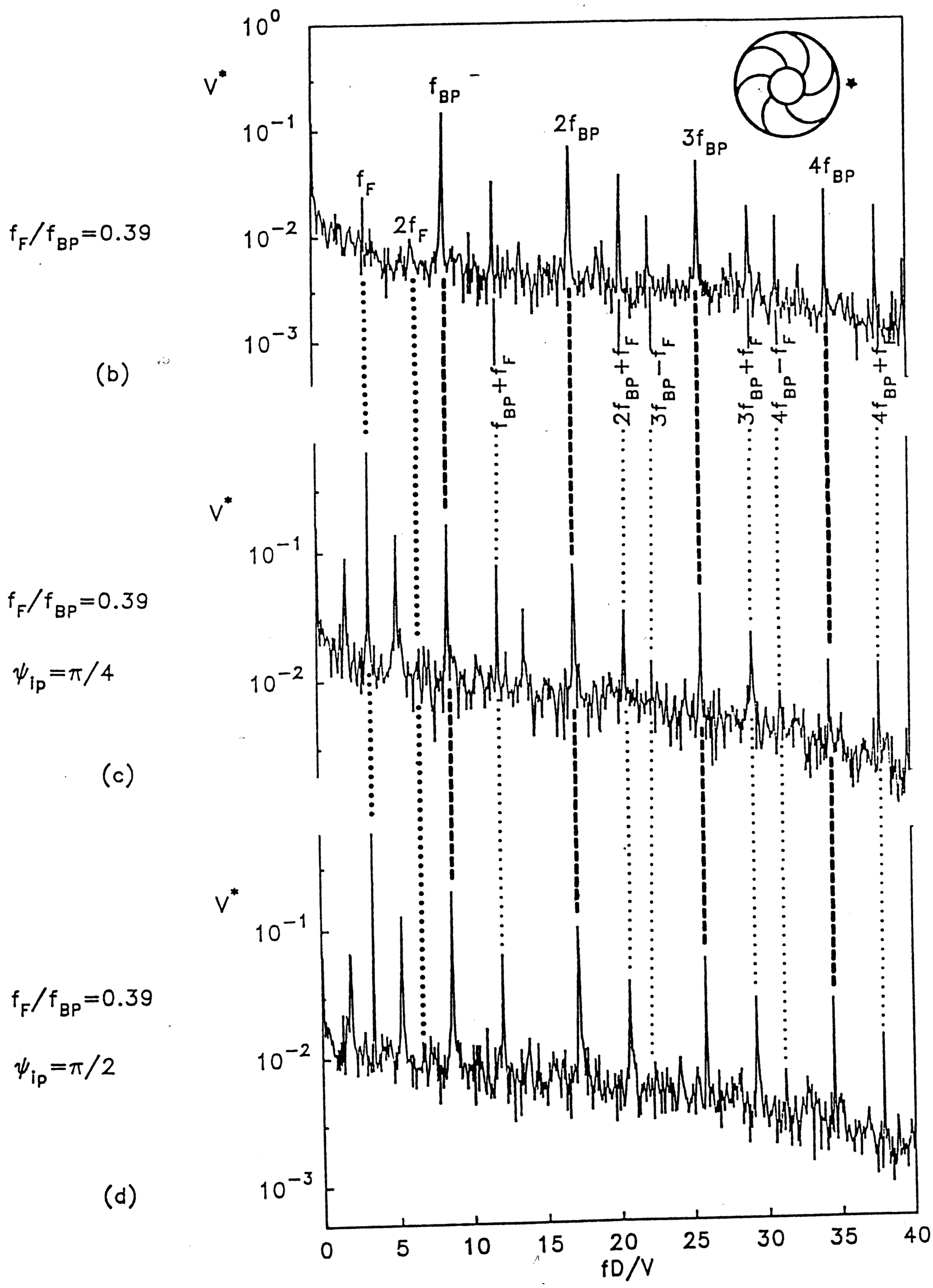

$f_F/f_{BP}=0.39$

(b)

$f_F/f_{BP}=0.39$

$\psi_{ip}=\pi/4$

(c)

$f_F/f_{BP}=0.39$

$\psi_{ip}=\pi/2$

(d)

Figure 4.1.4

f_F/f_{BP}=0.39

(b)

f_F/f_{BP}=0.39

$\psi_{ip}=3\pi/4$

(e)

f_F/f_{BP}=0.39

$\psi_{ip}=\pi$

(f)

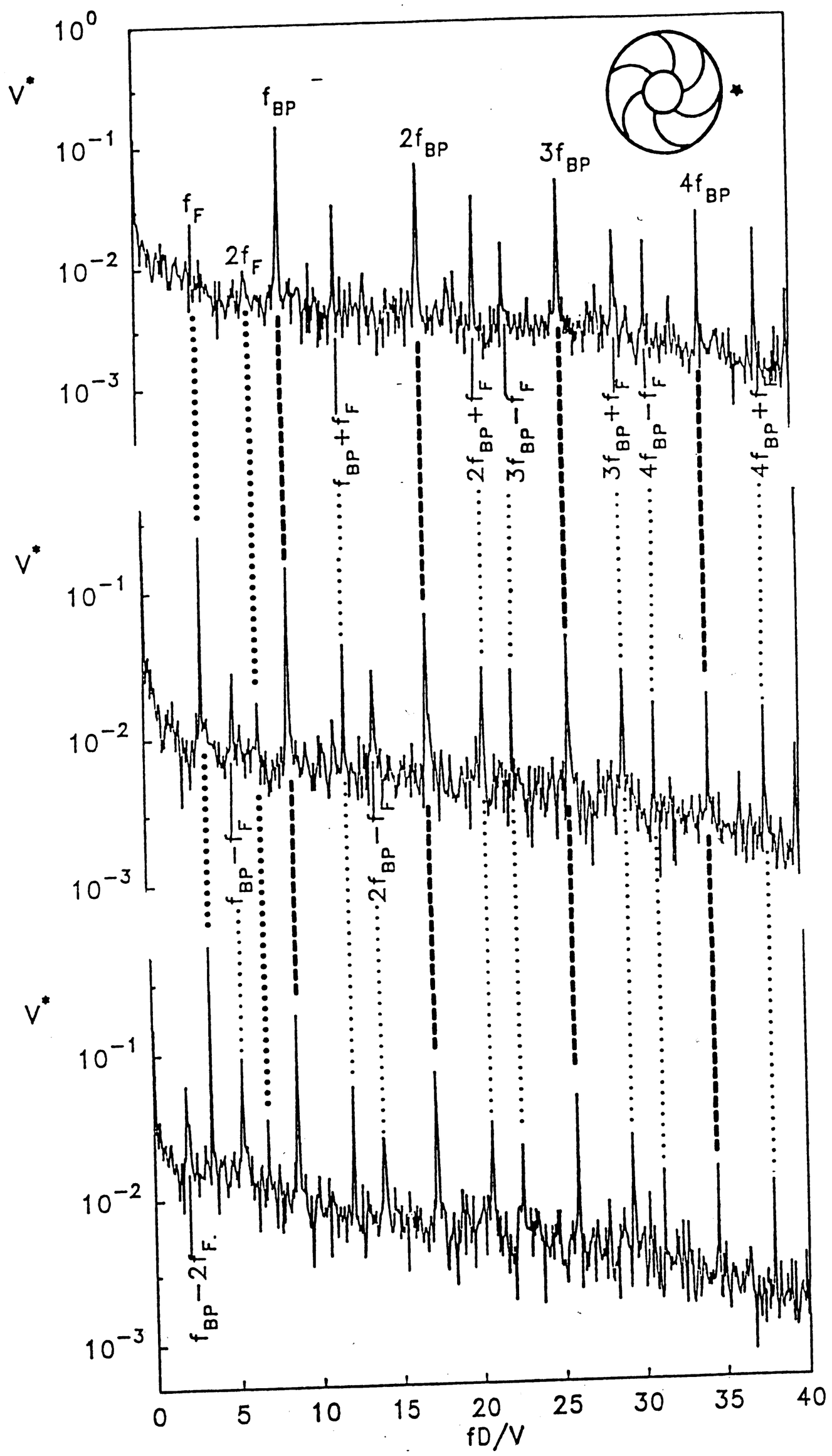

Figure 4.1.4

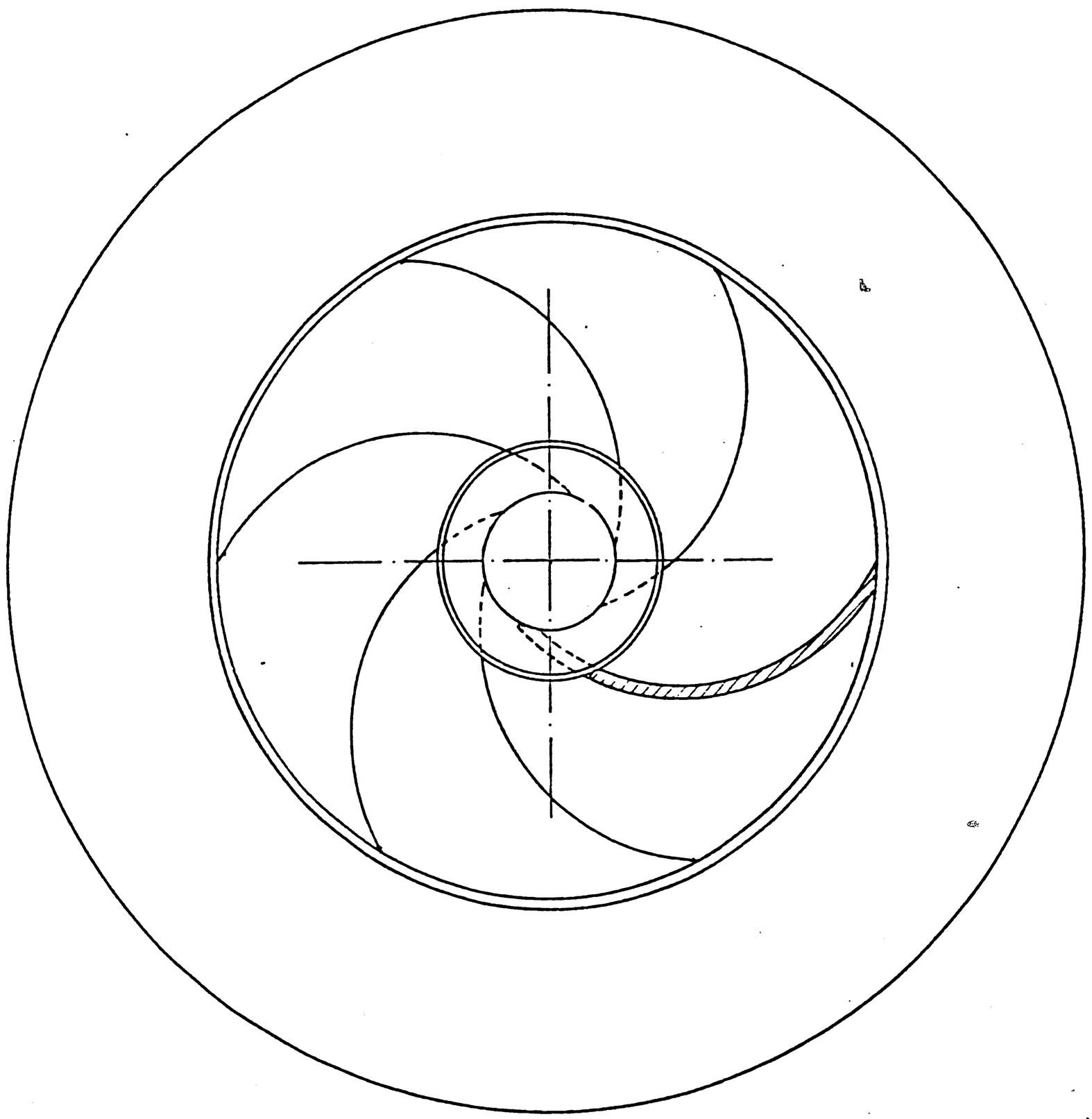

Figure 4.2: Six blade impeller and the diffuser discs.

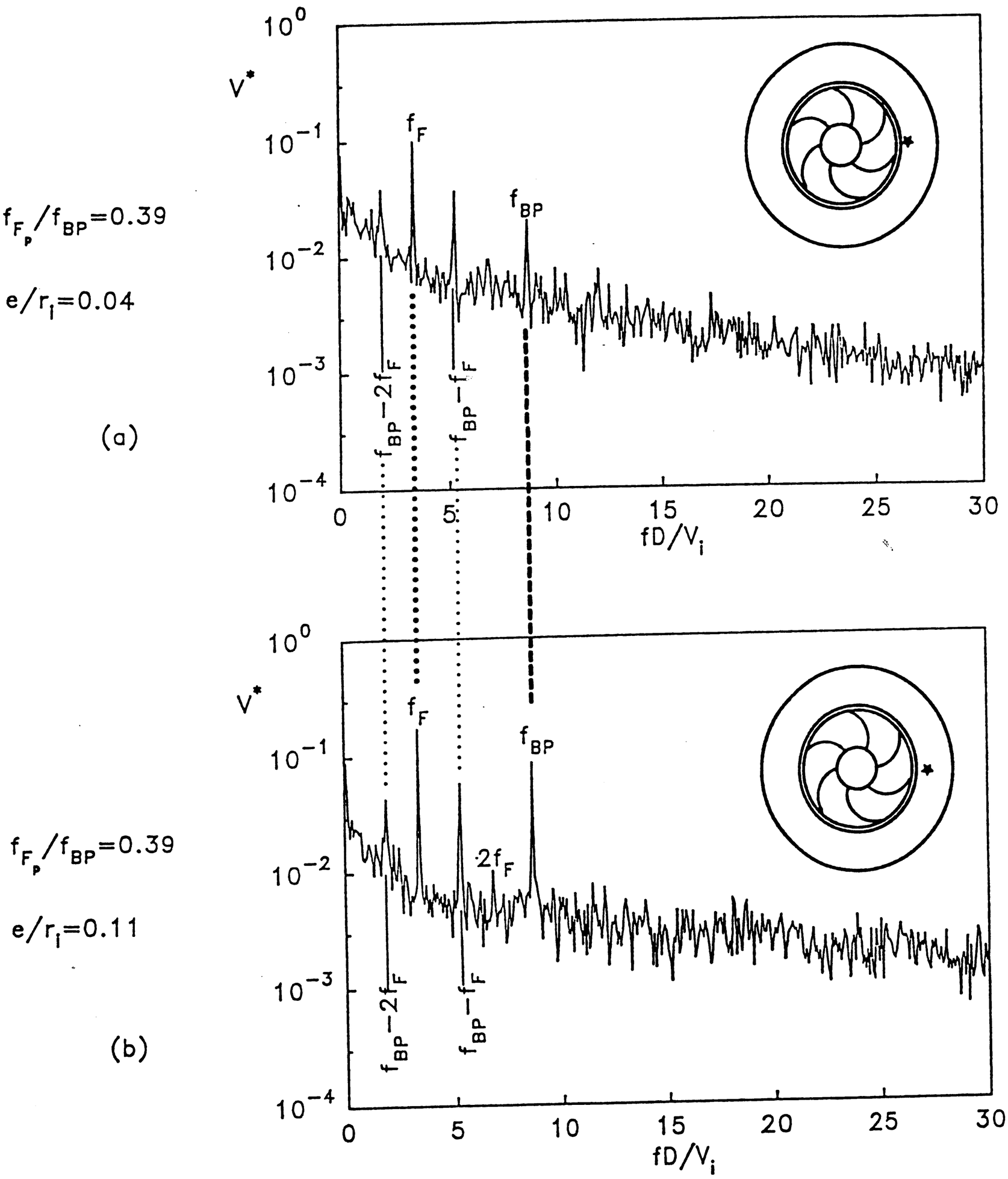
f_{F_p}/f_{BP}=0.39
e/r_i=0.04
(a)
f_{F_p}/f_{BP}=0.39
e/r_i=0.11
(b)
10^0
10^{-1}
10^{-2}
10^{-3}
10^{-4}
V*
f_F
f_{BP}
$2f_F$
$f_{BP}-2f_F$
$f_{BP}-f_F$
0
5
10
15
20
25
30
fD/V_i

Figure 4.2.1

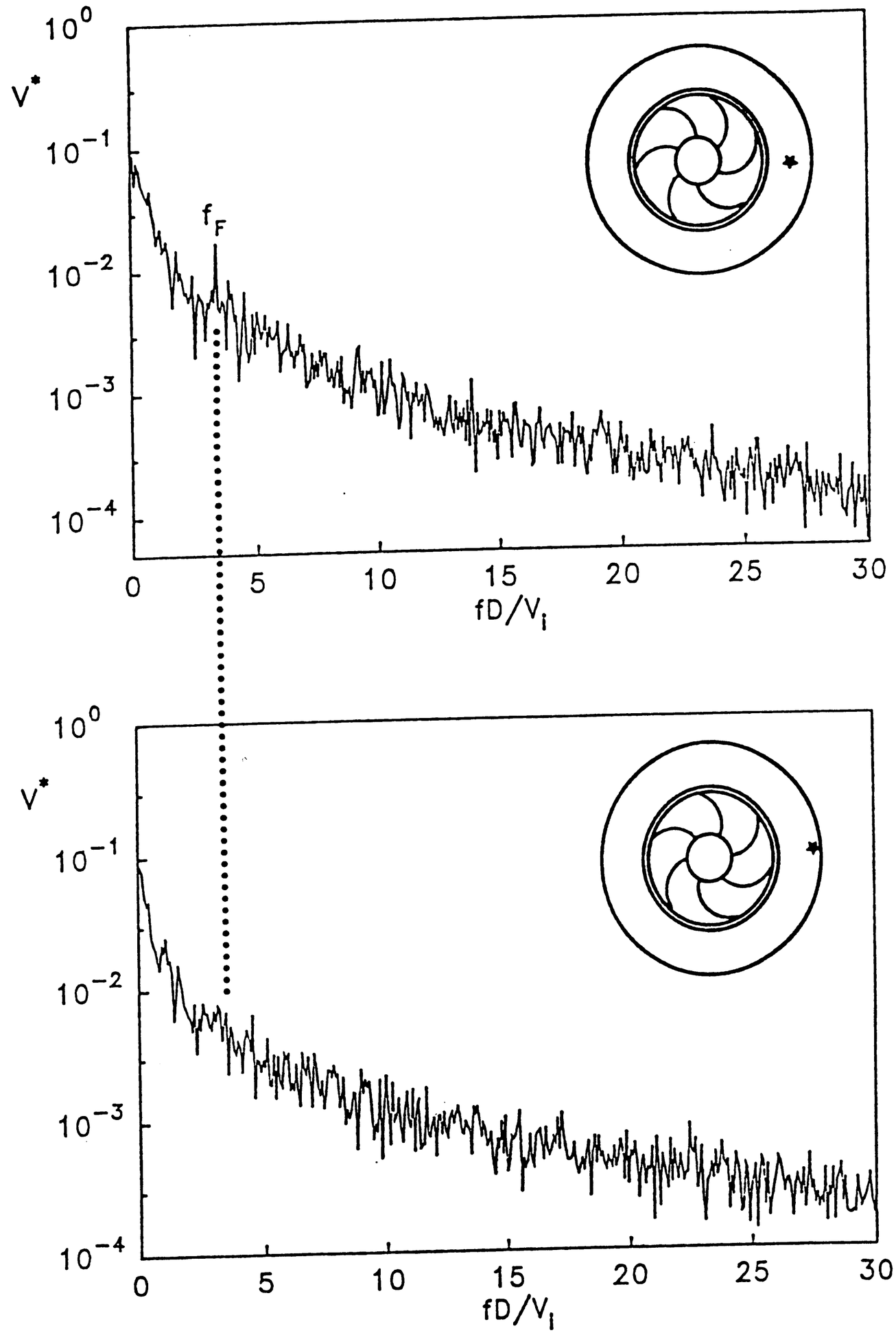

$f_{F_p}/f_{BP}=0.39$

$e/r_i=0.19$

(c)

$f_{F_p}/f_{BP}=0.39$

$e/r_i=0.44$

(d)

Figure 4.2

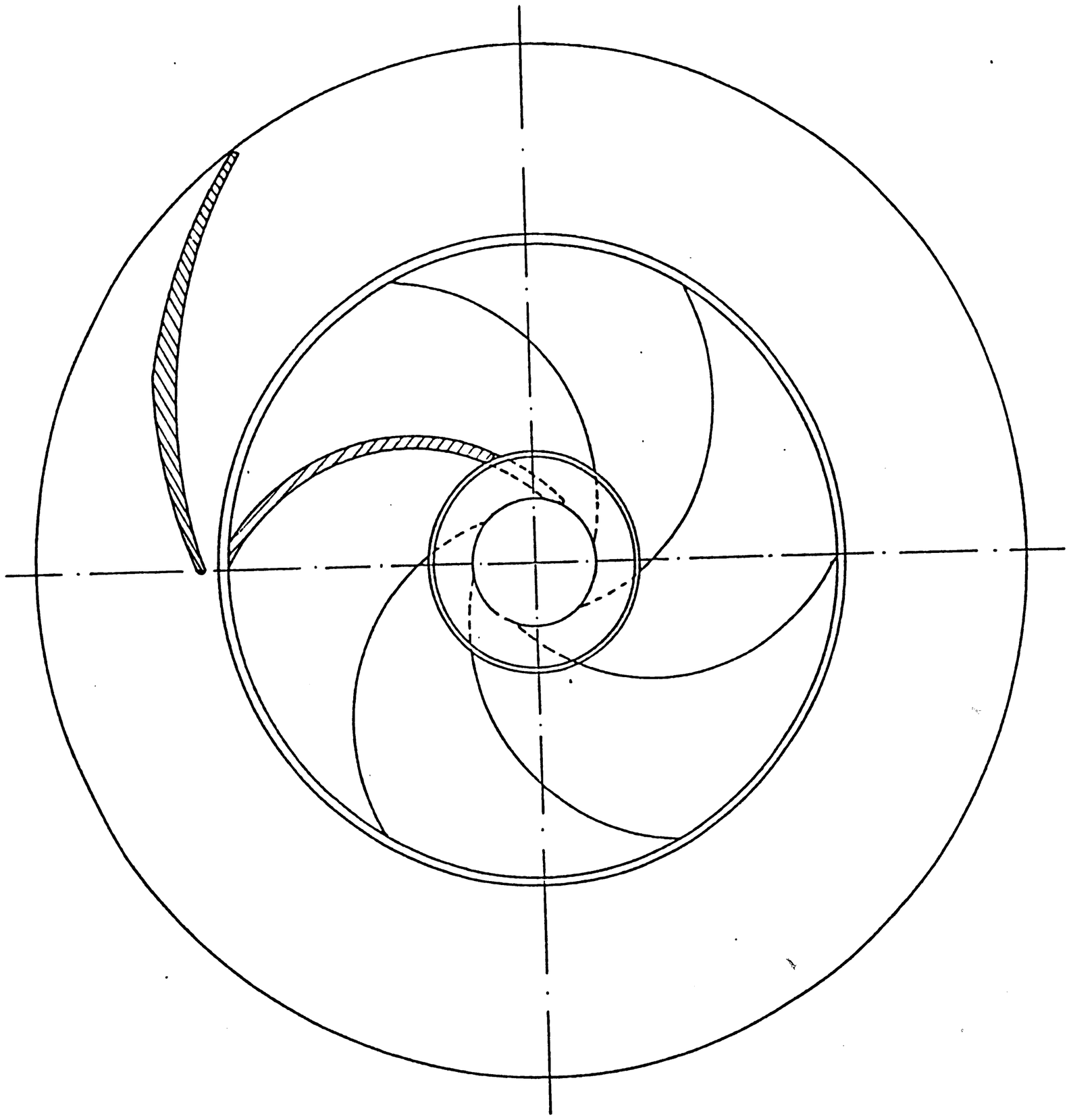

Figure 4.3: Six blade impeller, the diffuser discs and the diffuser blade.

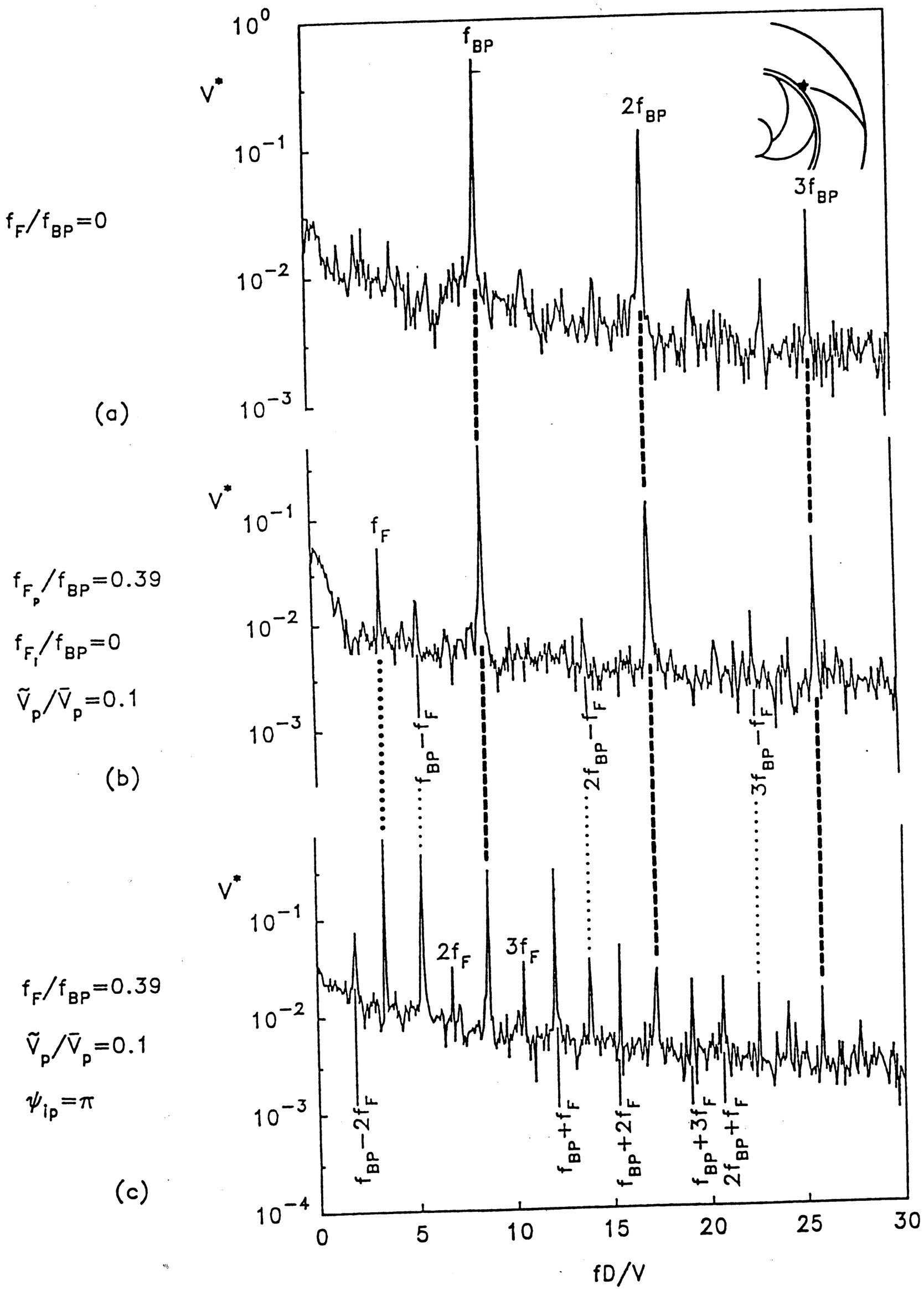
10^0
10^{-1}
10^{-2}
10^{-3}
V*
f_{BP}
$2f_{BP}$
$3f_{BP}$
$f_F/f_{BP}=0$
(a)
10^{-1}
10^{-2}
10^{-3}
V*
f_F
$f_{BP}-f_F$
$2f_{BP}-f_F$
$3f_{BP}-f_F$
$f_{F_p}/f_{BP}=0.39$
$f_{F_I}/f_{BP}=0$
$\tilde{V}_p/\bar{V}_p=0.1$
(b)
10^{-1}
10^{-2}
10^{-3}
10^{-4}
V*
$2f_F$
$3f_F$
$f_{BP}-2f_F$
$f_{BP}+f_F$
$f_{BP}+2f_F$
$f_{BP}+3f_F$
$2f_{BP}+f_F$
$f_F/f_{BP}=0.39$
$\tilde{V}_p/\bar{V}_p=0.1$
$\psi_{ip}=\pi$
(c)
0
5
10
15
20
25
30
fD/V

Figure 4.3.1

$f_F/f_{BP}=0$

(a)

$f_{F_p}/f_{BP}=0.39$

$f_{F_I}/f_{BP}=0$

$\tilde{V}_p/\bar{V}_p=0.3$

(b)

$f_F/f_{BP}=0.39$

$\tilde{V}_p/\bar{V}_p=0.3$

$\psi_{ip}=\pi$

(c)

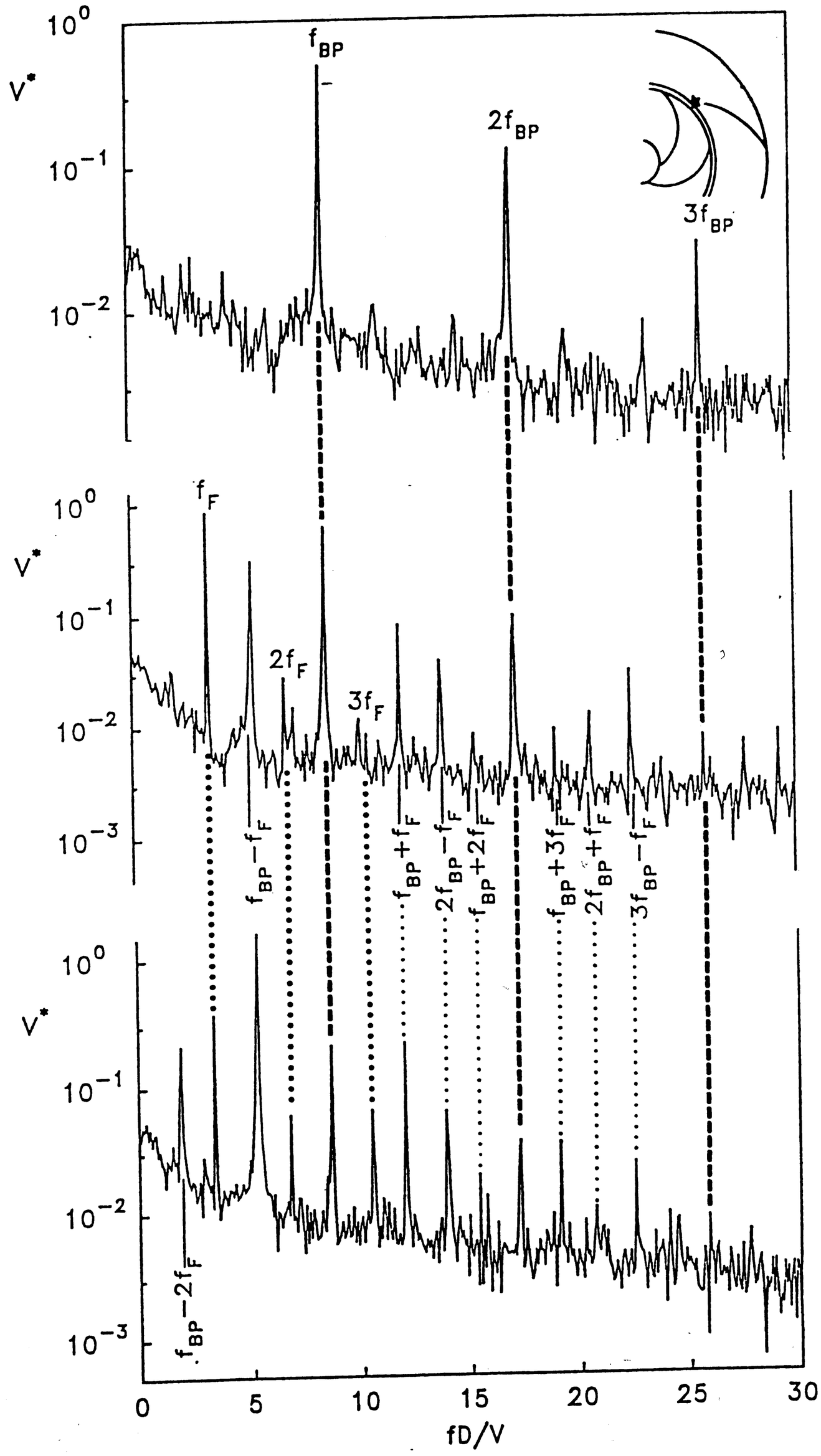

Figure 4.3.2

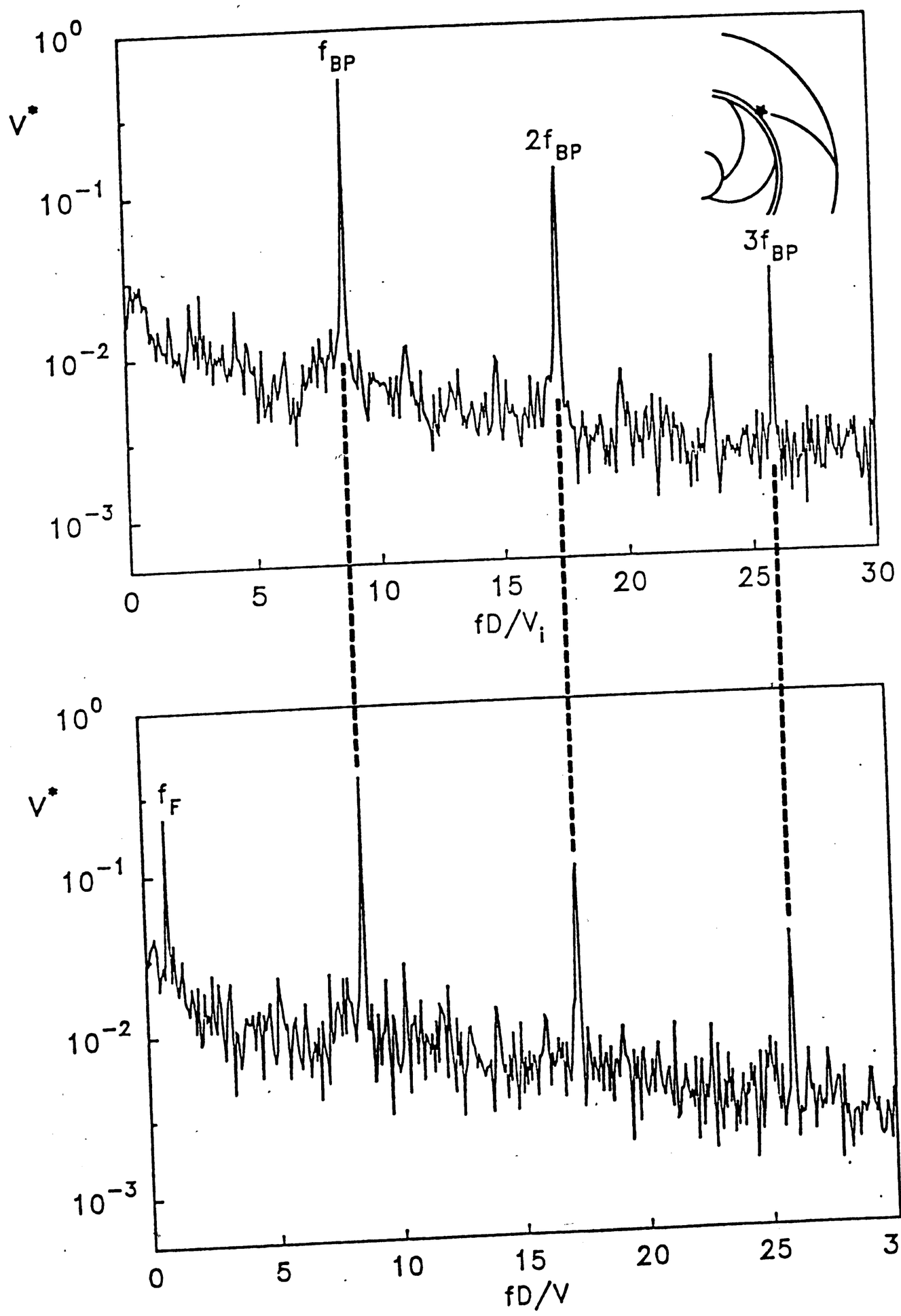
10^0
10^{-1}
10^{-2}
10^{-3}
V*
f_{BP}
$2f_{BP}$
$3f_{BP}$
0
5
10
15
20
25
30
fD/V_i
f_F/f_{BP}=0
(a)
f_{F_p}/f_{BP}=0.1
f_{F_i}/f_{BP}=0
f_F
fD/V
(b)

Figure 4 .3.3

$f_{F_p}/f_{BP}=0.1$

$f_{F_i}/f_{BP}=0$

(b)

$f_F/f_{BP}=0.1$

(c)

$f_F/f_{BP}=0.1$

$\psi_{ip}=\pi$

(d)

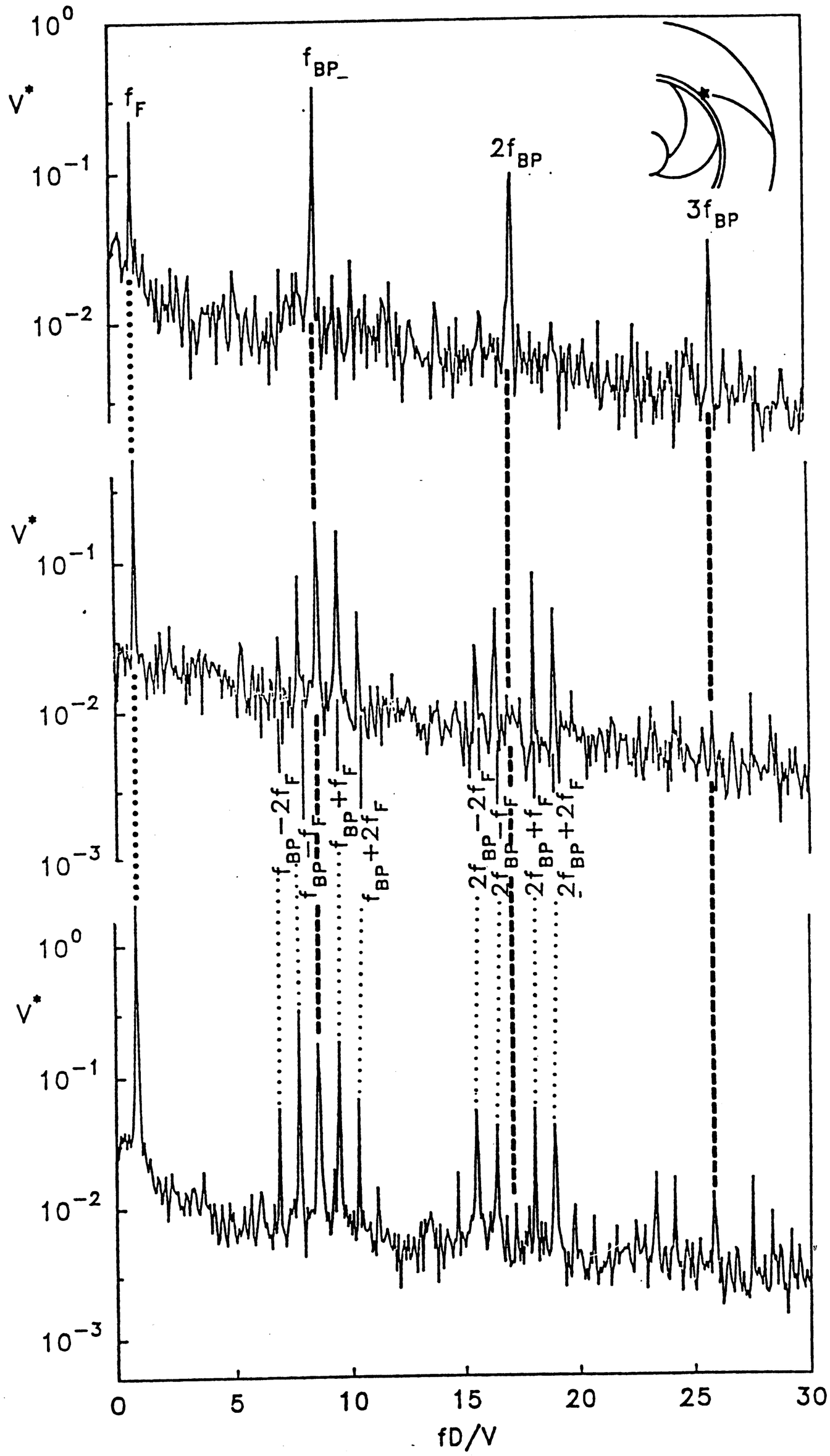

Figure 4.3.3

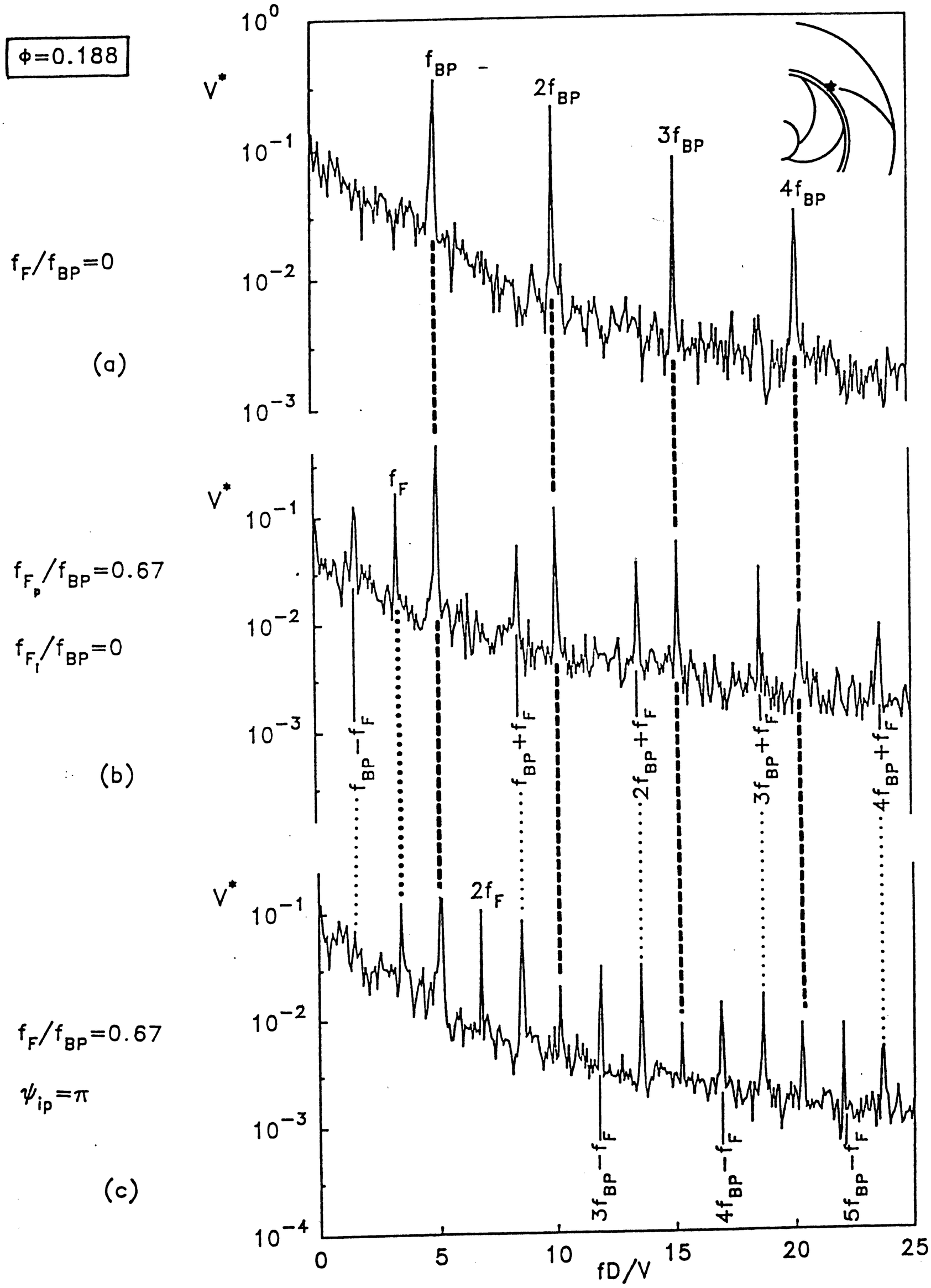
Φ=0.188
f_F/f_{BP}=0
(a)
f_{F_p}/f_{BP}=0.67
f_{F_i}/f_{BP}=0
(b)
f_F/f_{BP}=0.67
$\psi_{ip}=\pi$
(c)
V*
10^0
10^{-1}
10^{-2}
10^{-3}
10^{-4}
f_{BP}
$2f_{BP}$
$3f_{BP}$
$4f_{BP}$
f_F
$2f_F$
$f_{BP}-f_F$
$f_{BP}+f_F$
$2f_{BP}+f_F$
$3f_{BP}+f_F$
$4f_{BP}+f_F$
$3f_{BP}-f_F$
$4f_{BP}-f_F$
$5f_{BP}-f_F$
0
5
10
15
20
25
fD/V

Figure 4.3.4

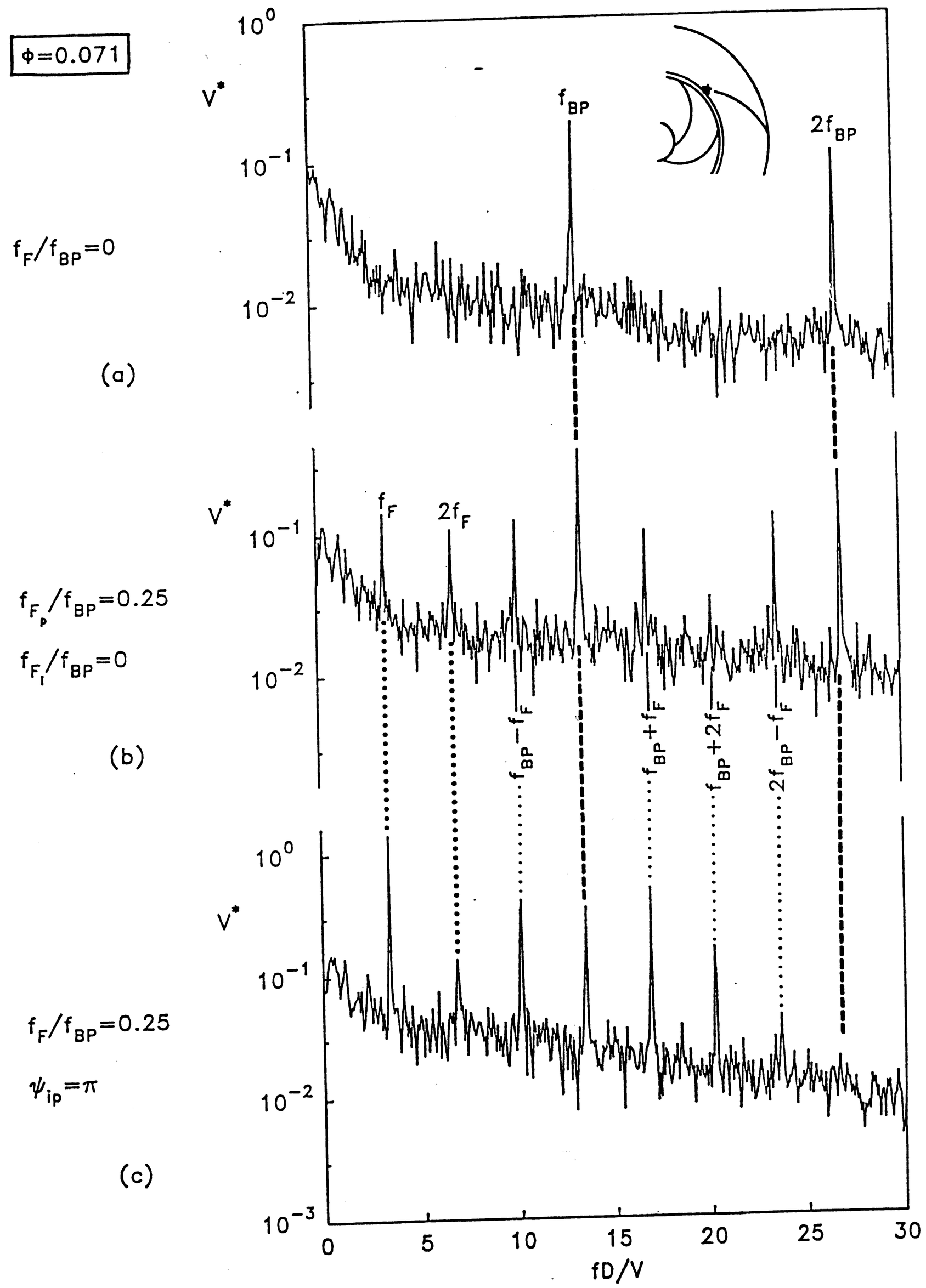
φ=0.071
f_F/f_{BP}=0
(a)
f_{F_p}/f_{BP}=0.25
f_{F_I}/f_{BP}=0
(b)
f_F/f_{BP}=0.25
$\psi_{ip}=\pi$
(c)
V*
10^0
10^{-1}
10^{-2}
10^{-3}
f_{BP}
$2f_{BP}$
f_F
$2f_F$
$f_{BP}-f_F$
$f_{BP}+f_F$
$f_{BP}+2f_F$
$2f_{BP}-f_F$
0
5
10
15
20
25
30
fD/V

Figure 4.3.5

$f_{F_p}/f_{BP}=0.39$

$f_{F_i}/f_{BP}=0$

(a)

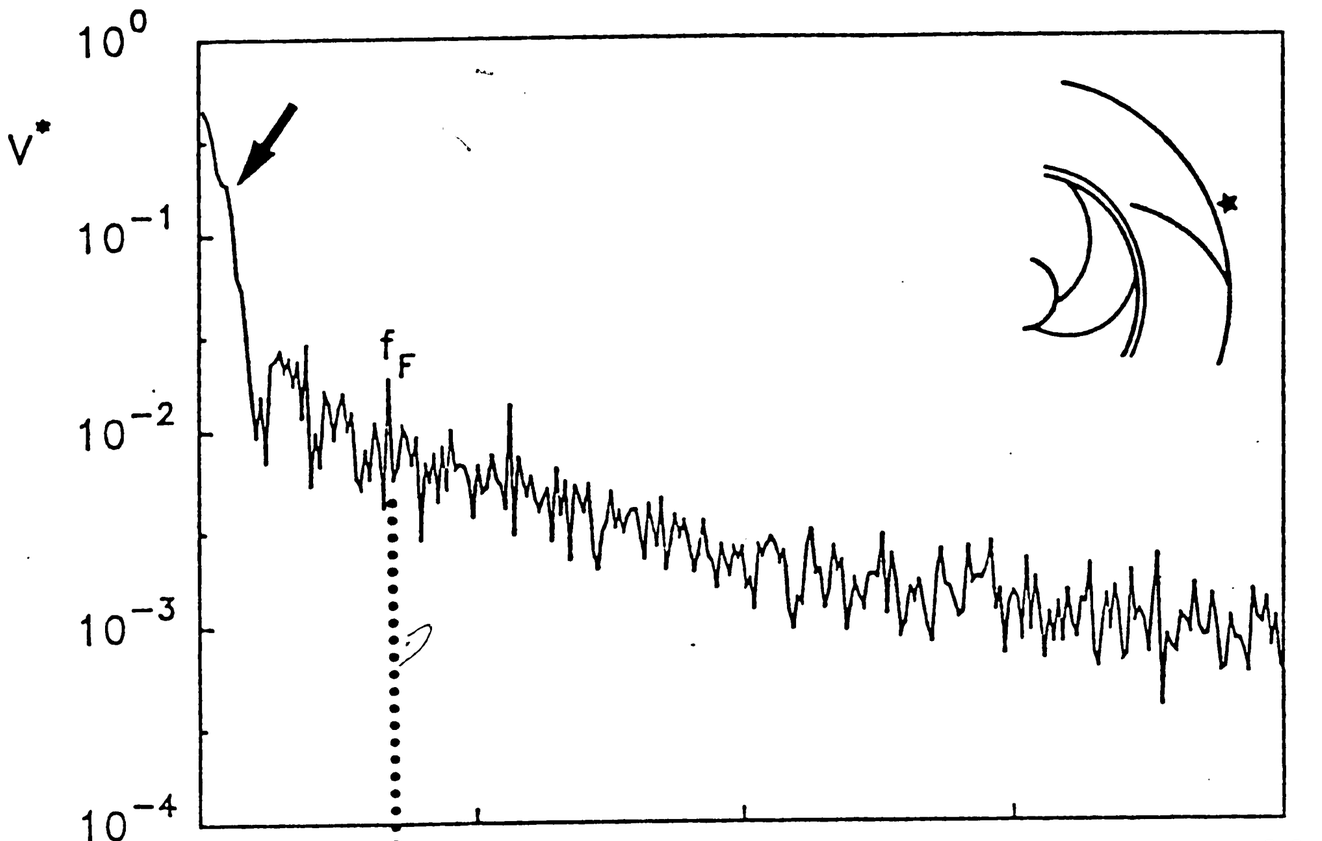

$f_F/f_{BP}=0.39$

$\psi_{ip}=\pi$

(b)

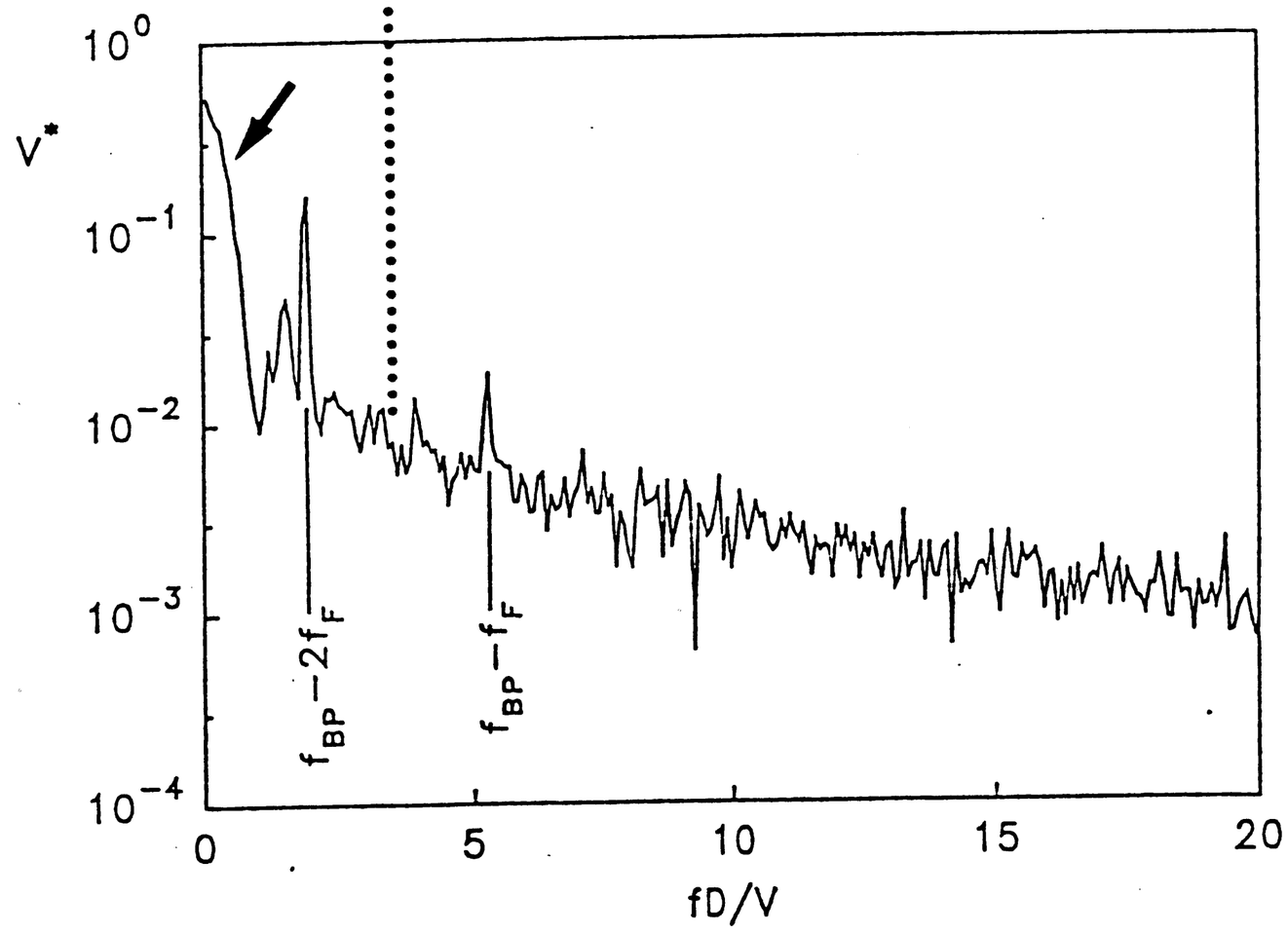

Figure 4.3.6

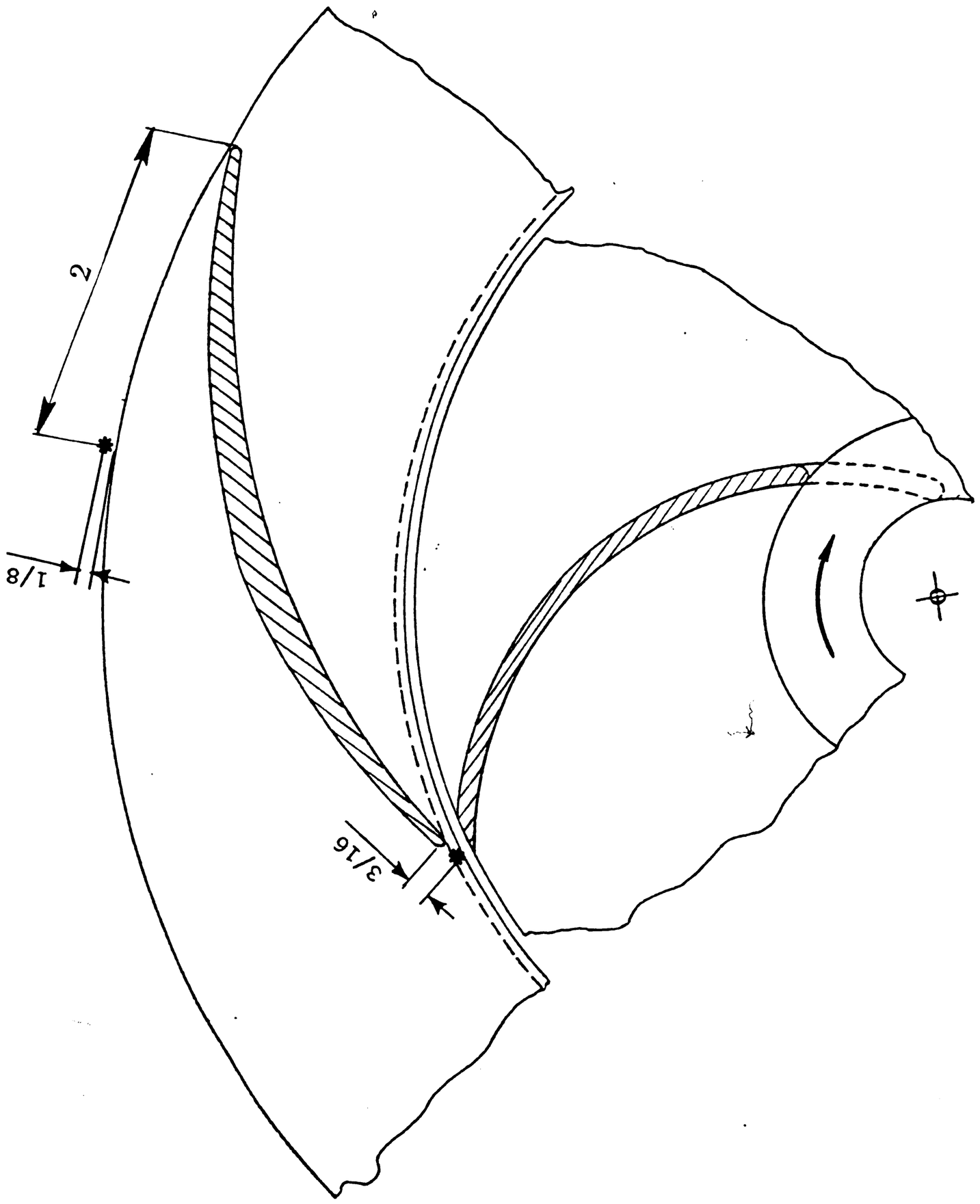

Figure 4.3.7 Location of LDV measurement volume during the experiments in the presence of vaned diffuser.

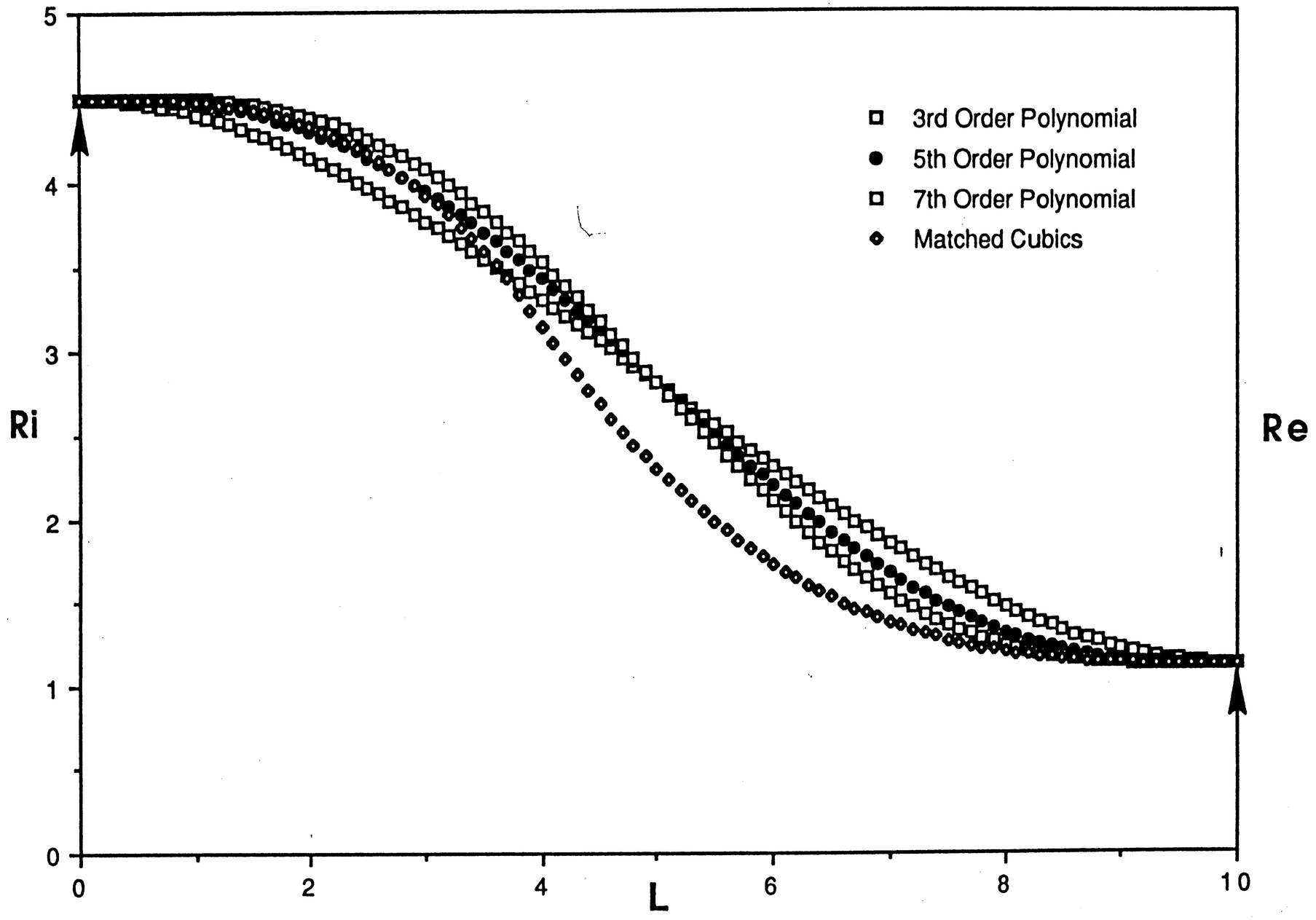

Figure 6.1: Contraction contours which are computed for same operation conditions but with different methods.

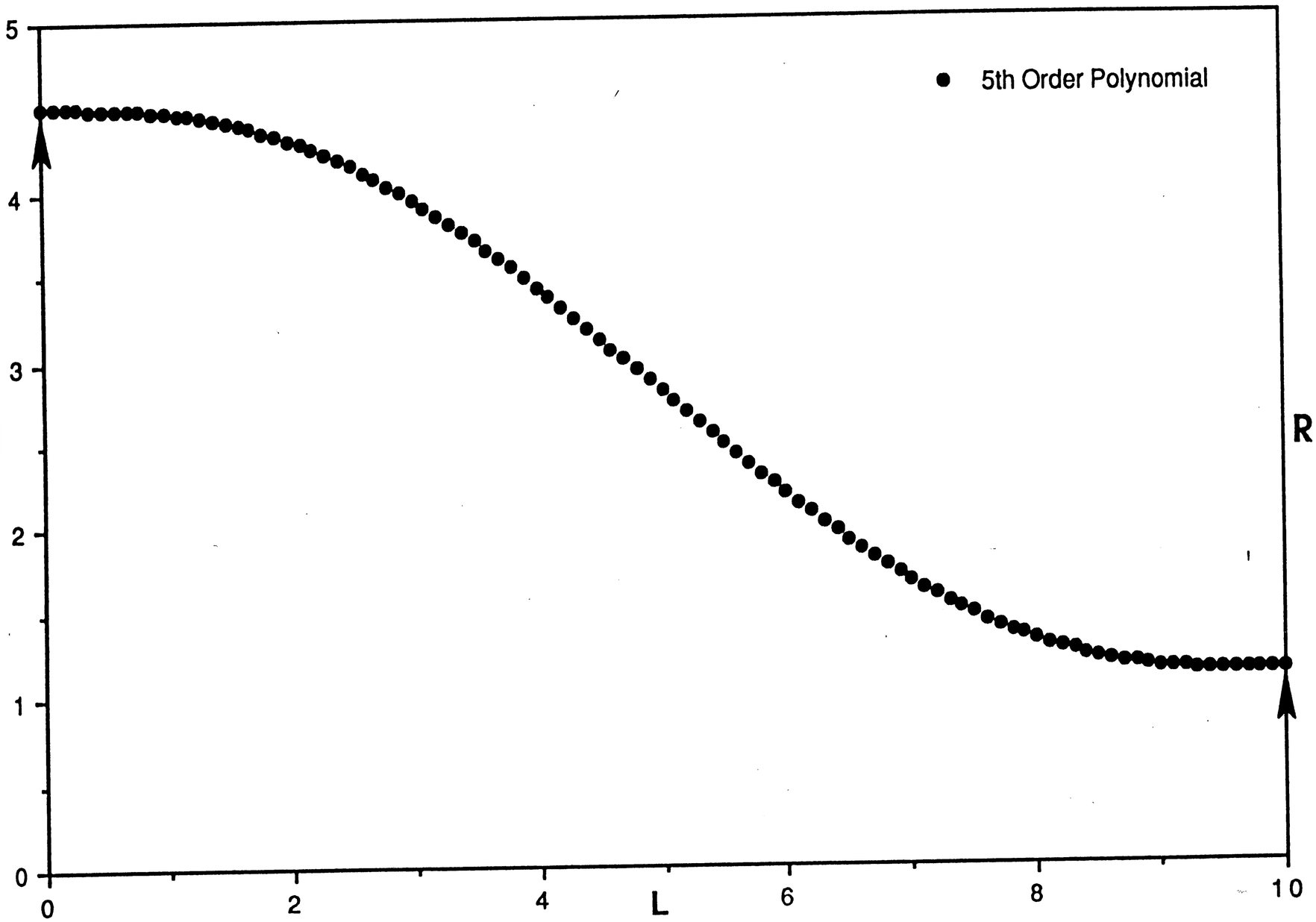

Figure 6.2: Contraction contour which is constructed with the Fifth Order Polynomial method and used in the experimental system.

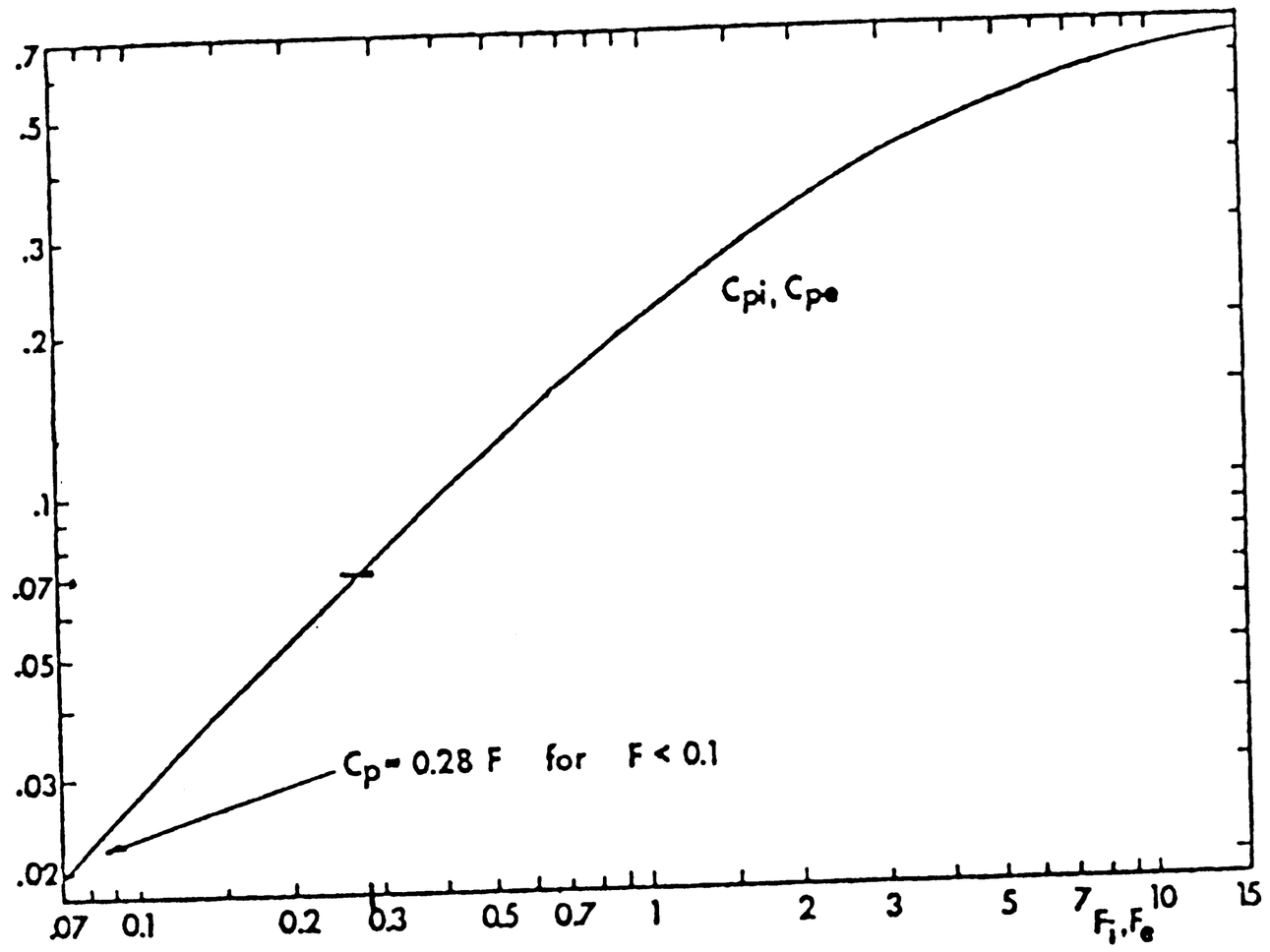

Figure 6.3: Dependence of c_{pe} on F_e.
[Reproduced from Morel, 1976]

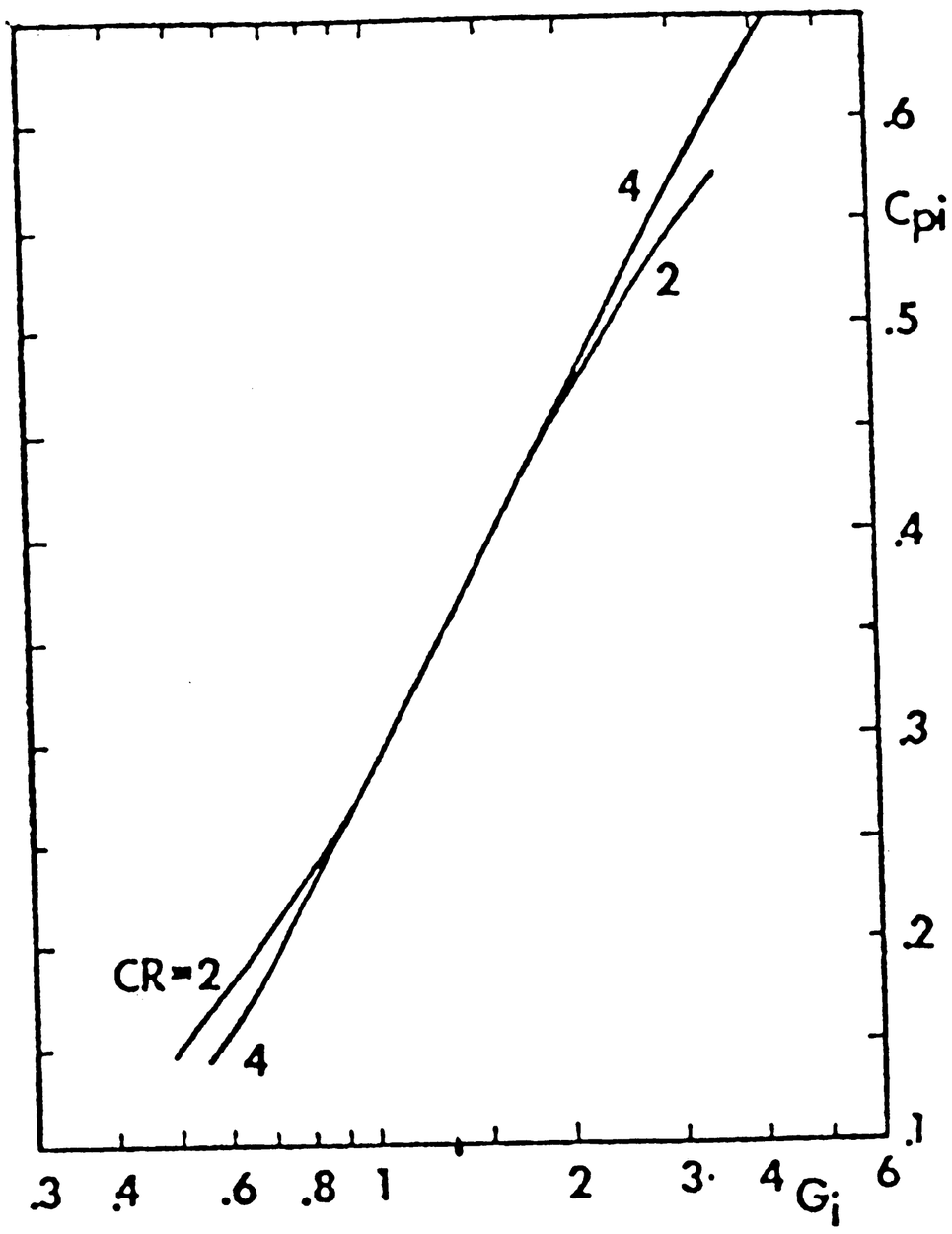

Figure 6.4 Dependence of c_{pi} on G_i.
[Reproduced from Morel, 1976]

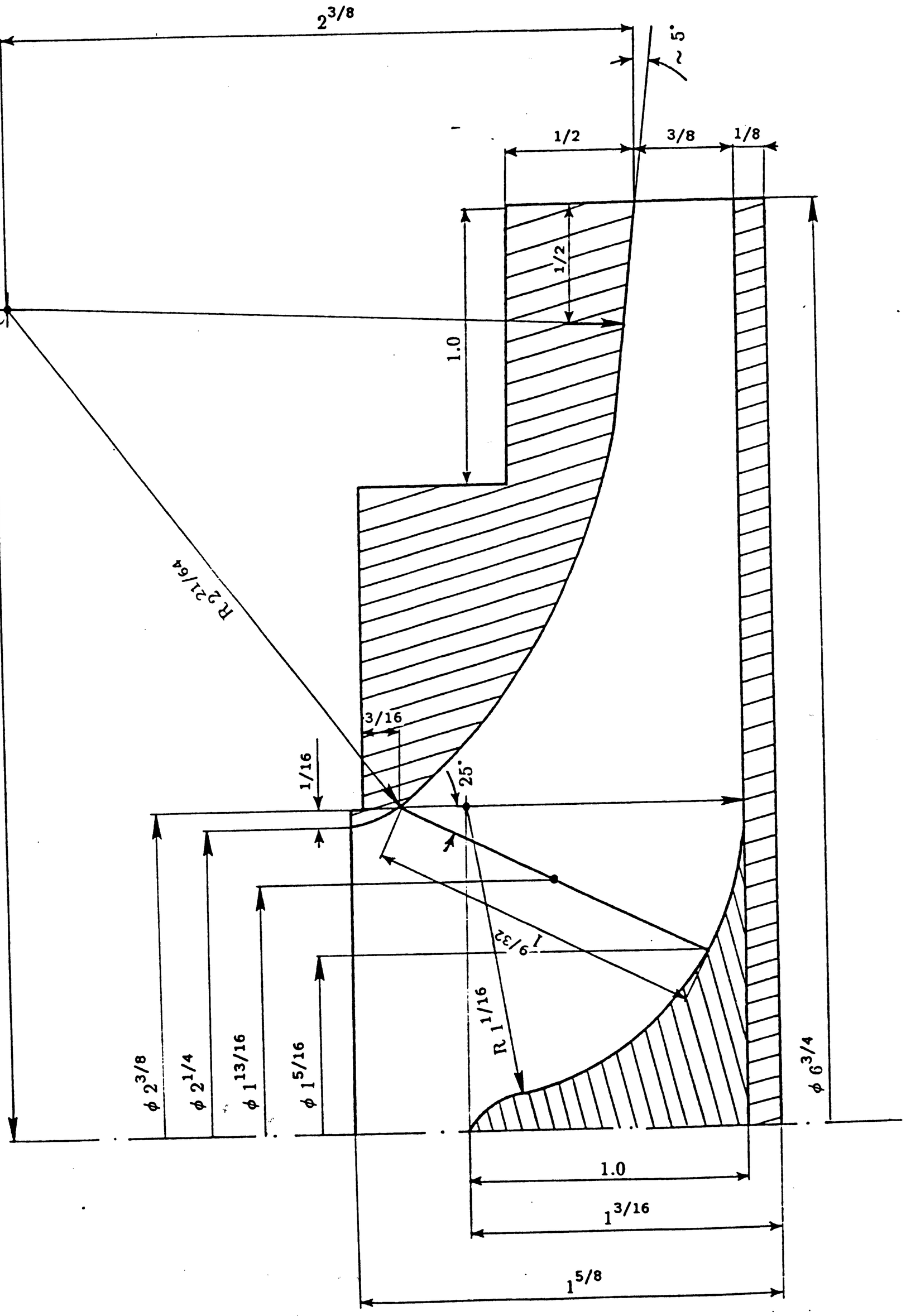

Figure 7.1: Detailed dimensions of the six blade impeller, side view.

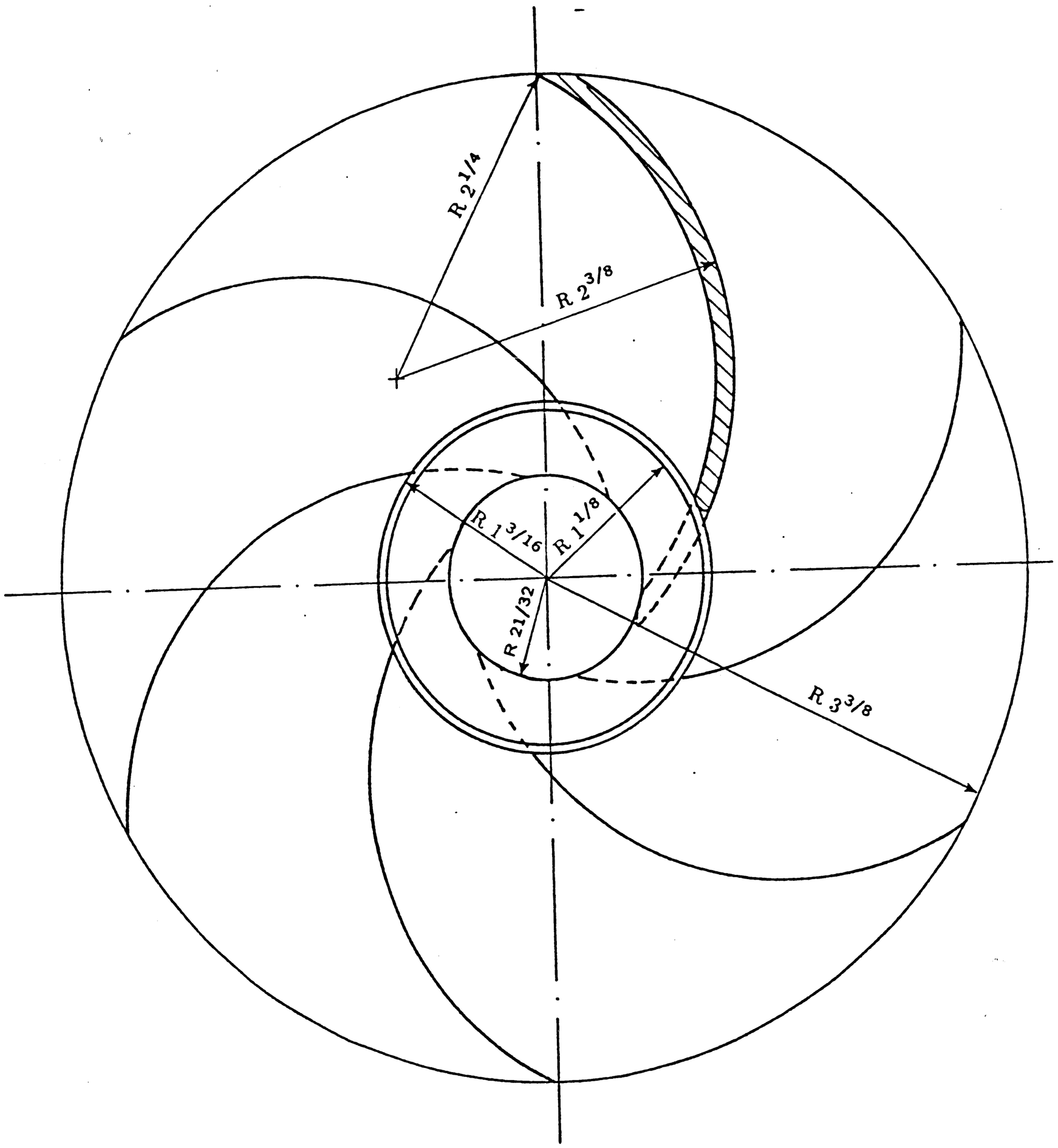

Figure 7.2: Detailed dimensions of the six blade impeller, plan view.

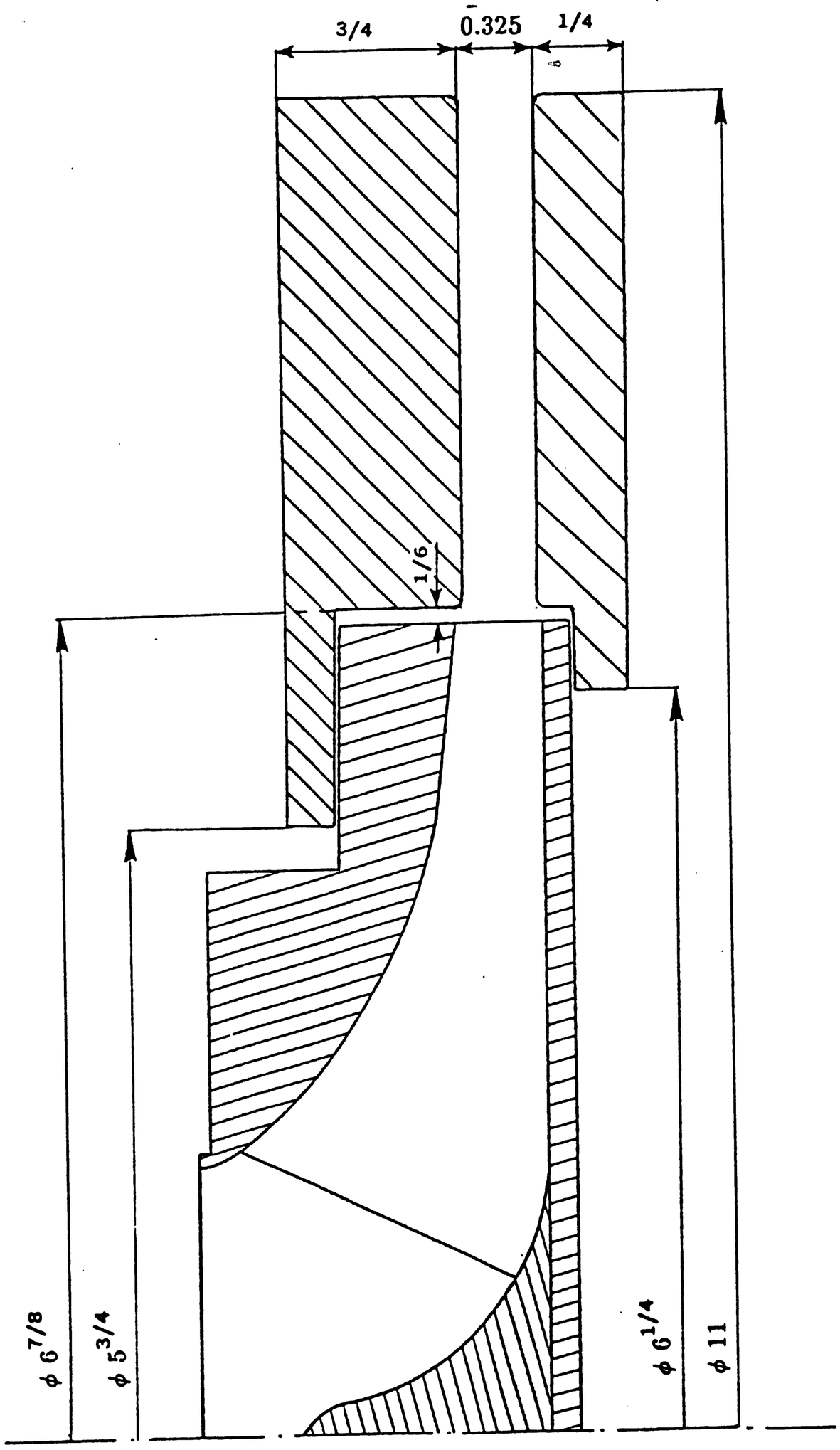

Figure 7.3: **Detailed dimensions of the diffuser discs, side view.**

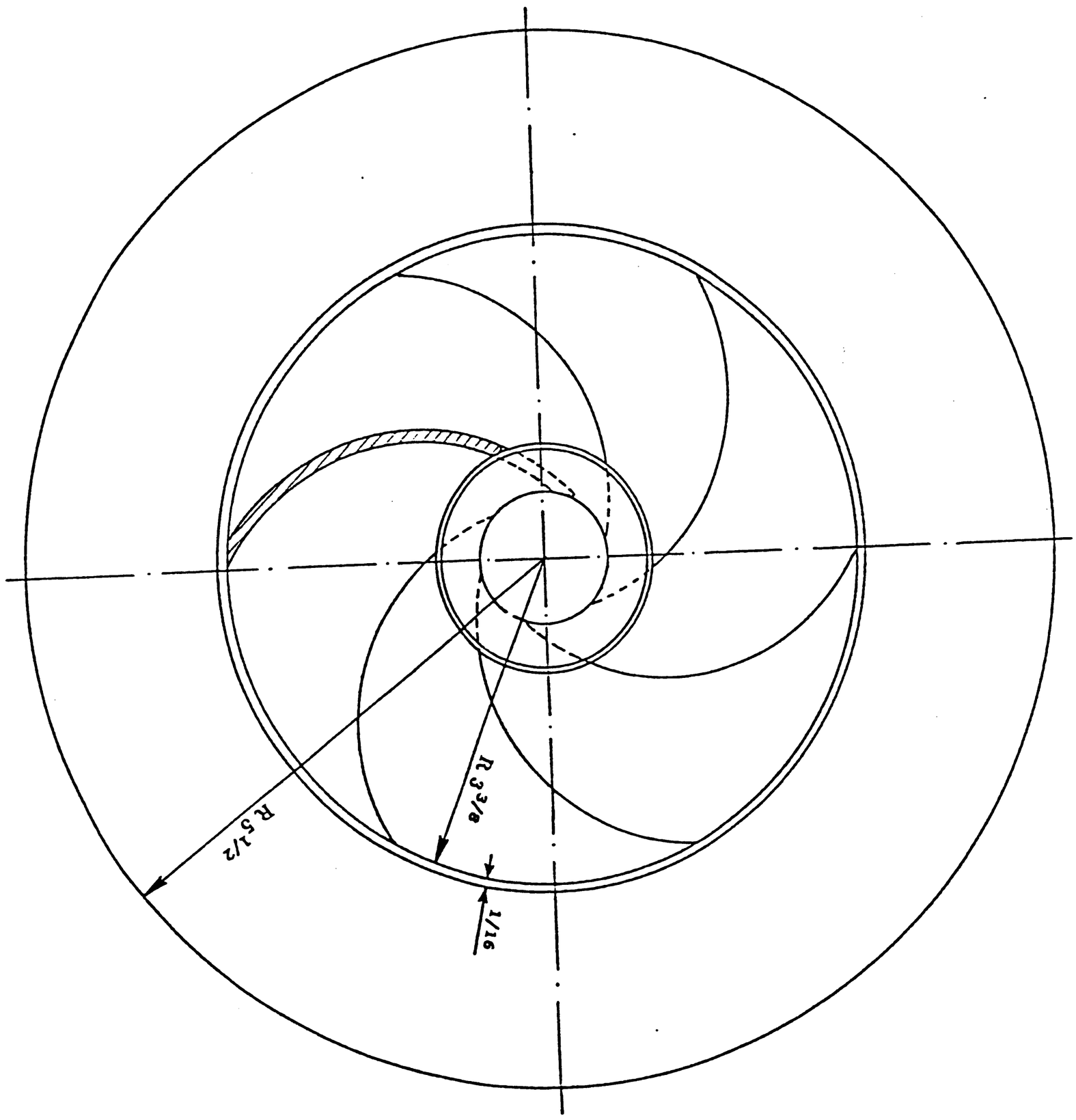

Figure 7.4: Detailed dimensions of the diffuser discs, plan view.

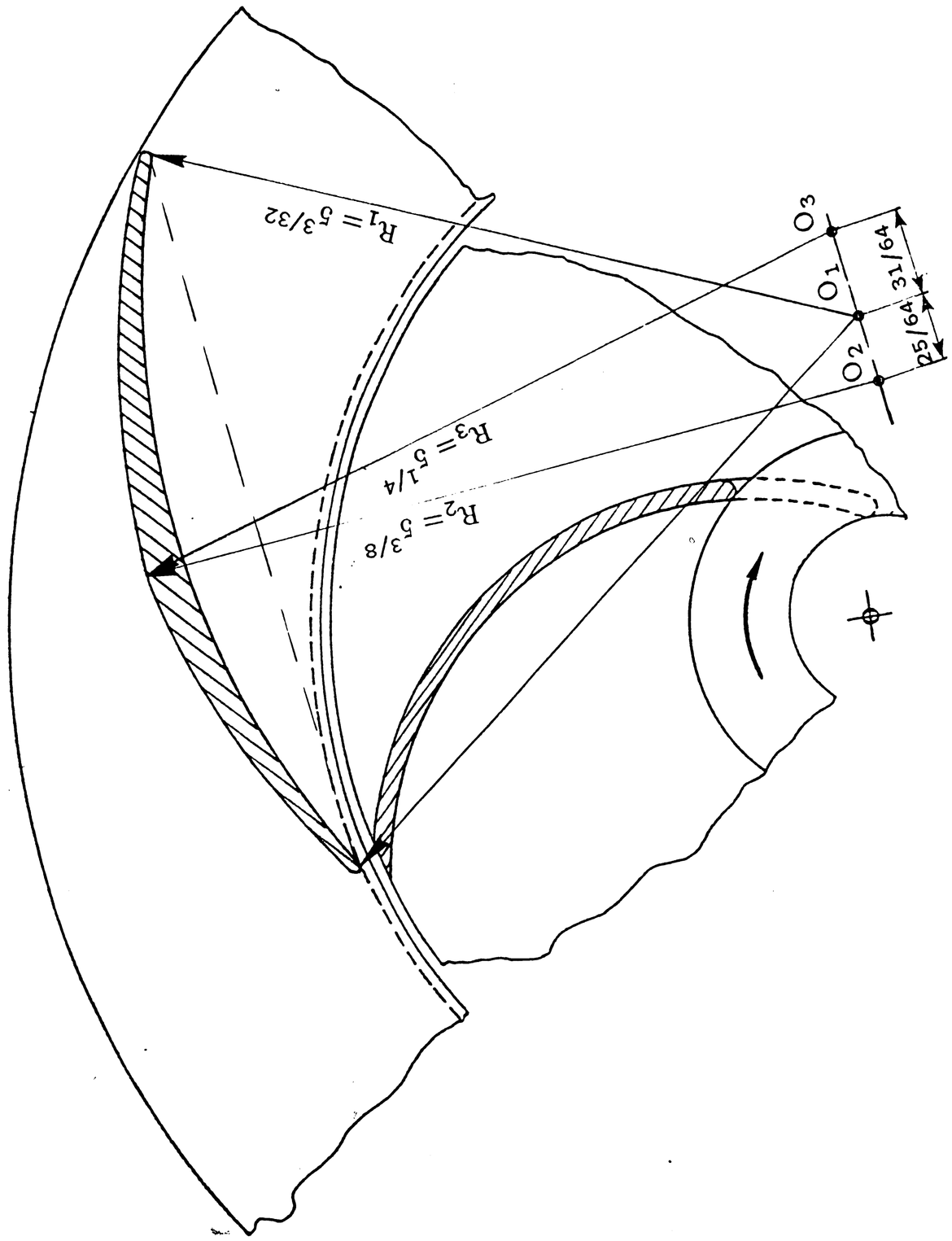

Figure 7.5: Dimensions of the diffuser blade on the diffuser discs.

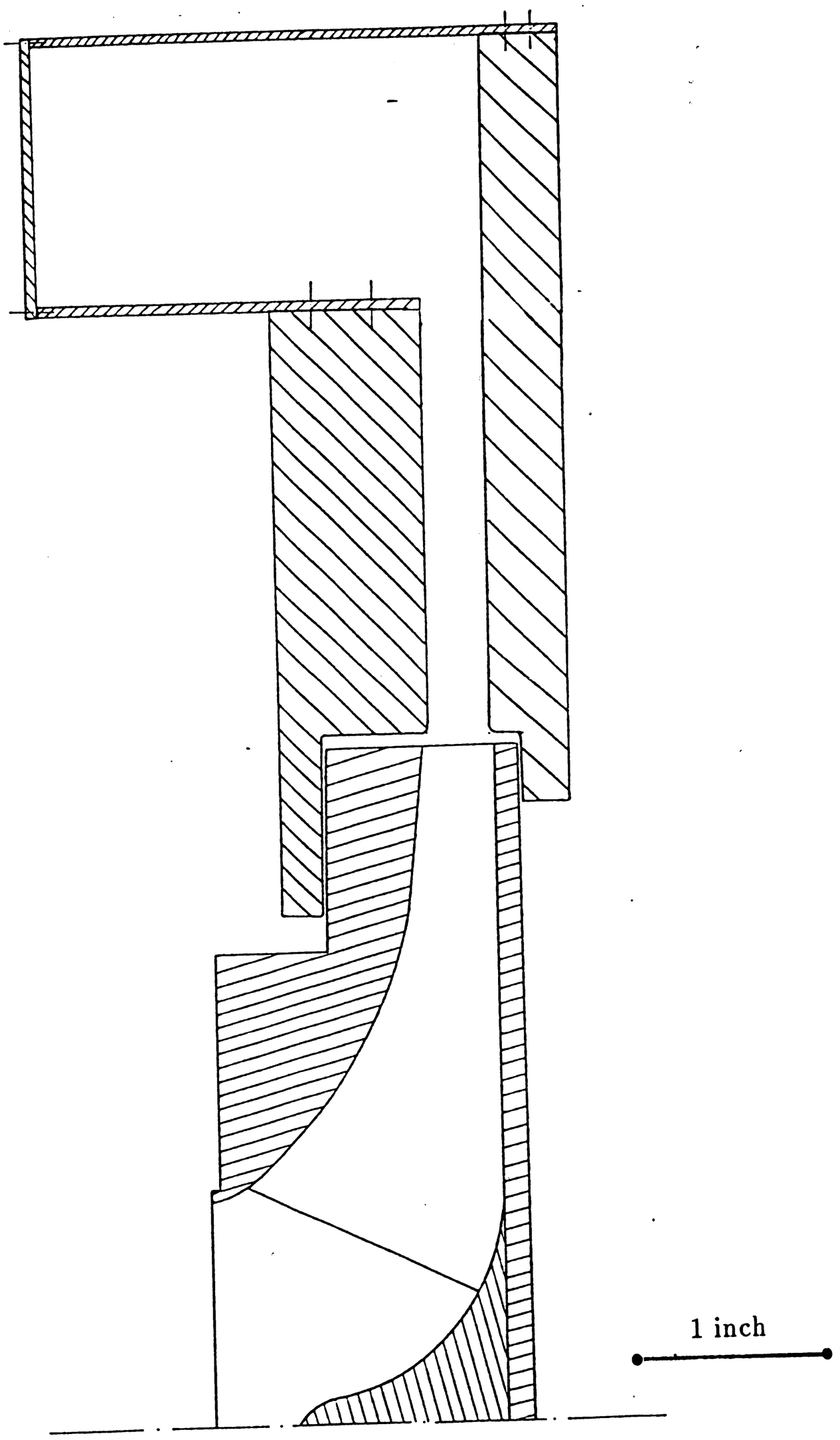

Figure 7.6: Collector with a rectangular cross section.

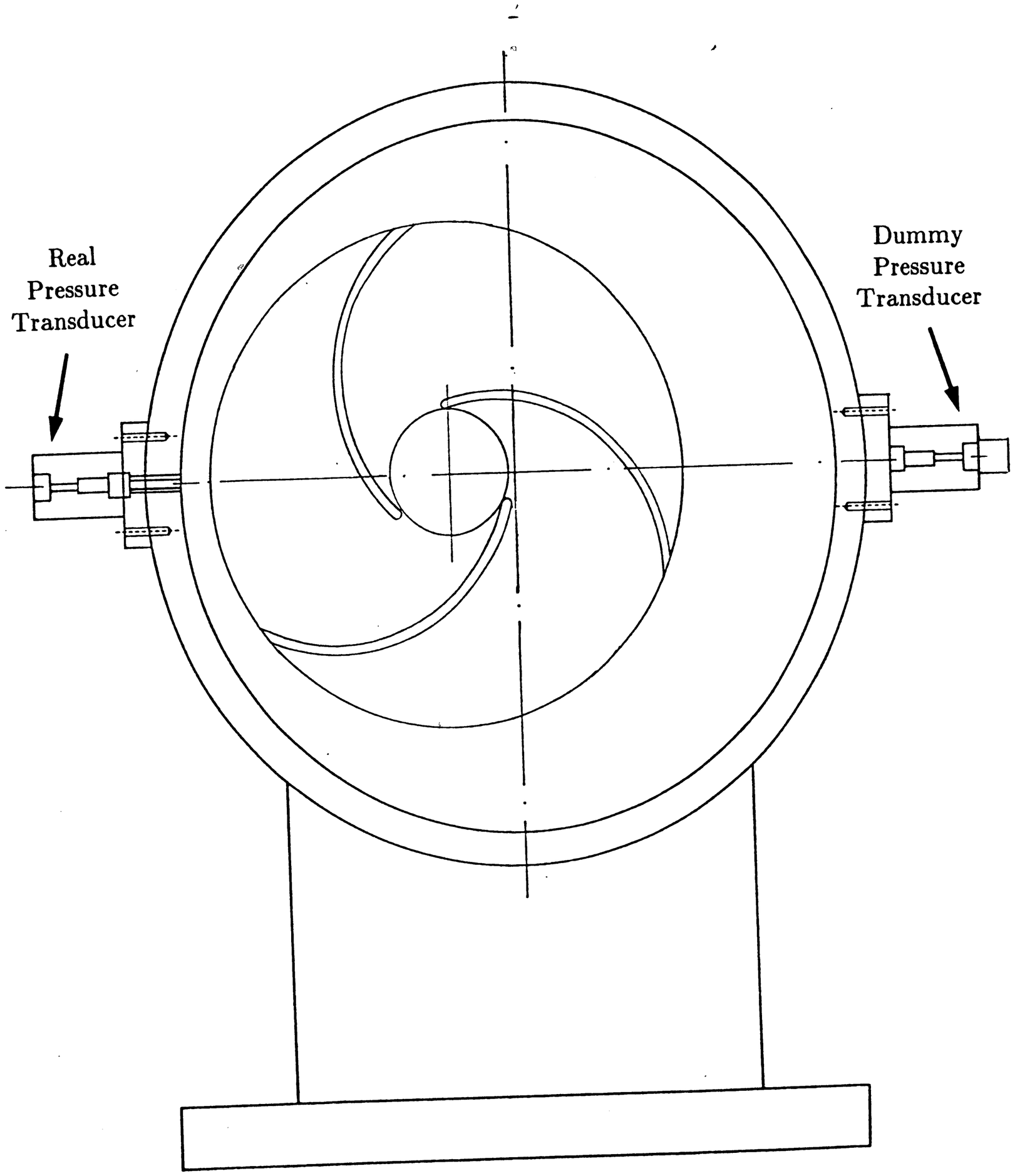

Figure 8.1: **Real and dummy pressure transducers which are placed on the volute simulation ring.**

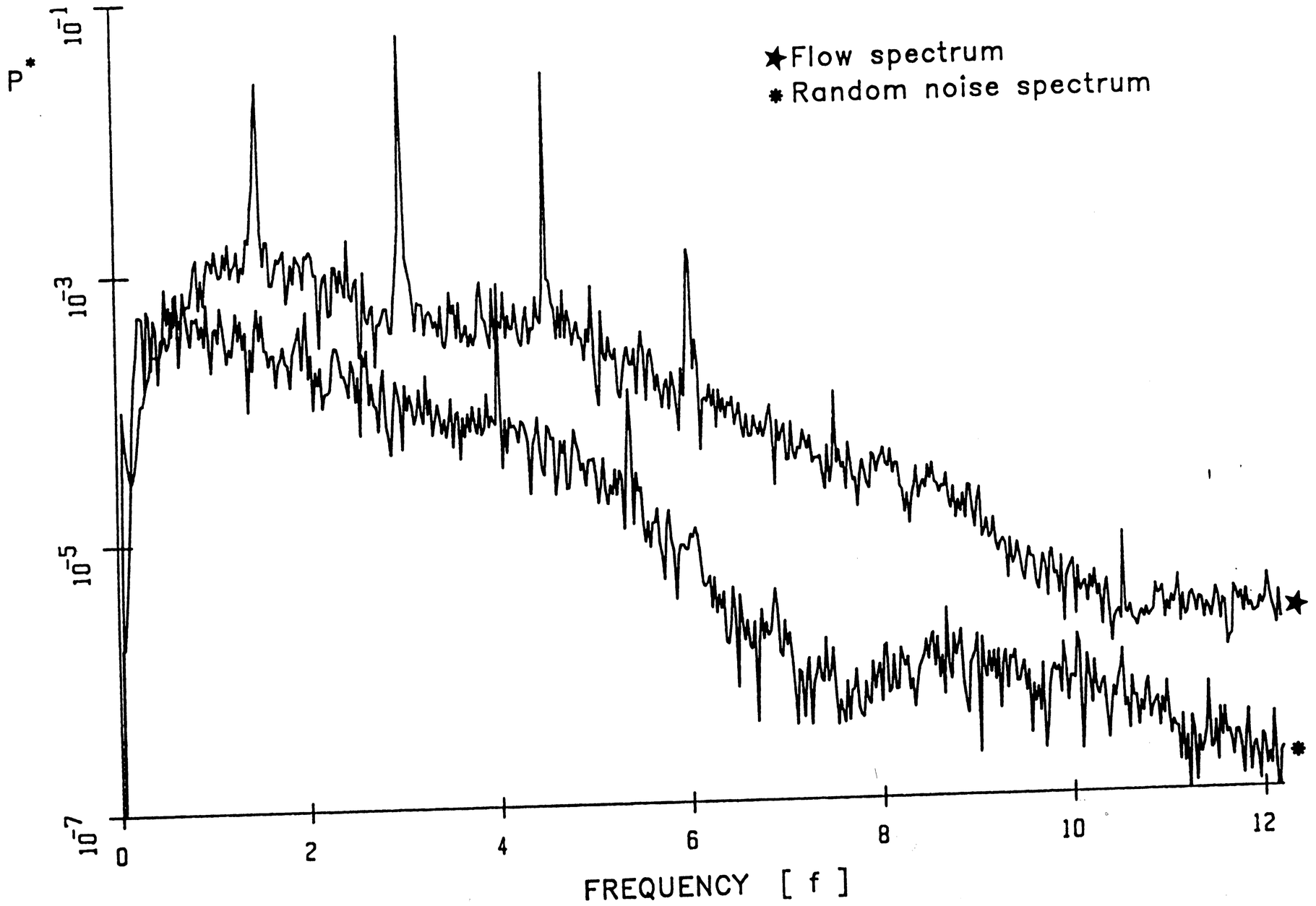
P*
10^{-1}
10^{-3}
10^{-5}
10^{-7}
★Flow spectrum
✱Random noise spectrum
0
2
4
6
8
10
12
FREQUENCY [f]

Figure 8.2

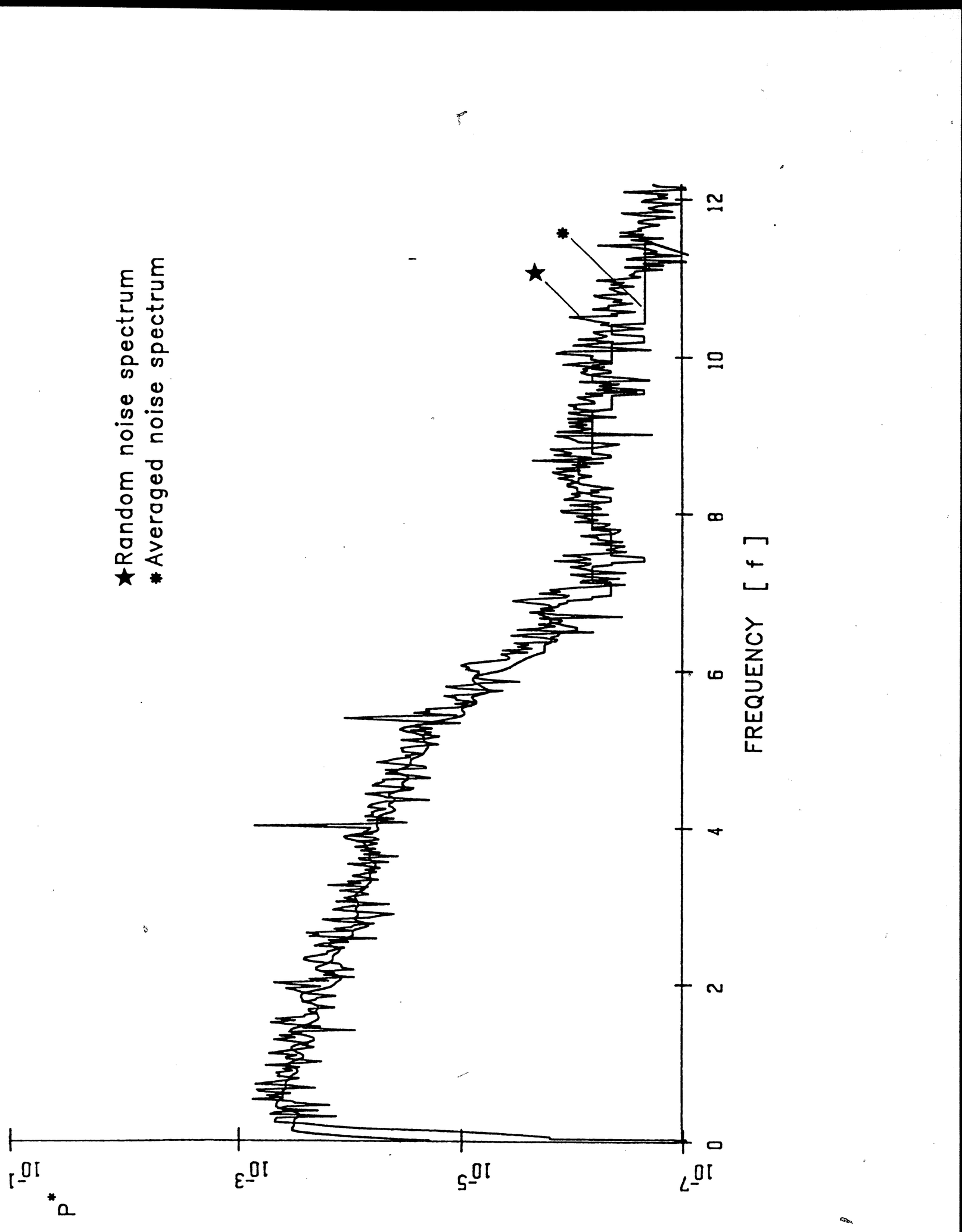
★Random noise spectrum
*Averaged noise spectrum
FREQUENCY [f]
0
2
4
6
8
10
12
10^{-7}
10^{-5}
10^{-3}
10^{-1}
d^*_p

Figure 8.3

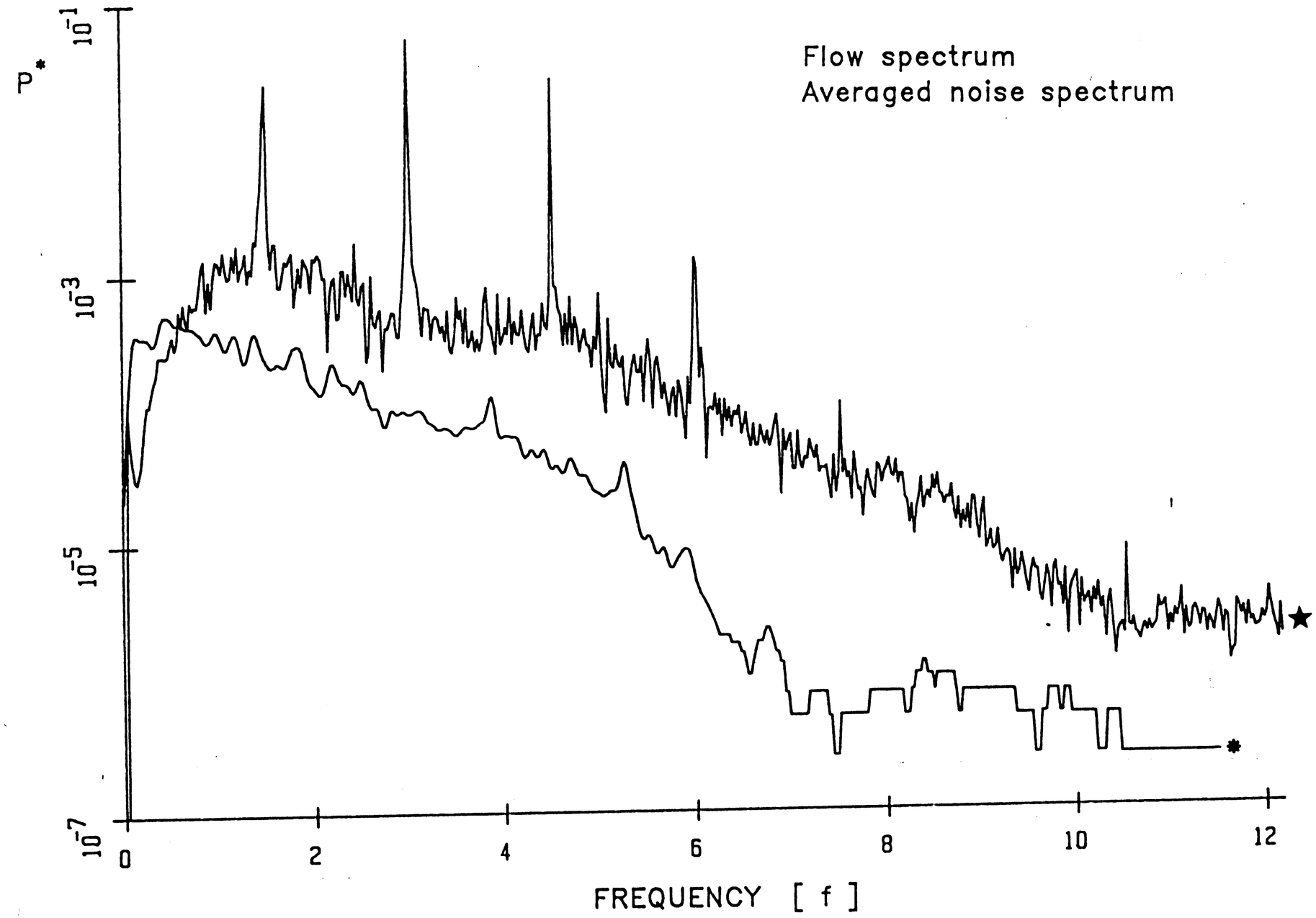
P*
10^{-1}
10^{-3}
10^{-5}
10^{-7}
0
2
4
6
8
10
12
FREQUENCY [f]
Flow spectrum
Averaged noise spectrum

Figure 8.4

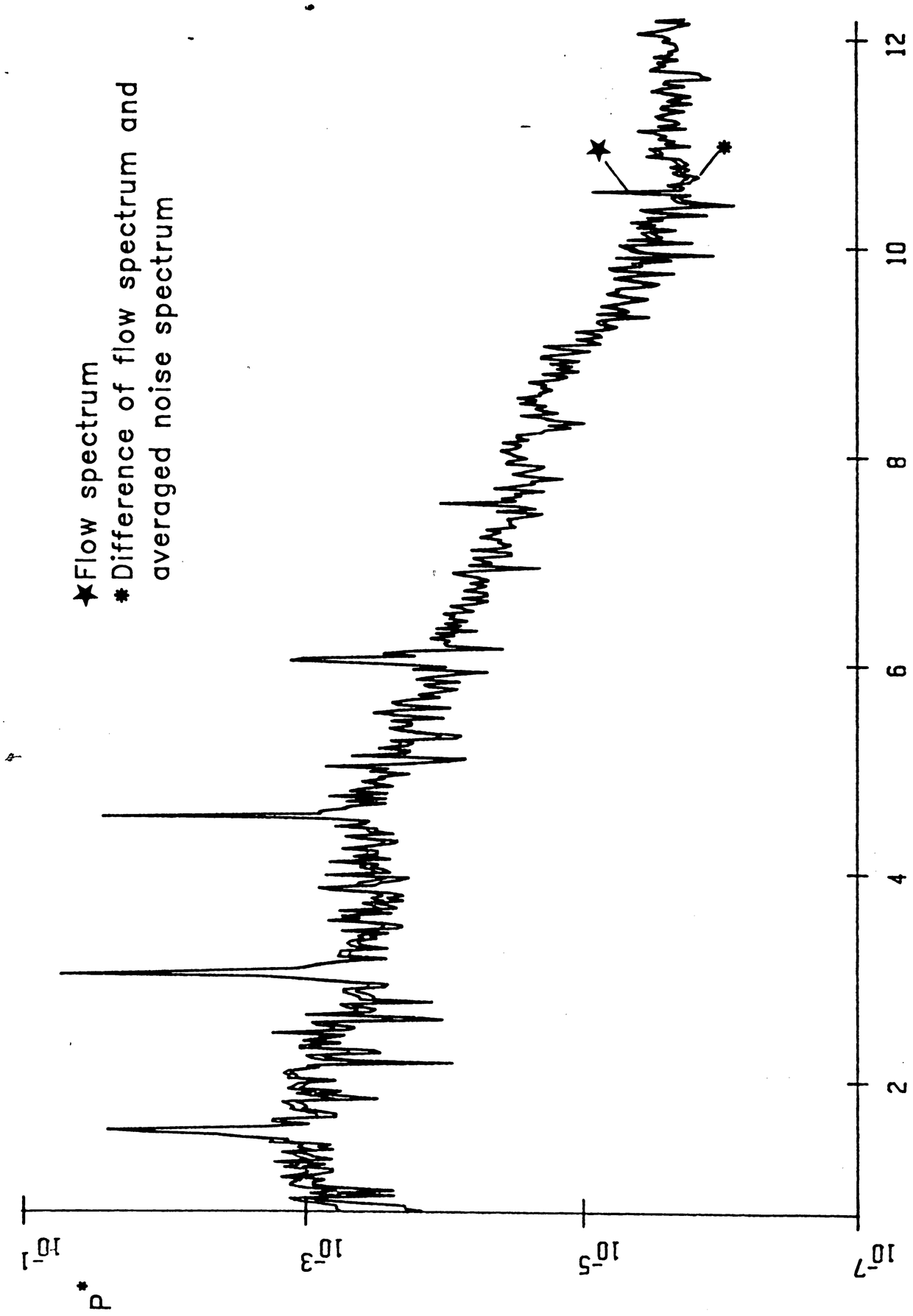
★Flow spectrum
*Difference of flow spectrum and averaged noise spectrum
FREQUENCY [f]
6
8
10
12
4
2
10^{-7}
10^{-5}
10^{-3}
10^{-1}
P_*

Figure 8.5

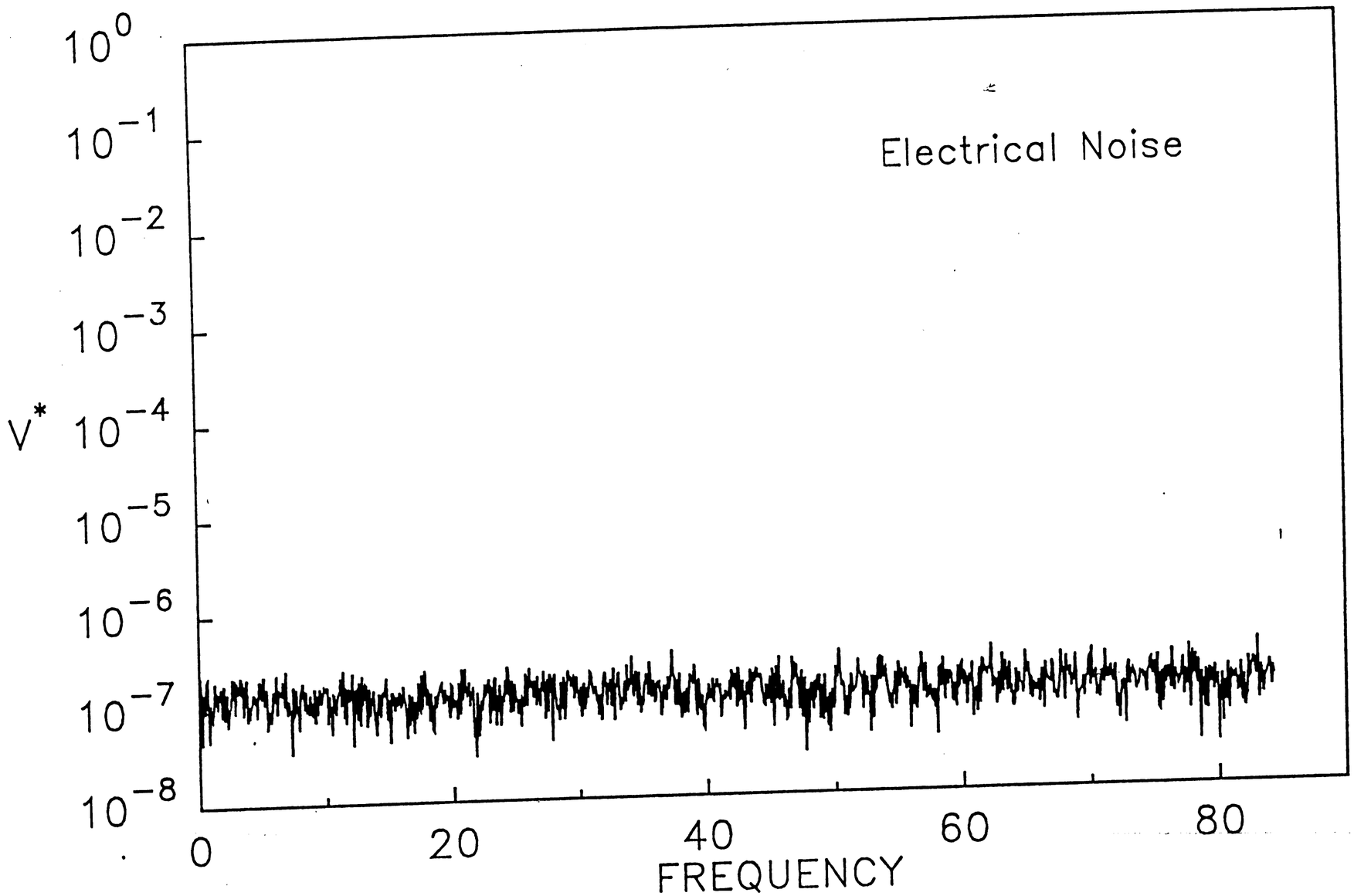
Electrical Noise
10^{0}
10^{-1}
10^{-2}
10^{-3}
10^{-4}
10^{-5}
10^{-6}
10^{-7}
10^{-8}
V*
0
20
40
60
80
FREQUENCY

Figure 8.6

VITA

The author was born in Safranbolu / Turkey on September 11, 1965 to Sevgi and Necati Akin.

He attended Darussafaka High School, Istanbul, and graduated in June 1984. He enrolled at Technical University of Istanbul, Turkey, where he was awarded his Bachelor of Engineering Degree in Mechanical Engineering in June 1988. He, then continued on his education at Lehigh University, Pennsylvania, with the aid of Turkish Oil Foundation Scholarship in Spring 1989, and of research and teaching assistantships for the rest of his education, obtaining a Master of Science Degree in Mechanical Engineering in June 1991.